Holmium-166 Radioembolization
SPECT IMAGING and DOSIMETRY

Martina Stella

Holmium-166 Radioembolization - SPECT Imaging and Dosimetry

PhD thesis, Utrecht University

Holmium-166 Radioembolization SPECT Imaging and Dosimetry

Radioembolizatie met Holmium-166 SPECT Beeldvorming en Dosimetrie

(met een samenvatting in het Nederlands)

Proefschrift

ter verkrijging van de graad van doctor aan de
Universiteit Utrecht
op gezag van de
rector magnificus, prof.dr. H.R.B.M. Kummeling,
ingevolge het besluit van het college voor promoties
in het openbaar te verdedigen op

donderdag 1 juni 2023 des ochtends te 10.15 uur

door

Martina Stella

geboren op 30 maart 1993
te Magenta, Italië

Promotoren:

Prof. dr. M.G.E.H. Lam

Prof. dr. H.W.A.M. de Jong

Copromotoren:

Dr. R. van Rooij

Dr. A.J.A.T. Braat

Beoordelingscommissie:

Prof. dr. I.H.M. Borel Rinkes (voorzitter)

Prof. dr. H.M. Verkooijen

Prof. dr. D.W.J. Klomp

Prof. dr. B.W. Raaymakers

Prof. dr. R. Boellaard

To Arthur and Rob,
who shared and guided this journey

Contents

CHAPTER 1

Introduction

Radioembolization

Radioembolization, also known as selective internal radiation therapy (SIRT), is a minimally invasive procedure that combines low-volume embolization and radiation to treat liver cancer. This procedure relies on the principle that hepatic tumors are mainly supplied by hepatic arteries [1], whereas healthy liver tissue is mainly fed by the portal vein. Thus, radioactive microspheres will predominantly lodge in and around tumorous tissue, sparing healthy liver tissue.

Until a few years ago, yttrium-90 (^{90}Y) was the only radionuclide used for this procedure, with two types of microspheres commercially available, either resin or glass.

The possibilities to use holmium-166 (^{166}Ho) as a potential isotope for the internal radiation therapy of hepatic tumors was first proposed in 1991 by Mumper *et al.* [2], while in 2001 Nijsen *et al.* [3] performed liver tumor targeting in rats by selective delivery of ^{166}Ho microspheres. Following these promising results in animal studies, in 2010 Smits *et al.* [4] designed the first phase I human trial to evaluate the safety and toxicity profile of ^{166}Ho-microspheres radioembolization. Since the first publication on ^{166}Ho-microspheres liver radioembolization, there has been a growing interest in ^{166}Ho-microspheres, resulting in more than seventy publications up until 2022.

Holmium-166 Isotope

^{166}Ho-microspheres were developed at the Department of Radiology and Nuclear Medicine of the University Medical Center Utrecht and their preparation was granted a patent in 2008 [5]. In 2015, ^{166}Ho-microspheres received CE mark as medical device under the commercial name of QuiremSpheres™ (Quirem Medical B.V., The Netherlands). In terms of clinical application in liver tumors, ^{166}Ho-microspheres are an alternative to the existing ^{90}Y-based medical devices. ^{166}Ho-microsphere characteristics, compared to ^{90}Y-microspheres, are summarized in **Table 1.1**.

The radioactive isotope ^{166}Ho is a high-energy beta-emitting isotope for therapeutic use, but it also emits primary gamma photons that can be imaged with single photon emission computed tomography (SPECT). Upon decay to the stable isotope erbium-166 (^{166}Er), with a half-life of 26.8 h, ^{166}Ho emits several gamma photons, most of which are 81 keV (abundance 6.7%), 1379 keV (0.9%) or 1581 keV (0.2%). Furthermore, being a lanthanide, ^{166}Ho can be imaged by magnetic resonance imaging (MRI) thanks to its paramagnetic properties [6][7].

This dissertation will solely investigate ^{166}Ho imaging by means of SPECT.

^{166}Ho microspheres are made of poly-L-lactic acid (PLLA), containing the isotope ^{166}Ho (see **Figure 1.1**). First, in the microspheres production process, holmium-165 (^{165}Ho) is

embedded within the matrix structure of PLLA. Then, a part of ^{165}Ho is activated to ^{166}Ho by neutron activation in a nuclear reactor.

Commercial Name	SIR-Spheres®	TheraSpheres®	QuiremSpheres™
Matrix	Resin	Glass	Poly-l-lactic acid
Diameter (mean, range)	32μm (20–60μm)	25μm (20–30μm)	30μm (25–35μm)
Density	1.6 g/mL	3.3 g/mL	1.4 g/mL
Isotope	^{90}Y	^{90}Y	^{166}Ho
β-energy mean/max	0.9/2.28 MeV	0.9/2.28 MeV	0.7/1.81 MeV
β penetration mean/max	2.5/11 mm	2.5/11 mm	2.5/8 mm
γ-peak suitable for imaging	–	–	81 keV (6.7%)
Half-life	64.1 h	64.1 h	26.8 h
Number of microspheres for 3 GBq	40–80 million	1.2–5 million	7.5–15* million
Activity per microsphere	50 Bq	1250–2500 Bq	200–400 Bq
Imaging technique	Bremsstrahlung SPECT PET	Bremsstrahlung SPECT PET	SPECT MRI
Surrogate/scout	^{99m}Tc-MAA	^{99m}Tc-MAA	QuiremScout™ ^{99m}Tc-MAA

Table 1.1

Microsphere characteristics. Comparison between SIR-Spheres®, TheraSpheres®, and QuiremSpheres™. *For a typical treatment, the number of microspheres will be in the range of 15–25 million.

Figure 1.1

Scanning electron microscope image of holmium microspheres. Content licensed under a Creative Common Attribution 2.0 Generic License. Publisher: Springer Nature. Content attributed to M. L. Smits *et al.*, "Holmium-166 radioembolization for the treatment of patients with liver metastases: design of the phase I HEPAR trial," J. Exp. Clin. Cancer Res., vol. 29, no. 1, p. 70, Jun. 2010.

Clinical Workflow

The clinical workflow for [166]Ho radioembolization follows similar steps as for radioembolization with other devices. These are summarized in **Figure 1.2** and discussed in the following.

Patient Eligibility Assessment

Indications and contraindications for radioembolization with [166]Ho-microspheres are in line with radioembolization with ^{90}Y-microspheres [8] and are summarized in **Table 1.2**.

Work–up

During a preparatory angiography, the hepatic vasculature is mapped and injection positions are determined by the interventional radiologist. A small batch of [166]Ho-microspheres with limited activity (200–250 MBq; 60 mg; approximately 3 million [166]Ho-microspheres) can be used as a scout dose. Contrary to previous ^{90}Y-microspheres products, [166]Ho-microspheres radioembolization offers the possibility to use the same type of commercially available particles for both scout and treatment procedure, reducing the variables among these and theoretically reducing the discrepancy between the work-up procedure and the treatment procedure.

Post–Scout SPECT

The amount of activity injected as scout is sufficient for SPECT/CT quantification, but limited enough not to cause tissue damage in case of shunting to the gastrointestinal organs or the lungs [9]. SPECT images are assessed for the presence of extrahepatic depositions in gastrointestinal organs and for lung shunting.

Treatment Planning

The current activity calculation for [166]Ho-microspheres is based on the first study in humans, a dose escalation study, which identified the maximum tolerated dose for [166]Ho-microspheres radioembolization at 60 Gy [10]. The absorbed dose delivered by 1 GBq in 1 kg tissue is 15.87 Gy for [166]Ho, under the assumption of homogenous distribution in the target volume and that all particles remain lodge in that volume (i.e., there is no biological excretion). Thus, the formula for the prescribed activity based on a 60 Gy average absorbed dose to the whole liver is the following:

$$\textit{Prescribed activity } [MBq] = \textit{Liver weight } [kg] \times 3781 \left[\frac{MBq}{kg} \right]$$

1
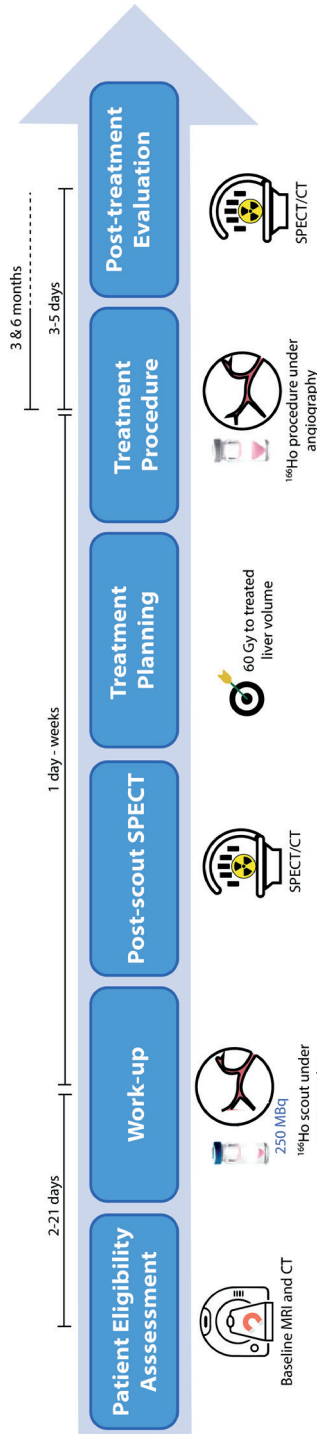
Figure 1.2

The steps included in the clinical workflow for [166]Ho-microspheres liver radioembolization. After having been assessed for eligibility based on criteria summarized in **Table 1.2**, a patient undergoing [166]Ho radioembolization would encounter three main phases: the pre-treatment (work-up procedure, post-scout SPECT and treatment planning), the treatment itself, and the post-treatment/follow-up.

Indications	Contraindications

1. Unresectable primary or metastatic hepatic disease with liver-only or liver dominant tumor burden	1. Pre-treatment scan demonstrating:
	  a. The potential of >30 Gy radiation exposure to the lung*
	  b. Flow to the gastrointestinal tract that cannot be corrected by catheter techniques

2. Life expectancy >3 months	2. Limited hepatic reserve
	  a. Irreversibly elevated bilirubin levels (> 2.0 mg/dl)
	  b. Reduced albumin (< 3 g/dl)

3. An eastern cooperative oncology group (ECOG) status ≤ 2	
4. In case of (suspected) cirrhosis: Child-Pugh score ≤ B7	3. Prior external beam radiation therapy involving the liver in the treatment field of view. Systemic radionuclide treatments are allowed (e.g. ^{177}Lu-dotatate)

5. Pre-operative radioembolization for:
  a. Downstaging
  b. Bridge to transplant
  c. Hypertrophy induction
	4. Severe contrast allergy, not manageable or responsive to prophylaxis

Table 1.2

Recommendations and contraindications for radioembolization. *Based on manufacturer's instruction for use.

According to current instructions for use [11], the average absorbed dose to the perfused volume may exceed 60 Gy (allowing for personalized dosimetry), as long as the average absorbed dose to the whole liver does not exceed 60 Gy.

Treatment Procedure

After a successful work-up procedure, patients undergo treatment with the administration of the treatment dose in a subsequent treatment procedure. Same-day treatment with [166]Ho-microspheres radioembolization is feasible [12], even though it limits possibilities of personalized treatment based on [166]Ho-microspheres scout distribution due to calculation and ordering of the prescribed activity.

Post-treatment Evaluation

To validate the technical success of the radioembolization procedure, a SPECT/CT can be performed. It allows for the quantification of the dose in the compartments of interest, i.e., tumor and healthy liver, and the evaluation of the dose–response effect.

> **Dosimetry**
>
> For radioembolization to be efficacious, a high tumoral radiation dose is required, while avoiding irradiation of the lungs, other extra-hepatic tissues, and hepatic-non-tumoral-tissue. The determination of the radiation absorbed dose in a target tissue from a given administered activity is called dosimetry. Dosimetry is crucial both in the planning phase, to determine the therapeutic activity to be injected, and in the post-treatment phase, to evaluate the treatment procedure. For ^{166}Ho-microspheres radioembolization, the dose estimate can be assessed using SPECT imaging.

Clinical Studies on ^{166}Ho Radioembolization

From 2009, eight clinical studies using ^{166}Ho-microspheres for radioembolization have been carried out. Type of study, patient population, study phase and design, and primary objective are summarized in **Figure 1.3.**

At least six other studies, mainly exploring the additional value of individualized treatment are currently in preparation. The findings regarding the primary end-point of the prospective studies completed within 2022 are summarized in **Table 1.3**. To be noted, the phase II study (HEPAR PLuS) which investigated the addition of ^{166}Ho-microspheres radioembolization after peptide receptor radionuclide therapy in patients with metastatic liver neuroendocrine neoplasms [13] constitutes the majority of the dataset used in this dissertation for patient data analysis.

Imaging to improve ^{166}Ho radioembolization

In the near future, personalized medicine could optimize patient treatments. In the frame of ^{166}Ho-microspheres radioembolization (so-called 'Holmium Platform'), this means that dose thresholds for patient selection and treatment planning need to be established. The possibility to define robust dose–response values relies on: i) accurate activity quantification in SPECT images, ii) the delineation of the volume of interest for which to assess the absorbed dose.

These two tasks remain challenging in the current clinical practice and their improvement is the focus of this dissertation. To address these challenges, two distinct research lines have been pursued, investigating: i) the possibility to use clinical ^{166}Ho SPECT images derived from a dual isotope protocol for ^{166}Ho dosimetry and ii) the best method to automatically segment the healthy liver volume.

Name	Population	Type	Subjects		Primary objective
HEPAR I	Liver metastases	Phase II, Single center	15	Dose-escalation toxicity	Toxicity of Ho-166 poly lactic microspheres using common toxities criteria vs 3 criteria with 12 weeks
HEPAR II	Liver metastases	Phase II, Single center	37	Toxicity	Target lesions tumour response 3 month after treatment using RECIST 1.1 criteria using CT scan
HEPAR PLuS	NET liver metastases	Phase II, Single center	31	Efficacy	Efficacy of adjuvant ^{166}Ho radioembolization after systemic ^{177}Lu-dotatate within 3 months using RECIST 1.1
SIM	mCRC	Phase II, Randomized, Single center	25	Feasibility	Investigate whether using the Surefire Infusion System during ^{166}Ho-radioembolization increases the posttreatment tumor to non-tumor activity concentration ratio.
HEPAR Primary	HCC	Phase II, Multi center	30	Toxicity	Safety, expressed as the rate of unacceptable toxicity, which is the occurrence of RE-induced liver disease.
HORA EST	Early stage HCC	Phase I, Single center	20	Dose-escalation toxicity	Dose-finding study assessing treatment area dose that will result in delivery of a radiation absorbed dose of ≥ 120 Gy to the target area
Emeritus	Liver metastases Liver cancer	NA, Single center	6	Feasibility	Feasibility of MR imaged administration of holmium microspheres, defined as successful treatment under MRI in at least 4 of 6 patients

Phase I　　Phase II　　Single center　　Multi center　　R Randomized

Figure 1.3
Summary of the clinical studies on ^{166}Ho radioembolization completed between 2009 and 2022. HCC = hepatocellular carcinoma, mCRC = metastatic colorectal cancer, NET = neuroendocrine tumor, RE = radioembolization, RECIST = Response Evaluation Criteria in Solid Tumors.

Reference	Study	Main finding
Roosen, J, *et al.*[16]	EMERITUS	[166]Ho transarterial radioembolization is feasible and safe within an MRI scanner: • Administration of [166]Ho-microspheres within the MRI scanner was feasible in 82% injection positions • Intraprocedural holmium-sensitive MRI allowed for tumor dosimetry in 95% of treated tumors • 33% CTCAE grade 3–4 toxicities were observed, and no adverse events were attributed to treatment in the MRI

Reinders-Hut MTM, *et al.* [17]	HEPAR Primary	[166]Ho-microspheres radioembolization is a safe treatment option for HCC patients with:
		• Unacceptable toxicity related to study treatment occurred in 10% of patients
		• Complete or partial response for:
		  - 54% of the target liver lesions at 3 month follow-up
		  - 84% of the target liver lesions at 6 month follow-up
		• Median overall survival was 14.9 months

Van Roekel C, *et al.* [18]	SIM	Between anti-reflux and standard microcatheter: • No difference in tumor targeting • No difference in infusion efficiency • No influence on the dose-response rate • Confirmed safety and efficacy in mCRC

Braat AJAT, *et al.* [13]	HEPAR PLuS	[166]Ho-microspheres radioembolization, as an adjunct to peptide receptor radionuclide therapy is safe and effective, with:
		• Response (complete or partial) in the liver, according to RECIST 1.1:
		  - 43% at 3 months
		  - 47% at 6 months
		• Acceptable toxicity
		• No loss in quality of life

Prince JF, *et al.* [19]	HEPAR II	[166]Ho-microspheres radioembolization induced a tumor response and acceptable toxicity profile in salvage patients with: • Complete response, partial response, or stable disease of the target lesion obtained in 73% of population at 3 months follow-up • Median overall survival of 14.5 months

Smits MLJ, *et al.* [10]	HEPAR I	• The maximum tolerated radiation absorbed dose was identified as 60 Gy (averaged over the perfused volume)
		• Stable disease or partial response regarding target lesions achieved:
		  - In 93% population at 6 weeks follow-up
		  - In 64% population at 12 weeks follow-up

Table 1.3

Summary of the published clinical findings, up until 2022, deriving from the prospective studies completed. CTCAE = Common Terminology Criteria for Adverse Events, HCC = HepatoCellular Carcinoma, mCRC = metastatic ColoRectal Cancer, RECIST = Response Evaluation Criteria in Solid Tumors.

> **Dual isotope protocol**
>
> The possibility to simultaneously use two isotopes to identify healthy liver and tumorous tissue was firstly suggested by Lam *et al.* [14]. A protocol including ^{166}Ho (lodging primarily in the tumorous tissues), for either the scout or the treatment procedure, and technetium-99m (^{99m}Tc) stannous phytate (accumulating in the healthy liver) for healthy liver delineation was proposed to allow for automatic healthy liver segmentation. Following ^{166}Ho-microspheres and ^{99m}Tc-stannous phytate injection, a conventional SPECT/CT that simultaneously acquires the two isotopes (^{166}Ho and ^{99m}Tc) can be performed. ^{166}Ho and ^{99m}Tc images are then reconstructed. These reconstructions are intrinsically registered and can be used to automatically define the healthy liver, avoiding segmentation and registration of a separately acquired CT, a time-consuming and prone-to-error task. The feasibility of this protocol was proved by van Rooij *et al.* [15] using a phantom study and a proof-of-concept clinical case.

Thesis outline

This dissertation aims to investigate clinical SPECT imaging for ^{166}Ho-microspheres radioembolization dosimetry and the use of a ^{166}Ho-^{99m}Tc dual isotope protocol for automatic healthy liver segmentation.

Part I addresses the technical challenges of quantitative ^{166}Ho SPECT imaging in clinical practice, and mainly includes findings deriving from phantom experiments. It opens with **Chapter 2**, which assesses the impact of high ^{166}Ho count rate on post-treatment ^{166}Ho dosimetry. This may be an issue when imaging patients directly after receiving a therapeutic amount of ^{166}Ho-microsphres. It continues with **Chapter 3**, focusing on scatter compensation and automatic healthy liver segmentation using a ^{166}Ho-^{99m}Tc dual isotope protocol. It concludes with **Chapter 4**, evaluating the acquisition and reconstruction parameters to harmonize ^{166}Ho SPECT imaging; this would enable the comparison of ^{166}Ho dosimetry outcomes between centers, which may be vital to determine dose-response relationships.

Part II is instead mainly focused on the transition of the ^{166}Ho-^{99m}Tc dual isotope protocol to the clinical setting; to this purpose patient data has been analyzed. **Chapter 5** assesses the feasibility of the ^{166}Ho-^{99m}Tc dual isotope protocol by comparing the resulting dosimetry in ^{166}Ho SPECT images acquired in presence or absence of additional ^{99m}Tc. **Chapter 6** applies the automatic healthy liver segmentation method described in **Chapter 3** to a patient dataset,

comparing the resulting segmentations and dosimetry to current clinical practice. Finally, **Chapter 7** investigates the lung absorbed dose measured on ^{90}Y PET post-radioembolization and the occurrence of radiation pneumonitis. Since, so far, no cases of radiation pneumonitis have been reported for ^{166}Ho radioembolization, the assessment of lung absorbed dose following ^{90}Y radioembolization can give insight into a lung absorbed dose limit applicable also to ^{166}Ho radioembolization.

This thesis concludes with a summary and general discussion in **Chapter 8**.
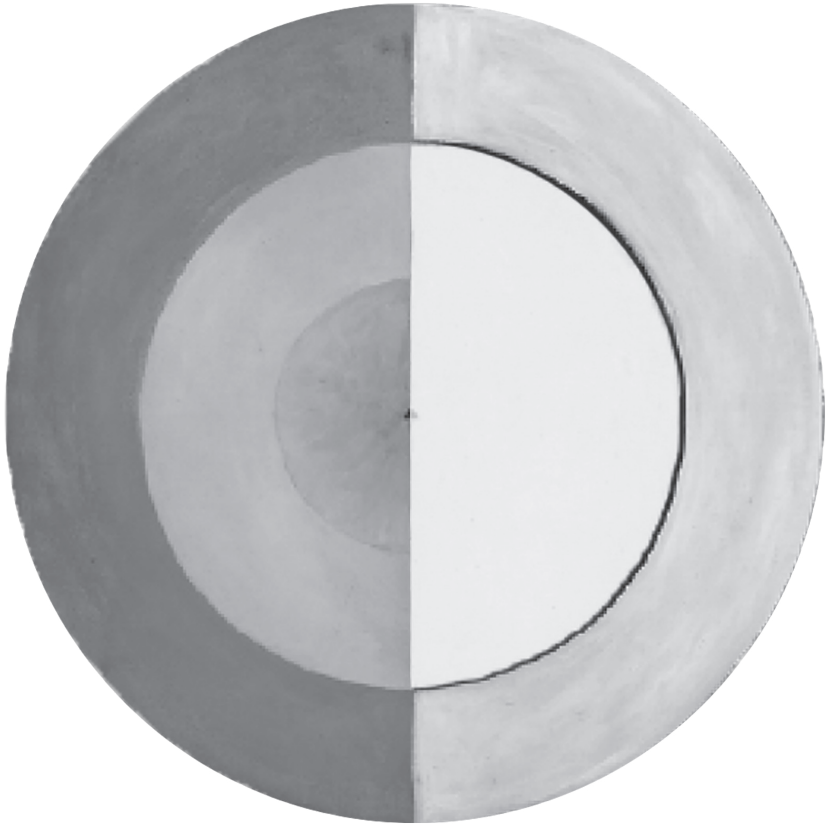
PART I

^{166}Holmium SPECT imaging

CHAPTER 2

Gamma camera characterization at high ^{166}Holmium activity

Abstract

Background: High activities of holmium-166 ([166]Ho)–labeled microspheres are used for therapeutic radioembolization, ideally directly followed by SPECT imaging for dosimetry purposes. The resulting high count rate potentially impacts dead time, affecting image quality and dosimetric accuracy. This study assesses gamma camera performance and SPECT image quality at high [166]Ho activities of several GBq.

Methods: To this purpose, the liver compartment, including two tumors, of an anthropomorphic phantom was filled with [166]Ho-chloride, with a tumor to non-tumorous liver activity concentration ratio of 10:1. Multiple SPECT/CT scans were acquired over a range of activities up to 2.7 GBq. Images were reconstructed using a commercially available protocol incorporating attenuation and scatter correction. Dead time effects were assessed from the observed count rate in the photopeak (81 keV, 15% width) and upper scatter (118 keV, 12% width) window. Post reconstruction, each image was scaled with an individual conversion factor to match the known total activity in the phantom at scanning time. The resulting activity concentration was measured in the tumors and non-tumorous liver. Image quality as a function of activity was assessed by a visual check of the absence of artifacts by a nuclear medicine physician. The apparent lung shunt fraction (nonzero due to scatter) was estimated on planar and SPECT images.

Results: A 20% count loss due to dead time was observed around 0.7 GBq in the photopeak window. Independent of the count losses, the measured activity concentration was up to 100% of the real value for non-tumorous liver, when reconstructions were normalized to the known activity at scanning time. However, for tumor spheres, activity concentration recovery was ~80% at the lowest activity, decreasing with increasing activity in the phantom. Measured lung shunt fractions were relatively constant over the considered activity range.

Conclusion: At high [166]Ho count rate, all images, visually assessed, presented no artifacts, even at considerable dead time losses. A quantitative evaluation revealed the possibility of reliable dosimetry within the healthy liver, as long as a post-reconstruction scaling to scanning activity is applied. Reliable tumor dosimetry, instead, remained hampered by the dead time.

Background

Holmium-166 ([166]Ho) radioembolization (QuiremSpheres™, Quirem Medical B.V., The Netherlands) is a well-established treatment for primary and secondary tumors in the liver [20]. This procedure consists of injecting radioactive microspheres via a microcatheter in the hepatic artery. The microspheres preferentially lodge in the tumors' arterioles and [166]Ho, being a beta emitter, irradiates the tumor cells, sparing the healthy liver. In [166]Ho radioembolization, single photon emission computed tomography (SPECT)/CT is used for dosimetry purposes both for treatment planning and post-treatment evaluation, relying on the additional 80.6 keV gamma emission of [166]Ho. In the pre-treatment phase, the distribution of low activity [166]Ho-microspheres (i.e. scout dose, 250 MBq, QuiremScout™, Quirem Medical B.V., The Netherlands) can be directly translated to microsphere distribution at therapeutic levels and can be used to identify potential extrahepatic depositions [21]. In the post-treatment phase, the actual therapeutic activity distribution is assessed to establish a dose response relation or to verify whether a sufficient absorbed dose was delivered to tumor tissue in individual cases. When using [166]Ho-microspheres, approximately 3.8 GBq of [166]Ho is injected per kg of treated liver mass [19] in order to deliver 60 Gy to the injected liver portion, as indicated by the manufacturer, and assuming a homogenous uptake throughout the liver. This typically results in injected activities of 5-10 GBq. Although the abundancy of the 80.6 keV [166]Ho photopeak is only 6.7%, the count rate immediately after treatment is very high. This is a consequence of the occurrence of multiple gamma emissions in the MeV range (1.38 MeV/0.93%, 1.58 MeV/0.19%, 1.66 MeV/0.12%) of the [166]Ho spectrum, causing interactions within the patient, collimator and crystal. Furthermore, there is a considerable amount of bremsstrahlung, caused by β^- (E_{max}:1.77Mev/49%, 1.85MeV/50%) interactions within the patient [22][23]. This potentially impacts image quality and quantitative accuracy because of gamma camera dead time effects. For accurate post-treatment dosimetry, a time interval between [166]Ho treatment and image acquisition is therefore used in clinical practice, which, given the 26.8 hours half-life, is typically 3-5 days post-treatment. However, this may be undesirable from a logistical perspective.

This study aimed to assess SPECT image quality for a range of [166]Ho activities, from 447 MBq extending up to 2.7 GBq (equivalent to a treatment-imaging interval of approximately two days in a clinical scenario). In addition, the possibility to perform relative dosimetry within healthy liver and tumors, at different activity concentrations, was investigated.

In a preliminary study [22], Elschot *et al.* evaluated scintillation camera characteristics for isotopes used in liver radioembolization, including [166]Ho. To this purpose, a NEMA image

quality phantom was used, and a comparison between isotopes using various collimators, to optimize acquisition parameters and to support future analyses of clinical comparisons between radioembolization studies was systematically performed. Additionally, the count rate linearity of the camera (Philips FORTE) was assessed. However, the count rate linearity was determined indirectly, combining the measured system sensitivity with an *intrinsic* count rate curve (i.e., measured on a spectrum without patient Compton scatter nor collimator interactions).

In this study, a further investigation mimicking patient geometry and clinical protocol for image acquisition and reconstruction is presented, including the effect of patient scatter and pulse-pile at high count rate. The outcome of this analysis may be used to further optimize imaging protocols and to create guidelines for [166]Ho SPECT acquisition in clinical practice, especially for the purpose of quantitative SPECT imaging for post-treatment dosimetry.

Materials and Methods

To estimate the effect of dead time and count pile-up, count rate performance and measured activity concentration were assessed, considering the total activity at scanning time. Image quality was evaluated by a nuclear medicine expert (experience > 5 years) who visually checked the absence of image artifacts. Measured lung shunt fractions ($LSF_{measured}$) for the considered range of activities were determined on both planar and SPECT acquisitions. Activity in the phantom was limited to 2.7 GBq to limit radiation dose to the investigators (due to filling and frequent handling of the phantom).

Phantom characteristics

An anthropomorphic phantom (model ECT/TOR/P), including lungs and liver, was used to mimic patient anatomy (**Figure 2.1**). Two spheres (S1 and S2) were placed in the liver to resemble tumors of different sizes. The liver compartment (1205 mL) and spheres (S1: volume = 24.2 mL, radius = 1,79 cm and S2: volume = 15.7 mL and radius = 1,55 cm) were filled with [166]Ho-chloride with a tumor to non-tumorous liver activity concentration ratio of 10:1, resembling a high tumor-to-non-tumor uptake, typically reported for large, highly vascularized tumors [24][25].

This resulted in an activity percentage, with respect to the total activity in the liver, equal to 15.10% for S1 and 9.76% for S2.

By letting the activity decay, multiple SPECT/CTs were acquired over several days to obtain a range of activities from 447 MBq up to 2.7 GBq. No radioactivity was injected into the lung compartment of the phantom.
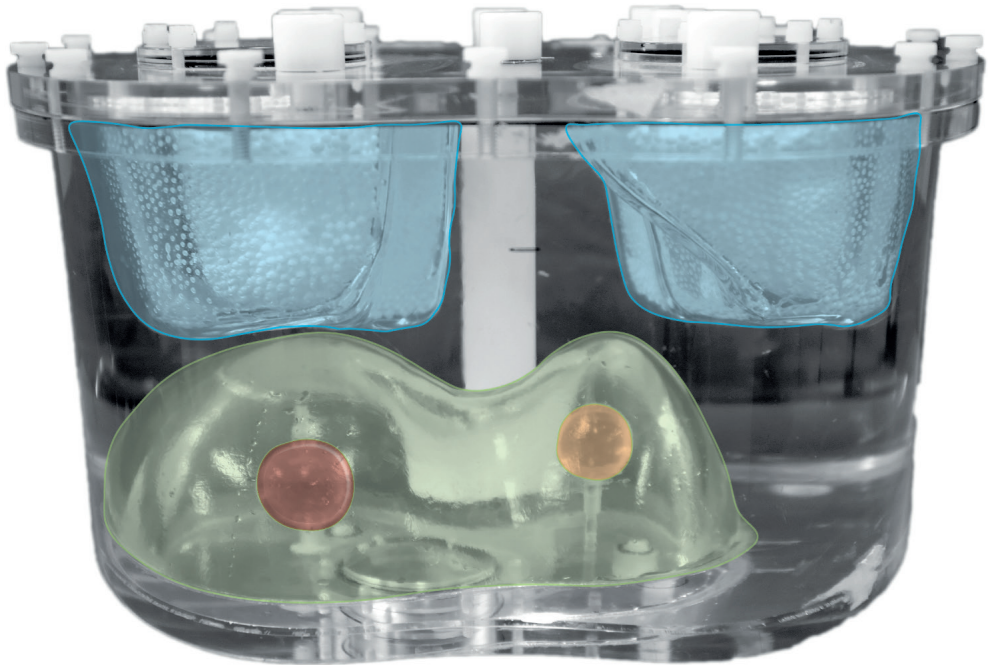
Figure 2.1

A photograph of the anthropomorphic phantom model ECT/TOR/P used for the experiment with VOIs superimposed. Lung region is colored in light blue, liver compartment in green, sphere S1 in red and S2 in orange.

Data Acquisition

A total of 16 measurements were performed. All images were obtained using Symbia SPECT/CT scanners, (Siemens, Erlangen, Germany), using medium-energy collimators. Of the 16 measurements, 10 were acquired on a Symbia T16 scanner and 6 on a Symbia T scanner. Projections were recorded in the 81 keV (15% width) photopeak window on a 128 x 128 matrix (pixel spacing, 4.8 x 4.8 mm), with 120 angles (20 s per projection) over a non-circular 360° orbit using step-and-shoot mode. An additional energy window centered at 118 keV (12% width) was used to correct the [166]Ho photopeak data for scatter from higher energy gamma emissions and bremsstrahlung using a window-based scatter correction.

The imaging protocol was adopted from the clinical protocol used in patients after a radioembolization treatment. Prior to every measurement, the energy spectrum as recorded by the gamma camera was stored (**Figure 2.2** panel **A**).
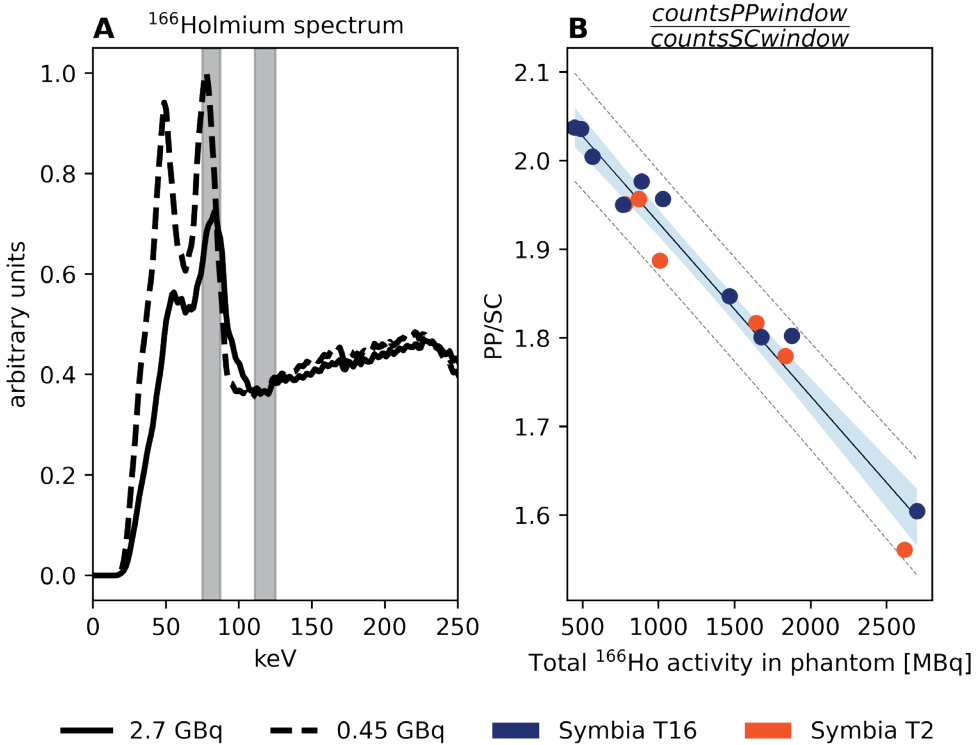
Figure 2.2

Panel **A** depicts the [166]Ho spectrum acquired for dead times equal to 42.25% (solid line), corresponding to a total phantom activity of 2.7 GBq and 9.25% (dashed line), corresponding to 447 MBq. The curves were scaled for comparison by matching the sum of the counts in the scatter window centered at 118 keV (12% width). The main [166]Ho photopeak window (80.6 keV, 15% width) and the scatter window (118 keV, 12% width) are represented by the gray areas. The effect of pulse pile-up due to the high count rate is visible as the shifting and broadening of the photopeak. Panel **B** shows the ratio between the mean of counts in the 81 keV photopeak window and the 118 keV upper scatter window within the recorded spectra, plotted as function of total activity in the phantom at time of recording. Linear regression is represented by the black line, while gray dashed lines represent prediction intervals. Data in the blue area are within the confidence intervals.

Before SPECT scans, planar images of the lungs and liver area were acquired (5-min acquisition, 256 x 256 matrix), according to the protocol currently in use for patients. The detectors were positioned to acquire anterior and posterior images. Data were acquired in a 74.6 – 86.6 keV energy window with the medium-energy low penetration collimators mounted.

Data Reconstruction

Images were reconstructed using commercially available software (Flash 3D; Siemens), with 10 iterations, 8 subsets, incorporating scatter and attenuation correction. No Gaussian smoothing was applied. The total downscatter estimate in the 81 keV window included scattered photons originating from higher energy emissions (including bremsstrahlung from the β− emissions), but not the photopeak scatter (originating from the primary 81 keV photopeak). This contribution can be estimated from the 118 keV window, using the k-factor. The k-factor used to correct the photopeak window for downscatter was previously estimated [26][27] and adopted in this study.

No scatter correction was applied to planar acquisitions.

Data Analysis

To characterize the gamma camera count-rate performance, counts in the [166]Ho photopeak window were plotted against total activity in the phantom at scanning time (**Figure 2.3**). The paralyzable detector model (PDM), valid within the considered count range [28], was fitted to the data and forced to pass through the axis origin, to obtain the linear response coefficient and activity at 20% count loss.

Reconstructions were converted into units of Bq by applying a conversion factor based on the known activity in the phantom at the time of scanning. For every reconstruction, a conversion factor was determined by summing the values within a VOI encompassing the liver, enlarged by two centimeters to compensate for spill-out (partial volume effect), and dividing by the activity in the phantom.

The quality of the reconstructed images was assessed visually, by a nuclear medicine physician, and quantitatively evaluating the measured activity concentrations and $LSF_{measured}$. Multiple volumes of interest were defined for the two spheres (S1 = 24.2 mL and S2 = 15.7 mL) within the liver, the liver compartment, and lungs. The VOIs for the liver and lungs were semi-automatically delineated on the CT images, using ITK-SNAP [29], and subsequently registered onto the corresponding SPECT images using the affine transformation between both coordinate systems. The spheres were instead defined on the SPECT reconstruction as spherical VOIs with radius corresponding to the nominal spheres radius enlarged by 1 cm, to compensate for the partial volume effect (PVE). The size of the spheres radius enlargement was empirically determined by iterative increments of radius size until the effect of PVE was mostly compensated. At this amount of sphere radius dilation, approximately 25% of the

activity in the sphere VOI is due to the background, which is corrected for, as shown in the equation (I). This ensures that most of the activity recovered in the spheres is actually present within the nominal sphere's volume.

Finally, to obtain the non-tumor VOI (non-tumorous liver) mask, the dilated sphere VOIs were subtracted from the liver VOI, eroded by 1 cm to compensate for the spill-out near the edge.

To assess the possibility of dosimetry in the considered compartments, tumorous and non-tumorous liver, at high counts rate, activity concentration recovery (ACR) was considered.

ACR for spheres was computed as follow:

$$ACR_{sphere} = \frac{C_s}{C_{ns}} \text{ x } 100\% = \frac{\frac{A_d}{V_s} - \frac{C_b(V_d-V_s)}{V_s}}{Cn_s} \text{ x } 100\% \tag{I}$$

Where C_s is the measured activity concentration in the sphere, C_{ns} the nominal activity concentration in the sphere, V_s the nominal sphere's volume, A_d the measured activity in the dilated sphere, V_d the volume of the dilated sphere and C_b the measured the activity concentration in the background. The term $\frac{C_b(V_d-V_s)}{V_s}$ compensates for the recovered activity in the dilated sphere VOI due to activity background.

For the non-tumorous liver background compartment, ACR was computed as:

$$ACR_{liver\ background} = \frac{C_{lb}}{C_{nl}} \text{ x } 100\% \tag{I I}$$

Where C_{lb} is the measured activity concentration and C_{nl} the nominal activity concentration in the liver background.

The Spearman rank correlation coefficient (ρ) between the measured activity concentration and total activity in the phantom at scanning time was computed for each VOI: non-tumorous liver, S1 and S2.

To assess the LSF$_{measured}$, two approaches were used: planar imaging-based and SPECT-based. For both approaches, the scatter in the lungs was computed, in line with clinical practice, as:

$$LSF_{measured} = \frac{counts_{Lungs}}{counts_{Lungs} + counts_{Liver}} \text{ x } 100\% \tag{III}$$

For the planar-based method, the counts were computed using the geometric mean following standard clinical practice [30], while for the SPECT-based method, counts within the lung and liver VOIs were considered. Since the lungs compartment of the phantom was not filled with any activity, the nominal lung shunt fraction, $LSF_{nominal}$, was 0 across the range of considered activities.

To visually assess image quality, a nuclear medicine physician (AB, experience >5 years) was randomly and blindly presented the reconstructed images, and asked to visually check the absence of image artifacts.

Results

Figure 2.2 panel **A** depicts the measured ^{166}Ho spectrum, acquired at 2.7 GBq and 447 MBq, indicating the transformation of the measured spectra due to pulse pile-up. The dead-time percentage, indicated by the scanner, was 42% and 9% respectively. The two spectra were normalized for the sum of counts in the scatter window centered at 118 keV (12% width), to allow for a visual comparison between them.

The spectrum acquired at 2.7 GBq presented deformations related to the high counts regime in which it was acquired, affected by increasing non-linear phenomena like the pulse pile-up effect and dead time. The ratio between mean counts in the main photopeak window (75 – 87 KeV) and in the scatter window (111 – 125 keV) is depicted in **Figure 2.2** panel **B**, as function of total activity in the phantom. The resulting correlation coefficient between count ratio and activity at scanning time is -0.93 (p-value = 1.94e^{-7}), with a linear regression line of $y = 2.1 - \frac{0.09}{GBq}$. This relation emphasizes the limitation of using a fixed k-factor, independent of ^{166}Ho activity, to compensate for scatter.

The count rate curve in the 81 keV photopeak window is shown in **Figure 2.3**. For both Symbia T16 and T2, the PDM model was fitted to the measured count rate data, and forced to pass through the axis origin. Dead time influenced the ideally linear relation between activity and counts recovered ($C(A) = \alpha A$), leading to a progressive count loss with increasing activity. The activity at which the 20% count loss was reported ($R_{20\%}$) was recovered at 714 MBq and 762 MBq for Symbia T2 and Symbia T16 respectively.
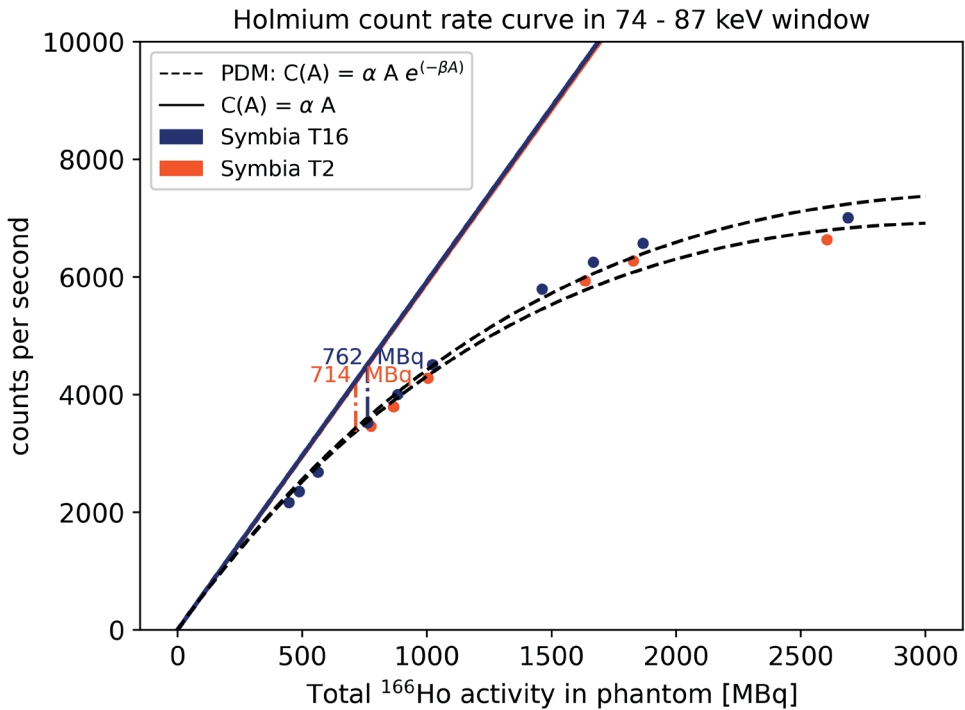
Figure 2.3

Count rate measured on a Siemens Symbia T16 and T2. Linear model, C(A) = αA, is depicted by the solid lines and the paralyzable dead time model (C(A) = αAe$^{-βA}$) by dashed lines. Values for 20% count loss are reported: 714 MBq for Symbia T2 and 762 MBq for Symbia T16.

Conversion factors for reconstruction units to Bq, based on the known activity in the phantom at the time of scanning, are plotted in **Figure 2.4** panel **A**, as a function of total activity. Activity concentration recovery as a function of total activity in the phantom is reported in **Figure 2.4** panel **B**, **C** and **D** for non-tumorous liver, S1 and S2, respectively. The non-tumorous liver compartment showed a non-significant (p-value = 0.34) correlation with activity (ρ =0.256), with a mean ± standard deviation of 101.2 ± 1.8%. The activity concentration recoveries in the tumor compartments S1 and S2 were negatively correlated with activity (ρ =-0.97, p-value = 2.28e^{-10}, and ρ = −0.77, p-value = 4.77e^{-4}, respectively), with linear regression lines of y = 85.6% (1 - $\frac{0.10}{GBq}x$) and y = 78.4% (1 - $\frac{0.03}{GBq}x$).

No artifacts were reported in the images, when visually assessed by a nuclear medicine expert.
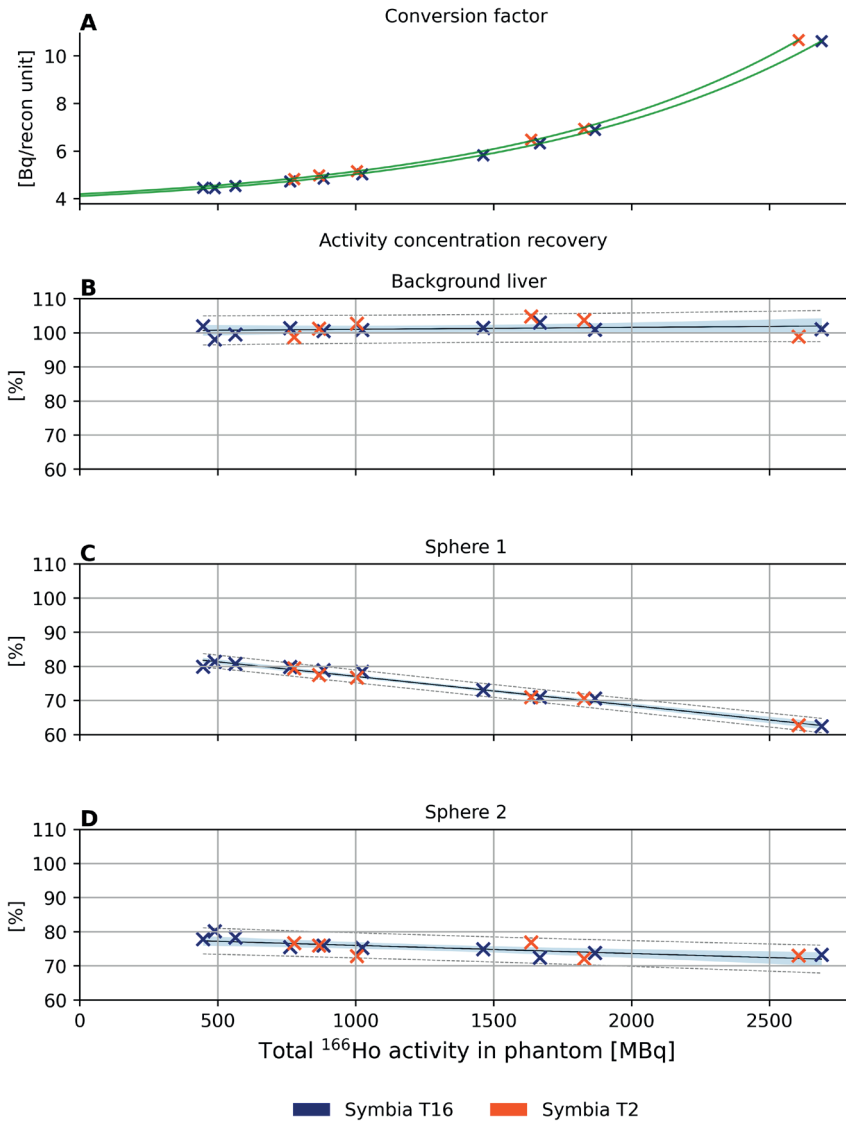
Figure 2.4

Panel **A** depicts the individual conversion factor between Bq and reconstruction values computed for each measurement based on the total activity in the phantom at the scanning time. Its trend, as function of activity, is reported together with the individual measurements. Panel **B**, **C** and **D** show the activity concentration recovery as function of total activity in phantom at scanning time for non-tumorous liver, sphere S1 and sphere S2, respectively. A complete activity concentration recovery is obtained for non-tumorous liver (panel **B**) while partial recovery for the spheres (panels **C** and **D**). Linear regression is represented by the black line, while gray dashed lines represent prediction intervals. Data in the blue area are within the confidence intervals.

LSF$_{measured}$ is shown in **Figure 2.5** for both the planar-based approach (top panel) and SPECT-based approach (bottom panel). Despite the LSF$_{nominal}$ was equal to 0, mean and standard deviations of the measured lung shunt fraction were 21.16% ± 0.55% for the planar-based method and 1.57% ± 0.19% for the SPECT-based method. The corresponding linear regression lines were $y = 20.2\%\,(1 - \frac{0.04}{GBq}x)$ and $y = 1.2\%\ (1 - \frac{0.25}{GBq}x)$. Correlation with activity was 0.85 (p-value = 3.70e^{-3}) and 0.95 (p-value = 8.76e^{-5}) for the planar- and SPECT-based method respectively.
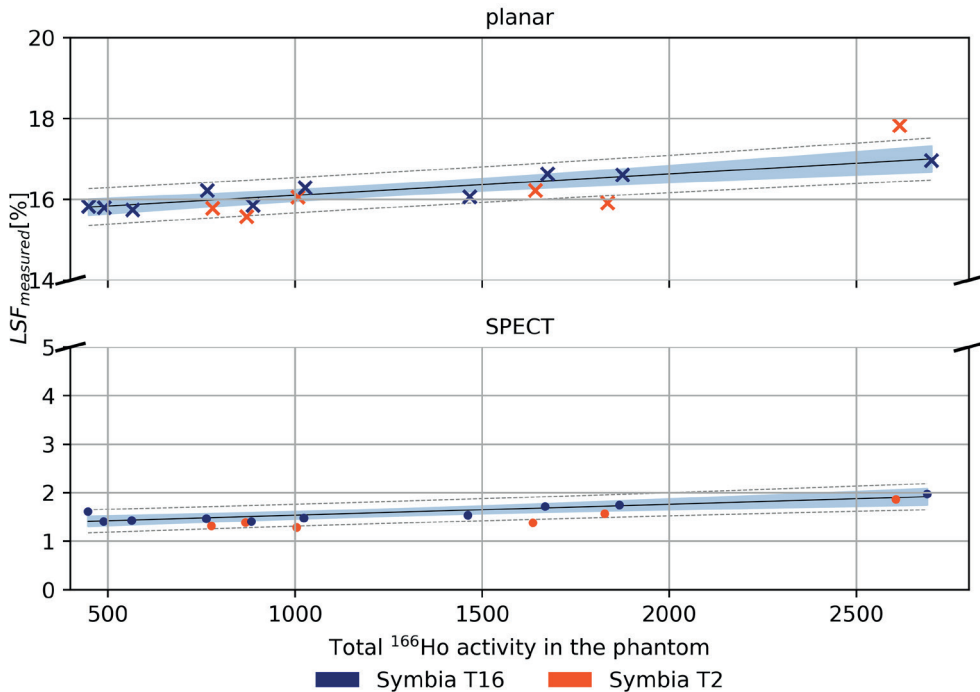
Figure 2.5
LSF$_{measured}$ in the lungs based on planar images (top panel) and SPECT reconstructions (bottom panel). Linear regression is represented by the black line, while gray dashed lines represent prediction intervals. Data in the blue area are within the confidence intervals.

Discussions

Count rate saturation and its effect on quantification is of importance for radiation peri-therapeutic dosimetry in nuclear medicine imaging. The impact of high activity on dead time and pulse pile-up was evident in the recorded energy spectra (**Figure 2.2** panel **A**), where a relatively lower ^{166}Ho photopeak was registered for the spectrum acquired during high count

rate, corresponding to a total activity in the phantom of 2.7 GBq. With increasing count rate, the amount of relative scatter is increasing, which is evident in **Figure 2.2** panel **B**) where the ratio between mean of counts in the main photopeak and in the scatter window decreased with increasing activity. In our study, activity values corresponding to a 20% count loss were 714 MBq and 762 MBq for Symbia T2 and T16, respectively. In the work by Elschot *et al.* [22], a value for the A_{linmax}, defined as the highest activity with less than 2% loss of count rate, of approximately 1.5 GBq was reported. The difference between these findings and the values reported in the current work may be explained by the different gamma cameras employed and the different methods used for the measurements. In the previous study, a Philips FORTE gamma camera was used. This camera operates a "high count rate mode", which is automatically activated at count rates above 20 kcps [31]. Moreover, to determine the A_{linmax} an indirect approach was taken [22], which included the measurement of an intrinsic count rate curve (i.e. acquired without collimators) of an activity-filled vial in the full energy window, combined with separate measurements of the system sensitivity using a Petri dish with a thin layer of activity, hence without scatter material producing scattered photons and bremsstrahlung, in both the full energy window and the photopeak window, underestimating the intrinsic count rate. Moreover, as can be appreciated from **Figure 2.2**, dead-time effects become increasingly detrimental for a narrow photopeak window. In the present study, therefore, the focus was on mimicking patient geometry in a clinical scenario, directly measuring the number of counts in the main photopeak window for a range of activities.

This former study showed that the use of a single conversion factor for quantification is insufficient for activities above several hundreds of MBq and that dead time effects need to be taken into account. The challenges of this process may be avoided altogether by scaling reconstructions to the known injected activity on a patient-to-patient basis, on the assumption that all of the activity is within the field of view. Using this scaling method, the activity concentration recovery in the liver compartment presented values close to 100%, regardless of total activity. This paves the way to a reliable assessment of absorbed dose in the healthy liver up to at least 2.7 GBq. This method may be used for dosimetric assessment of healthy liver absorbed dose, a decision driving parameter in radioembolization procedures.

Tumor dosimetry based on [166]Ho SPECT/CT is challenging, especially when relying on standard commercially available reconstruction methods. These methods do not take into account the full emission spectrum and bremsstrahlung, and typically rely on energy window based scatter correction methods. The triple energy window method is inadequate for [166]Ho due to the characteristic lead X-ray emission lines around 74 keV, just below the [166]Ho photopeak. Reconstructions using dedicated Monte Carlo methods significantly improve

image quality [32], but are typically not available for standard clinical use. Because of this, standard clinical [166]Ho reconstructions are hampered by poor resolution due to a large partial volume effect and contain photopeak scatter and lead X-ray contamination.

At the high activity levels typically encountered after therapy, dead time effects become significant as well. Dead time effects add further issues to be considered when aiming at adequate dosimetry in the tumor compartments.

The impact of the dead time effect can be observed in the decrease of the activity concentration recovery for the spheres (representing tumors). Hence, at high [166]Ho count rate, tumor dosimetry performed on clinically reconstructed SPECT scans is impaired even more.

The limitation due to the high count regime is made clear when NEMA Image Quality (IQ) measurements are performed. The contrast recovery coefficients, for the nominal VOIs of the spheres, range from 9% for the smallest sphere (volume = 0.52 mL) to 47%, for the largest sphere (volume = 26.52 mL), showing the impact of the PVE. When the sphere VOI is dilated to correct for the PVE, using the same approach as presented for the anthropomorphic phantom used in this study, an increase in the contrast recovery coefficient is observed. However, this increase leads to a recovery of approximately 80%, which is in line with the activity concentration recovery obtained for the S1 and S2 spheres at lowest activities (see **Figure 2.4** panel **C** and **D**), where the effect of the high-count regime was minor. This incomplete recovery is partly due to the suboptimal scatter correction method and was analysed in details in the work by Elschot *et al.* [32] where several reconstruction methods were compared against one another for the computation of the contrast recovery coefficient, as function of NEMA IQ phantom sphere volumes.

Despite no activity was present in the lung compartment, $LSF_{nominal} = 0$, activity was measured in the lungs due to scatter. This phenomenon, quantified through $LSF_{measured}$, using both planar and SPECT images, confirmed the superiority of SPECT images for lung shunt estimation [9], [33]. However, it is interesting to notice that, for both planar and SPECT images, $LSF_{measured}$ was only slightly affected by the high count rate.

The study was conducted under the assumption that all the injected activity was within the imaged field of view, and considering the measurement of residual activity a mandatory clinical practice. This allowed to the computation of the total injected activity in the patient to properly scale the reconstructed scans. This study has indeed showed that, at high [166]Ho count rate, the scaling to the activity at scanning time plays a determinant role. However, for tumors VOI, where the activity concentration was higher, this approach was not sufficient

to obtain a complete activity concentration recovery in the considered activity range, as it happened for the non-tumorous liver.

Some limitations apply to the study: images were acquired with a specific scanner, thus the measurements reported in this study are vendor-specific. Moreover, administered activities for radioembolization procedures can be up to 10 GBq or more, while in this study the maximum total activity in the phantom was 2.7 GBq. In addition, the tumor to non-tumorous liver ratio, even though realistic, was fixed and thus it was not possible to assess gamma camera performance for different concentration ratios. Similarly, total tumor volume was limited to 40 mL (1200 mL total liver volume), whereas much larger volumes are often encountered. Moreover, during a patient scan, breathing artifacts and patient movement can play an important role. Notwithstanding this, an anthropomorphic phantom has the advantage to better mimic the average patient volume characteristics compared to the NEMA Image Quality phantom.

In the future, a similar experiment including breathing motion may be conducted, analyzing different possible methods to correct the consequent artifacts.

Conclusion

^{166}Ho quantitative reconstructions are deeply affected by the high count regime, requiring a scaling to the total activity at the scanning time, making its accurate knowledge mandatory. If properly scaled, ^{166}Ho reconstructions acquired up to 2.7 GBq provide reliable healthy liver dosimetry. However, tumor dosimetry remains inadequate, further challenged by the increasing dead time effect. At high count rate, no images artifacts are reported. Measured lung shunt fractions were relatively constant, independent of total activity.

CHAPTER 3

^{166}Holmium–^{99m}Technetium dual-isotope imaging

Abstract

Background: Partition modelling allows personalized activity calculation for holmium-166 (^{166}Ho) radioembolization. However, it requires the definition of tumor and non-tumorous liver, by segmentation and registration of a separately acquired CT, which is time-consuming and prone to error. A protocol including ^{166}Ho-scout, for treatment simulation, and technetium-99m (^{99m}Tc) stannous phytate for healthy liver delineation was proposed. This study assessed the accuracy of automatic healthy liver segmentation using ^{99m}Tc images derived from a phantom experiment. In addition, together with data from a patient study, the effect of different ^{99m}Tc activities on the ^{166}Ho-scout images was investigated.

Methods: To reproduce a typical scout procedure, the liver compartment, including two tumors, of an anthropomorphic phantom was filled with 250 MBq of ^{166}Ho-chloride, with a tumor to non-tumorous liver activity concentration ratio of 10. Eight SPECT/CT scans were acquired, with varying levels of ^{99m}Tc added to the non-tumorous liver compartment (ranging from 25 to 126 MBq). For comparison, forty-two scans were performed in presence of only ^{99m}Tc from 8 to 240 MBq. ^{99m}Tc image quality was assessed by cold-sphere (tumor) contrast recovery coefficients. Automatic healthy liver segmentation, obtained by thresholding ^{99m}Tc images, was evaluated by recovered volume and Sørensen-Dice index. The impact of ^{99m}Tc on ^{166}Ho images and the role of the downscatter correction were evaluated on phantom scans and twenty-six patients' scans by considering the reconstructed ^{166}Ho count density in the healthy liver.

Results: All ^{99m}Tc image reconstructions were found to be independent of the ^{166}Ho activity present during the acquisition. In addition, cold-sphere contrast recovery coefficients were independent of ^{99m}Tc activity. The segmented healthy liver volume was recovered fully, independent of ^{99m}Tc activity as well. The reconstructed ^{166}Ho count density was not influenced by ^{99m}Tc activity, as long as an adequate downscatter correction was applied.

Conclusion: The ^{99m}Tc image reconstructions of the phantom scans all performed equally well for the purpose of automatic healthy liver segmentation, for activities down to 8 MBq. Furthermore, ^{99m}Tc could be injected up to at least 126 MBq without compromising ^{166}Ho image quality.

Background

Holmium-166 (^{166}Ho) radioembolization is an established treatment for liver malignancies [34]. The current clinical practice for ^{166}Ho radioembolization includes pre-treatment planning and treatment, together with post-treatment verification. The pre-treatment phase can be performed using QuiremScout™ (Quirem Medical B.V., The Netherlands), particles which are shaped identical to the microspheres used for the treatment, ^{166}Ho-microspheres (QuiremSpheres™, Quirem Medical B.V., The Netherlands). Using the ^{166}Ho-microspheres for both procedures (pre-treatment and treatment) has the benefit of improving the intrahepatic distribution prediction in comparison with current clinical standard (technetium-99m macroaggregated albumin or ^{99m}Tc-MAA)[21]. The activity distribution imaged in this phase serves as a predictor for the radiation dose distribution during the treatment, and can be used to avert a potential extrahepatic deposition. In addition, it enables partition modelling [35] which allows a personalized activity calculation for ^{166}Ho radioembolization. However, this requires segmentation of tumors and non-tumorous tissue on anatomical images, which is typically performed using a complementing contrast enhanced CT, usually acquired up to weeks before the treatment. Consequently, these segmented volumes of interest (VOIs), tumors and non-tumorous area, should be registered to the SPECT/CT to perform dosimetry. A similar workflow applies to the post-treatment phase, to assess treatment outcome and response. So far, manual segmentation and manual image registration are currently most commonly applied in clinical practice. These manual processes are time-consuming, prone to error and introduce inter-observer variability. Therefore, a protocol to automatically segment and register the VOIs would tackle these drawbacks, allowing an automatic workflow for planning and evaluation of the treatment. To this purpose, a dual-isotope protocol was suggested by Lam *et al.* in [14]. It is based on ^{166}Ho microspheres, which serve as treatment simulation, and technetium-99 m (^{99m}Tc) stannous phytate, which accumulates in the healthy liver tissue and provides a healthy liver demarcation (^{166}Ho-^{99m}Tc dual isotope protocol). These two compounds can be imaged simultaneously with a single SPECT acquisition and then be reconstructed into two images: ^{166}Ho and ^{99m}Tc, avoiding any registration procedure.

However, the presence of the two radionuclides leads to a reciprocal influence between the two (depicted in **Figure 3.1**), which has to be taken into account during the image reconstruction phase. In particular, the ^{166}Ho main photopeak, at 81 keV, is affected by the downscatter from ^{99m}Tc, which has its main photopeak at 140 keV. Vice versa, ^{99m}Tc is contaminated by downscatter from the ^{166}Ho high energy gamma emissions and bremsstrahlung.
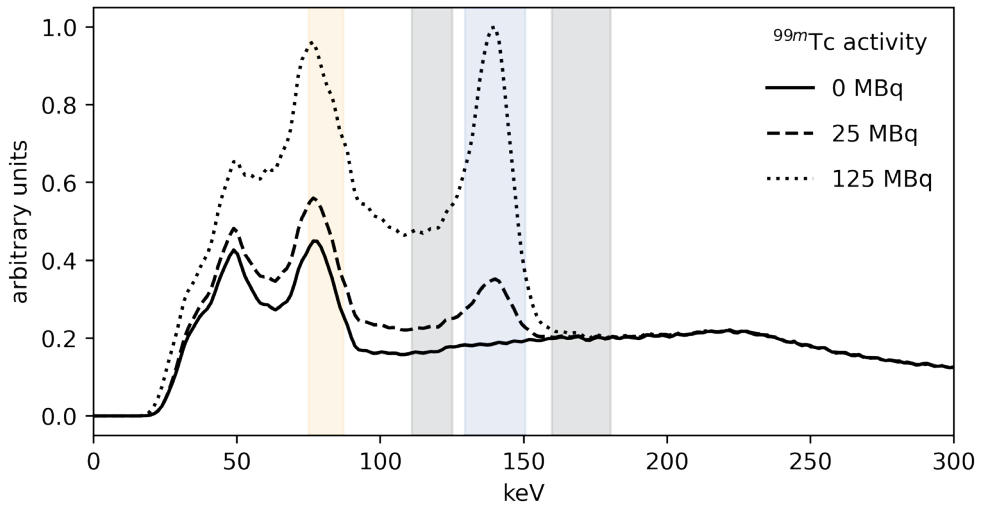
Figure 3.1

Spectra recorded by the SPECT scanner of an anthropomorphic phantom filled with ^{166}Ho and ^{99m}Tc. Curves are depicted for ^{166}Ho:^{99m}Tc activity combinations (in MBq) of: 282:0 (solid line), 268:25 (dashed line), and 250:125 (dotted line). The curves were scaled such that the tails of the spectra overlap for visual comparison: the relative difference between the spectra is attributed to ^{99m}Tc. Orange and blue areas represent the ^{166}Ho and ^{99m}Tc photopeak windows, respectively; while the grey areas depict the scatter windows (see **Table 3.2**).

The ^{166}Ho-^{99m}Tc dual isotope protocol is currently implemented in our institute using 50 MBq of ^{99m}Tc administered right after 250 MBq ^{166}Ho scout, leading to a ^{166}Ho:^{99m}Tc activity ratio of 5. The decision to use this particular ratio was based on the results of a phantom study together with visual interpretation and consensus reading by two nuclear medicine physicians and a medical physicist [15]. Within the clinical practice, ^{166}Ho-^{99m}Tc dual isotope scans are reconstructed using 3D OSEM algorithm (Flash 3D; Siemens). The impact of this protocol on ^{166}Ho image quality was investigated through a comparison between patient scans, acquired before and after the additional ^{99m}Tc injection [27].

This current study expands on the previous work by van Rooij *et al.* [5] who used a Monte Carlo based reconstruction method to correct for the crosstalk interactions between the two isotopes. However, because this reconstruction method is not available for everyday clinical practice, the current study focuses on the applicability of the ^{166}Ho-^{99m}Tc dual isotope protocol in the clinical scenario, using commercially available reconstruction software. The impact of different ^{99m}Tc activities on the ^{166}Ho-scout image quality, and vice versa, the impact of ^{166}Ho scout on ^{99m}Tc image quality and the accuracy of healthy liver segmentation were investigated using scans

reconstructed according to the clinical protocol. To understand the impact of ^{99m}Tc on ^{166}Ho image quality and its associated effect on downscatter correction during image reconstruction, ^{166}Ho image quality has been assessed by multiple metrics. Image uniformity, contrast recovery coefficients and ^{166}Ho count density, i.e. the voxel value in ^{166}Ho reconstructions, were measured for various amounts of ^{99m}Tc activity, investigating their dependency on the k-factor used for ^{166}Ho image reconstruction. This will make the ^{166}Ho-^{99m}Tc dual isotope protocol more suitable for its adoption in ^{166}Ho radioembolization practice, independent of the treatment institution.

Materials and Methods

To investigate ^{99m}Tc image reconstructions for the purpose of healthy liver segmentation during a ^{166}Ho-scout procedure, an anthropomorphic phantom using various concentrations of ^{99m}Tc in the healthy liver compartment in presence or not of ^{166}Ho was used. To mimic patient tumor/liver uptake, ^{166}Ho was injected in the healthy liver compartment. Two ^{166}Ho-filled spheres with a higher concentration resembling tumors with a high uptake were placed within the healthy liver compartment. ^{99m}Tc was added only to the healthy liver compartment and not to the tumors, simulating the expected distribution of ^{99m}Tc stannous phytate. For the ^{166}Ho-^{99m}Tc dual isotope study, the ^{166}Ho activity was held constant at 250 MBq (as per scout prescription) while ^{99m}Tc was varied across a range of activities.

^{99m}Tc image quality for varying levels of ^{99m}Tc activity was evaluated though several metrics: image uniformity, cold-sphere contrast recovery and the accuracy of healthy liver segmentations (obtained by thresholding). For comparison, these acquisitions were repeated without ^{166}Ho in the phantom in order to investigate the influence of ^{166}Ho on ^{99m}Tc reconstructions.

The effect that the addition of ^{99m}Tc has on ^{166}Ho images was investigated by comparing ^{166}Ho reconstructions from similar scans, performed with various amounts of ^{99m}Tc. Specifically, ^{166}Ho count densities (the voxel values in the reconstructions) in the healthy liver compartment were compared between reconstructions. To this end, phantom measurements and multiple patient scans were analyzed.

Details regarding the measurements and the corresponding metrics are summarized in **Table 3.1**.

Phantom

Phantom characteristics

An anthropomorphic phantom (model ECT/TOR/P), including lungs and liver, was used to mimic patient anatomy. Two fillable spheres (S1 and S2) were placed in the liver to resemble tumors of different sizes.

	Protocol	^{166}Ho [MBq]	^{99m}Tc [MBq]	Scans	Reconstruction	Aim	Metric
Phantom	^{166}Ho-^{99m}Tc dual isotope	250	25 - 126	8	^{166}Ho	Downscatter	^{166}Ho count density
						Uniformity	Coefficient of variation
					^{99m}Tc	Contrast	Cold-sphere contrast recovery
						Segmentation	Recovered volume
							Sørensen-Dice index
	^{99m}Tc only	0	8 - 240	42	^{99m}Tc	Uniformity	Coefficient of variation
						Contrast	Cold-sphere contrast recovery
						Segmentation	Recovered volume
							Sørensen-Dice index
Patients	^{166}Ho-^{99m}Tc dual isotope	224 (35)*	50	26	^{166}Ho	Downscatter	^{166}Ho count density difference
	^{166}Ho-only	224 (35)*	0	26	^{166}Ho		

Table 3.1

Summary of the experiments. *Median (and interquartile range) of administered activity among patient scout procedures.

For the ^{166}Ho-^{99m}Tc dual isotope measurements, the healthy liver compartment (1205 mL) and spheres (S1: volume = 24.2 mL, radius = 1.79 cm and S2: volume = 15.7 mL and radius = 1.55 cm) were filled with ^{166}Ho-chloride with a sphere to healthy liver compartment concentration ratio of 10:1, resembling a high tumor-to-non-tumor uptake, typically reported for large, highly vascularized tumors [24], [25]. This resulted in an activity percentage, with respect to the total activity in the liver, equal to 15.10 % for S1 and 9.76 % for S2. In order to consistently achieve an equivalent of 250 MBq of ^{166}Ho across the various measurements, which resembles the prescribed scout activity as used in the clinical studies [9], the imaging time for each scan was adjusted (17.8 sec to 38.2 sec per projection) with respect to the clinical protocol (20 sec per projection) to compensate for ^{166}Ho decay between scans. The validity of this approach was based on the assumption that the difference in dead time had little effect on count statistics. The measured dead time rate shifted on average from 4.5 % at the higher activities to 2.5 % at lower activities compensated by longer scanning time. ^{99m}Tc activity was injected multiple times in the healthy liver compartment leading to various ^{166}Ho:^{99m}Tc ratios, ranging from 2 to 10. Effective ^{99m}Tc activity, modified to correct for the varying imaging times, ranged from 25 to 126 MBq.

In a separate series of measurements, the anthropomorphic phantom was filled only with ^{99m}Tc in the healthy liver compartment (activity ranging from 8 to 240 MBq). These ^{99m}Tc-only measurements were used as reference for comparison of the ^{99m}Tc images acquired in presence of ^{166}Ho.

No radioactivity was injected into the lung compartment of the phantom, nor the torso compartment.

Phantom Data Acquisition

All images were obtained using a Symbia T SPECT/CT scanner (Siemens, Erlangen, Germany), using medium-energy collimators. Projections were recorded on a 128 x 128 matrix (pixel spacing, 4.8 x 4.8 mm), with 120 angles, over a non-circular 360° orbit using step-and-shoot mode. Energy windows used for image acquisition are summarized in **Table 3.2**.

Window name	Center of the energy window	Width of the energy window
^{166}**Ho photopeak**	81 keV	15%
Scatter$_{\_118}$	118 keV	12%
^{99m}**Tc photopeak**	140 keV	15%
Scatter$_{\_170}$	170 keV	12%

Table 3.2
Energy window characteristics

Phantom Data Reconstruction

All images were reconstructed using commercially available software (Siemens Flash3D), with 10 iterations, 8 subsets, incorporating scatter and attenuation correction. No post-reconstruction filtering was applied.

^{166}Ho–^{99m}Tc dual isotope downscatter correction

^{166}Ho images were reconstructed with window-based scatter correction, using projections acquired in the 118 keV energy window (scaled by a k-factor) as an estimate for downscatter in the 81 keV photopeak window originating from both ^{99m}Tc and higher-energy ^{166}Ho gamma emissions and bremsstrahlung.

Starting from the k-factor value previously computed by dividing the counts in the 81 keV and 118 keV energy window of ^{166}Ho-^{99m}Tc dual isotope projections [27], the k-factor for different ^{99m}Tc activities was empirically investigated by reconstructing ^{166}Ho images for a variety of k-factors ranging from 0.65 to 1.30 with a 0.05 interval. The optimal value of the k-factor was tuned by measuring, and minimizing, the impact of ^{99m}Tc activity on the ^{166}Ho count density measured on ^{166}Ho image reconstruction. Photopeak scatter, i.e., scattered photons originating from the 81 keV ^{166}Ho photopeak, was not accounted for.

^{99m}Tc images were reconstructed using the 118 keV and 170 keV windows for triple-energy-window scatter correction, the scatter was estimated as:

$$S_E = \left(\frac{C_L}{W_L} + \frac{C_U}{W_U} \right) \times \frac{1}{2} \times W_{PP} = \left(\frac{W_{PP}}{W_L \times 2} \right) \times C_L + \left(\frac{W_{PP}}{W_L \times 2} \right) \times C_U$$

Where C_L and C_U are the recorded projections for the lower (Scatter$_{118}$) and upper scatter (Scatter$_{170}$) windows respectively, and W_L, W_U and W_{PP} are the widths of the lower, upper and main photopeak energy windows.

For consistency, this method was also applied when no ^{166}Ho activity was present in the phantom.

Phantom Data Analysis

VOI definition

VOIs matching the phantom's liver compartment and sphere inserts were defined on a high resolution CT. The sphere VOIs were subtracted from the liver mask to produce the healthy liver compartment VOI. These pre-defined VOIs were registered to each SPECT/CT reconstruction using Elastix [36], [37]. Grid matrices were super-sampled to allow partial voxels to be included within the VOIs.

Uniformity

The healthy liver uniformity for different ^{99m}Tc activities was quantified by the coefficient of variation (COV), defined as the ratio of the standard deviation to the mean, computed within the healthy liver compartment VOI, for both ^{166}Ho and ^{99m}Tc reconstructions. The COV was computed for each ^{99m}Tc image, acquired either in presence or not of ^{166}Ho in the phantom. A binary erosion of 1 cm [38] on the healthy liver mask was applied to avoid edge effects.

Contrast recovery

Image quality can be assessed by analyzing the contrast recovery coefficient for either hot or cold spheres (Q_H or Q_C respectively), generally defined as:

$$Q = \frac{C_S / C_B - 1}{(R - 1)} \times 100\%$$

where, C_s is the mean intensity measured in the sphere VOI, C_B is the mean intensity measured in the healthy liver compartment VOI, and R is the nominal activity concentration

ratio between spheres and healthy liver compartment. However, for cold spheres, R is zero by definition.

The effect of adding ^{99m}Tc activity to the healthy liver compartment was assessed by measuring the contrast recovery coefficients on both ^{166}Ho and ^{99m}Tc reconstructions (Q_h or Q_c respectively). The nominal activity concentration ratio between spheres and healthy liver compartment, R, was 10 for ^{166}Ho reconstructions but since only ^{166}Ho was present in the spheres, and not ^{99m}Tc, R was zero for all ^{99m}Tc reconstructions.

Healthy liver segmentation

The usability of the ^{99m}Tc scans for the purpose of automatic segmentation of the healthy liver was investigated by analyzing the overlap between the segmentations and the pre-defined healthy liver compartment VOI for images acquired at different ^{99m}Tc activities. The segmentations were obtained using a thresholding procedure. The accuracy of a standard thresholding procedure relies on the choice of the threshold value, which is typically defined as a percentage of the maximum image intensity. This, however, implies that the segmentation relies on a single voxel value, the maximum, which is prone to inaccuracy due to noise. To reduce this dependency, the threshold value was instead based on a percentage (α) of the maximum value after having smoothened the image using a 3D Gaussian filter. The threshold was then applied back to the original, un-smoothened, image to produce the segmentation.

For every individual scan, an optimal threshold percentage α could be determined by applying an optimization routine which varied α to correctly recover the volume of the healthy liver in the phantom. However, as these values for α may be different between scans, a single value to apply to all scans was defined as the average of all individual optimal values.

The accuracy of the healthy liver segmentation using ^{99m}Tc images was evaluated by assessing both the recovered healthy liver compartment and the resulting cold spheres (i.e., the tumors). The ratio between the segmented volumes and the nominal volumes were computed for the three VOIs (cold sphere S1 and S2, and healthy liver compartment). In addition, the overlap between the segmentations and the nominal VOIs was assessed through the Sørensen-Dice index [39].

Statistical analysis

For the above mentioned metrics (uniformity, cold-sphere contrast recovery coefficients and healthy liver segmentation), a T-test was used to determine if there was a significant difference between the measurements acquired in presence or not of ^{166}Ho. P-values were reported only if a statistically significant difference was found.

Impact of k-factor on ^{166}Ho phantom reconstructions

SPECT reconstructions of ^{166}Ho images suffer from downscatter induced by higher energy gamma emissions and bremsstrahlung, detected in the 81 keV ^{166}Ho photopeak window. The 118 keV energy window, scaled with a k-factor, is used as an estimate for these downscatter contributions. In case of dual-isotope ^{166}Ho-^{99m}Tc imaging, there is an additional downscatter contribution arising from the ^{99m}Tc photopeak at 140 keV. Ideally, however, with a well-chosen k-factor, the ^{166}Ho reconstructions are independent of ^{99m}Tc activity.

The impact of ^{99m}Tc on ^{166}Ho images can be assessed by the COV and the contrast recovery coefficients (of hot spheres), similarly to the ^{99m}Tc analysis. However, both these metrics strongly depend on the ^{166}Ho count density in the healthy liver compartment.

To determine the optimal k-factor, the count density in the healthy liver compartment VOI was measured for all ^{166}Ho images, reconstructed for a range of k-factors (0.65 – 1.30 with a 0.05 step interval). For each k-factor, the relative change in ^{166}Ho count density was determined as a function of ^{99m}Tc activity.

Patient Data

To clinically evaluate the findings regarding the k-factor obtained using the phantom scans, a similar analysis was applied to images from patient procedures, for which both a ^{166}Ho-^{99m}Tc dual-isotope and a ^{166}Ho-only acquisition was available.

For all patient SPECT/CT acquisitions used in this study, informed consent was obtained as part of the HEPAR PLuS study [40]. Twenty-six scout (pre-treatment) procedures performed on patients with liver metastases of neuroendocrine tumors were analyzed (median administered activity (and interquartile range): 224 (35) MBq of ^{166}Ho).

According to the HEPAR PLuS study protocol, for each scout procedure, two SPECT/CT images were acquired: a ^{166}Ho-only SPECT/CT and, after administration of ^{99m}Tc-stannous phytate, a ^{166}Ho dual isotope SPECT/CT. All scans were acquired and reconstructed using the same protocols as those adopted for the ^{166}Ho-^{99m}Tc dual isotope phantom data. Similar to the ^{166}Ho phantom scans, ^{166}Ho patient images where reconstructed using multiple k-factors ranging from 0.65 to 1.30 with step 0.05.

To assess the impact of the k-factor on ^{166}Ho patient reconstructions, a volume of interest was defined containing the healthy liver (by thresholding the ^{99m}Tc image). Within this healthy liver VOI, the ^{166}Ho count density was determined for both acquisitions, ^{166}Ho-only and ^{166}Ho dual isotope, using the same k-factor for both reconstructions. The percentage

difference in ^{166}Ho count density between the ^{166}Ho dual isotope and ^{166}Ho-only acquisition was computed for each k-factor (ranging from 0.65 to 1.30).

Results

Phantom

Uniformity

The ^{99m}Tc image uniformity, measured as the coefficient of variation within the healthy liver compartment, is displayed in **Figure 3.2**. The COV decreased with the square root of ^{99m}Tc activity, but was independent on the presence of 250 MBq of ^{166}Ho in the phantom. No statistically significant difference was found between ^{99m}Tc images acquired in presence or not of ^{166}Ho.

3
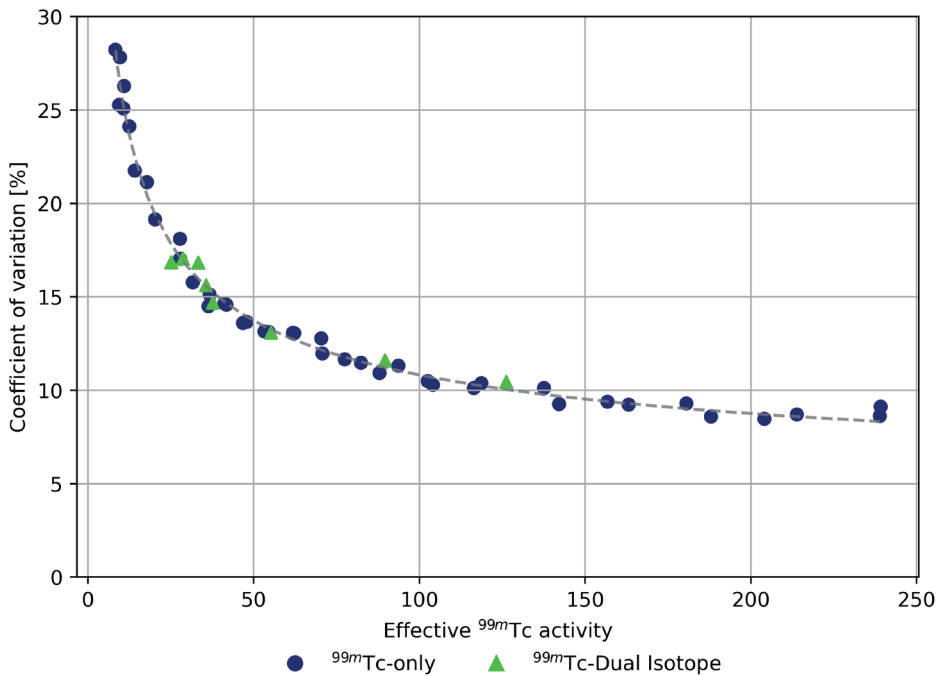
Figure 3.2
Coefficient of variation computed on the ^{99m}Tc images within the healthy liver compartment VOI. The coefficient of variation, measuring the level of inhomogeneity in the healthy liver compartment VOI, is displayed as function of effective ^{99m}Tc activity in the phantom. Blue circles refer to measurements acquired with ^{99m}Tc only while green triangles represent measurements acquired with ^{99m}Tc in presence of ^{166}Ho (dual-isotope). The COV decreases with the square root of ^{99m}Tc activity, down to an offset which is assumed to be present due to limited imaging resolution (independent of ^{99m}Tc activity). The gray dashed line depicts a fit to the data, where the offset was found to be 3.8%.

Contrast recovery of cold spheres

Cold-sphere contrast recovery coefficients as function of effective ^{99m}Tc activity in the phantom are reported in **Figure 3.3 A** and **B**, for sphere S1 and sphere S2, respectively. Mean ± standard deviation of Q_c was 65.7% ± 1.6% for sphere S1 and 57.8% ± 2.1% for sphere S2. At low ^{99m}Tc activities (< 50 MBq), a higher spread in Q_c (**Figure 3.3**) was visually noticeable. No statistically significant difference was found between ^{99m}Tc images acquired either in presence or not of ^{166}Ho.

Figure 3.3
Contrast recovery coefficient of cold spheres (Q_c) computed on ^{99m}Tc images acquired in presence of different ^{99m}Tc activities. Results are displayed as function of the total effective ^{99m}Tc activity in the phantom. Panel **A** refers to cold sphere S1 and panel **B** to cold sphere S2. Blue circles refer to measurements acquired in presence of ^{99m}Tc only while green triangles represent measurements acquired in presence of both ^{99m}Tc and ^{166}Ho.

Usability of ^{99m}Tc images for automatic healthy liver segmentation

The procedure to determine the optimal threshold percentage α was repeated for a range of Gaussian filter sizes, where a width (sigma) of 15 mm was found to produce the smallest

variance among segmented volumes. For this filter size, the averaged optimal threshold percentage α adopted for the automatic segmentation process was 40%.

Figure 3.4 shows the axial view of six phantom SPECT/CT scans with the healthy liver contour overlapped resulting from the automatic segmentation process.
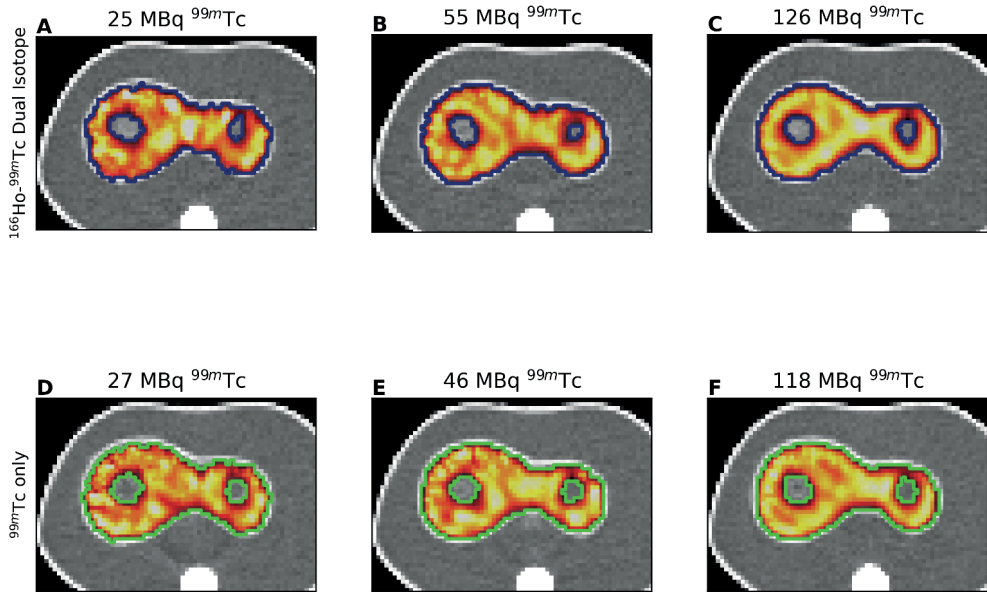
Figure 3.4

Axial view of ^{99m}Tc reconstructions and healthy liver segmentations. Healthy liver segmentations of ^{99m}Tc SPECT/CTs, acquired in presence of 250 MBq^{166}Ho (top panel) and without ^{166}Ho (bottom panel). Three ^{99m}Tc activity levels are presented to indicate the effect on image quality and segmentation accuracy.

Results for the volume recovery percentage and Sørensen-Dice index as function of the effective ^{99m}Tc activity are depicted in **Figure 3.5**. Panel **A** and **D** refer to cold sphere S1, **B** and **E** to cold sphere S2 and panel **C** and **F** to the healthy liver compartment. Mean ± standard deviation for the volume recovery percentage were 88.8% ± 5.3%, 118.2% ± 12.0% and 99.6% ± 3.8% for cold sphere S1, S2 and healthy liver compartment, respectively. Mean ± standard deviation for the Sørensen-Dice index were 0.79 ± 0.02, 0.58 ± 0.03 and 0.93 ± 0.01 for cold sphere S1, S2 and healthy liver compartment, respectively. No statistically significant difference was found between ^{99m}Tc images acquired either in presence or not of ^{166}Ho.
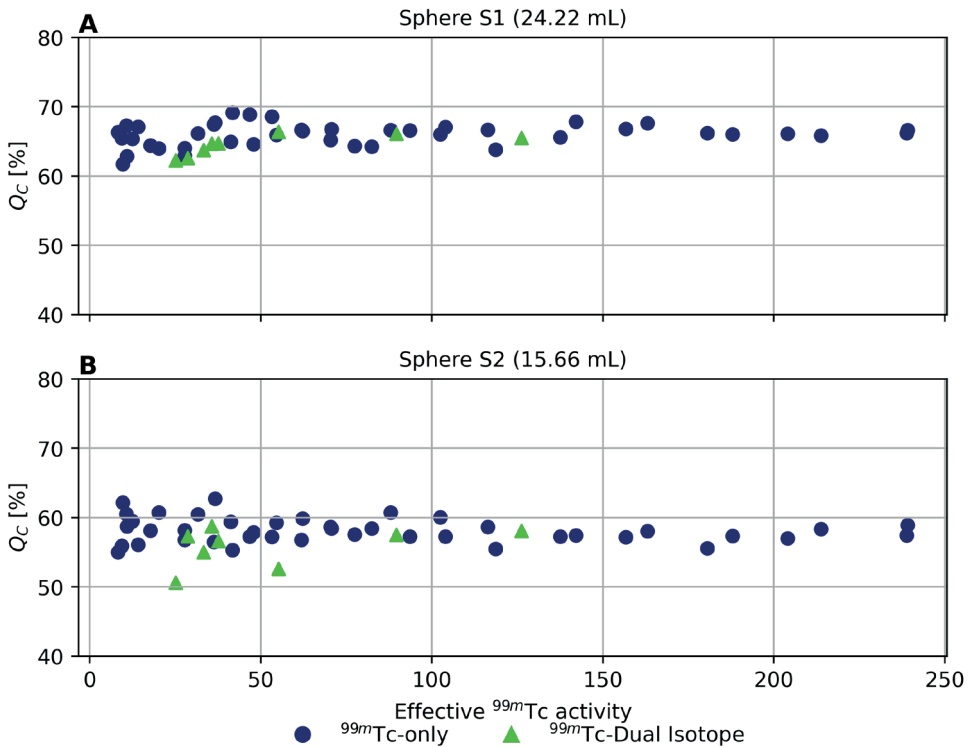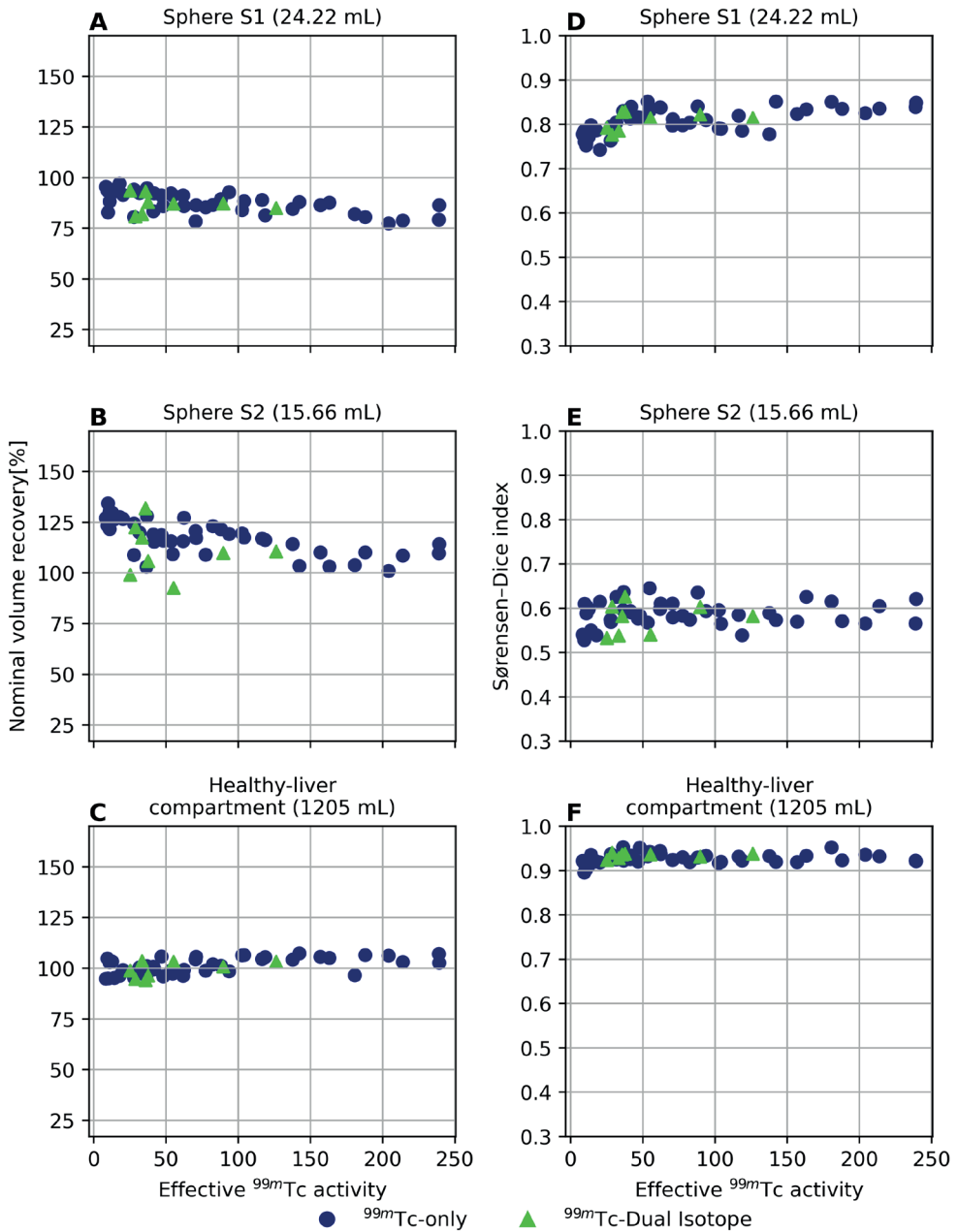
Figure 3.5

Nominal volume recovery and Sørensen-Dice index obtained from segmentation of the ^{99m}Tc images using a threshold approach. On the left, the percentage of recovered nominal volume using the threshold

Figure 3.5 Continued

approach for the three VOIs under investigation is shown: sphere S1 (panel **A**), sphere S2 (panel **B**) and healthy liver compartment (panel **C**). Blue circles refer to measurements acquired in presence of ^{99m}Tc only while green triangles represent measurements acquired in presence of both ^{99m}Tc and ^{166}Ho. The results are displayed as function of the total effective ^{99m}Tc activity in the phantom. On the right (panel **D**, **E** and **F**) the corresponding Sørensen-Dice index is shown.

Impact of k-factor on ^{166}Ho phantom reconstructions

The coefficient of variation and the contrast recovery coefficients for the hot spheres, as function of the effective ^{99m}Tc activity in the phantom, are depicted in **Figure 3.6** for several k-factors.

A poor choice for the k-factor will under- or over correct ^{99m}Tc scatter in the ^{166}Ho image, causing an increase or decrease of apparent ^{166}Ho signal in the phantom, approximately linear with ^{99m}Tc activity. This dependency is illustrated in **Figure 3.6** where results are shown for the lowest and the highest k-factor. However, tuning the k-factor can reduce the impact of ^{99m}Tc, as shown by the dashed lines in **Figure 3.6**.

The percentage error in ^{166}Ho count density, as a result of adding ^{99m}Tc (evaluated at 50 MBq for consistency with the current clinical protocol), is plotted as a function of k-factor in **Figure 3.7** (blue crosses) along with the results from patient scans. It ranged from 14.3% to -18.6%. The k-factor for which the ^{166}Ho count density in the phantom was least dependent of ^{99m}Tc activity was 0.95.

Patient data

Impact of k-factor on ^{166}Ho patient reconstructions

For the patient scans, the count density in ^{166}Ho reconstructions was measured in the healthy liver volume, for both ^{166}Ho-only scans and ^{166}Ho dual isotope scans. The percentage difference between these measurements, attributed to downscatter from the additional ^{99m}Tc in the liver, is plotted in **Figure 3.7** as a function of k-factor. For every k-factor, the data of the 26 patient procedures are summarized in a boxplot. A k-factor of 1.05 resulted in the smallest overall impact of ^{99m}Tc on ^{166}Ho image reconstructions with a median percentage difference (and interquartile range) of 1.7% (6.4%), ranging from -12.9% to 13.3%.
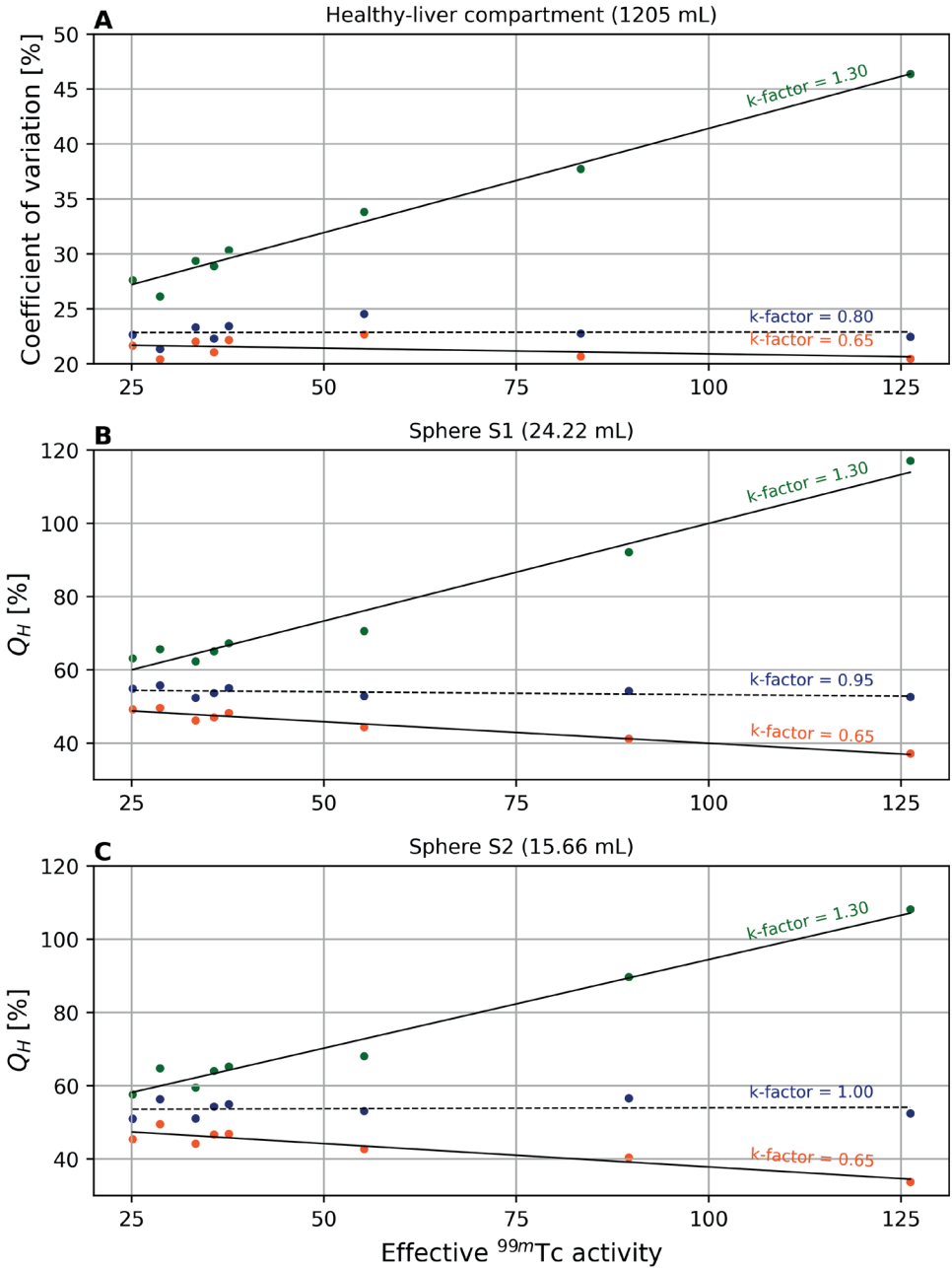
Figure 3.6

Quality analysis for the [166]Ho images, reconstructed using several k-factors, as function of the ^{99m}Tc activity in the phantom during the [166]Ho-^{99m}Tc dual-isotope acquisition. Coefficient of variation and

Figure 3.6 (Continued)

contrast recovery coefficients for hot sphere S1 and S2 are depicted as function of effective 99mTc activity in the phantom, for 166Ho reconstructions using three different k-factors. Panel **A** shows the coefficient of variation, measuring the level of inhomogeneity, computed on the 166Ho images within the healthy liver compartment VOI. Panel **B** and **C** depict the contrast recovery coefficients for sphere S1 and S2, respectively. Ideally, these image-quality metrics for 166Ho are independent of 99mTc activity if scatter from 99mTc is sufficiently corrected for. The impact of the choice of k-factor can be observed by the dependence on 99mTc activity, causing an offset of counts in the phantom background. The depicted k-factors are the lowest, the highest and the k-factor leading to the lowest dependency on 99mTc for the considered metric.
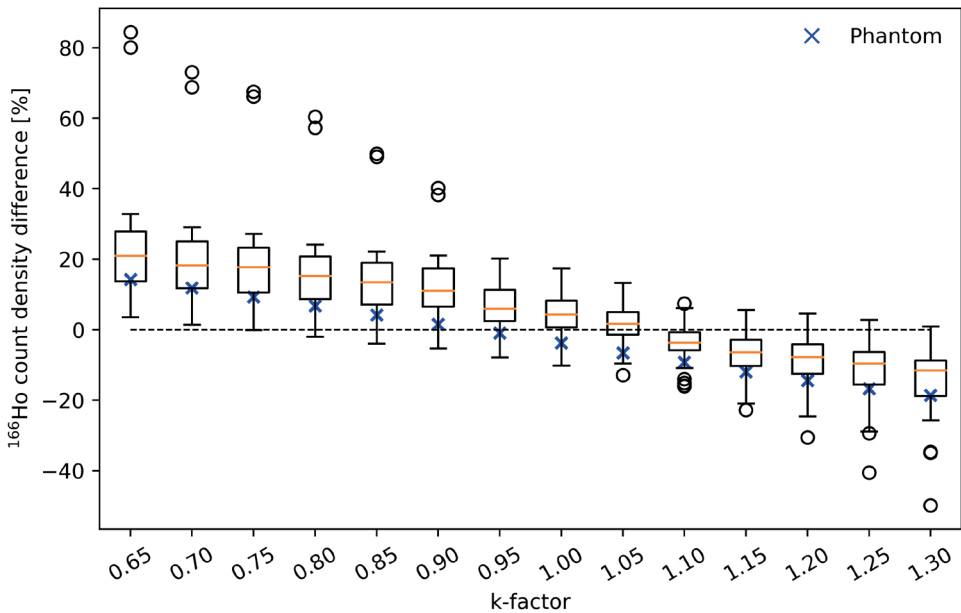
Figure 3.7

Dependence of 99mTc scatter correction on 166Ho reconstructions. Scatter contributions from 99mTc on 166Ho image reconstructions are corrected for using a dual-energy-window scatter correction. The scatter is estimated from the 118 keV energy window, positioned in between the 166Ho and 99mTc photopeak, scaled by a k-factor. This graph shows the measured count density difference in 166Ho reconstructions from 166Ho-99mTc dual isotope acquisitions relative to 166Ho-only acquisitions, as function of the k-factor. Each boxplot represents the results for the 26 patient procedures. Count density was evaluated within the healthy liver volume. Outlier values were due to a higher-than-average 166Ho concentration in the liver (due to either higher activity or relatively small liver volume). The blue crosses show the equivalent metric for the phantom study, where the count density difference was evaluated for a 99mTc activity of 50 MBq.

Discussions

Accurate image segmentation and registration are paramount to provide personalized dosimetry to radioembolization patients. However, these tasks are time-consuming and user-dependent, being currently performed manually.

The registration step could be avoided by adding a contrast enhanced CT acquisition to the SPECT/CT procedure. However, some limitations prevent this approach to be used in clinical practice. Typically, a contrast enhanced CT is already acquired prior to the scout procedure. Additionally, many SPECT/CT systems lack a contrast injector. Moreover, unless an algorithm for liver and tumor delineation on CT is clinically available, this approach would still require the manual segmentation of the volumes of interest.

The ^{166}Ho-^{99m}Tc dual isotope protocol is a viable option to provide an automatic segmentation of the healthy liver within the ^{166}Ho radioembolization context. This study demonstrates that the reciprocal interaction between the two isotopes can mostly be negated, provided a proper k-factor for downscatter correction is applied for ^{166}Ho reconstructions and a triple-energy-window scatter correction is applied for ^{99m}Tc reconstructions.

^{99m}Tc reconstructions

From the measurements performed using an anthropomorphic phantom it was shown that ^{99m}Tc image uniformity improved only little for higher ^{99m}Tc activities (>100 MBq), but that it was independent of ^{166}Ho activity in the phantom. On average, the contrast recovery coefficients of the cold spheres were not dependent on ^{99m}Tc activity, regardless of the presence of ^{166}Ho. Nonetheless at lower ^{99m}Tc activities (<50MBq) a higher spread for Q_c was found (**Figure 3.2**). The partial contrast recovery can be attributed to spill-in from activity in the healthy liver compartment due to the limited SPECT system resolution.

Within the investigated range, the amount of ^{99m}Tc activity did not have a significant effect on the accuracy of the healthy liver segmentations. Using the same method for each segmentation, irrespective of ^{99m}Tc activity or in presence or not of ^{166}Ho, the healthy liver compartment was recovered to 100% of its nominal volume, with a Sørensen-Dice index > 0.9. However, the cold spheres within the liver (representing tumors), were segmented to a lower accuracy as was evident from the reduced Sørensen-Dice indices.

^{166}Ho reconstructions

For phantom images acquired at an effective ^{166}Ho activity of 250 MBq in presence of ^{99m}Tc, a major role was played by the choice of k-factor used for scatter correction, particularly for

increasing ^{99m}Tc activities. When reconstructed with adequate k-factors, the coefficient of variation, contrast recovery coefficients for the hot spheres, and count density in the ^{166}Ho main photopeak was, on average, not dependent on effective ^{99m}Tc activity in the phantom. However, there is no single k-factor which is optimal to fully compensate for scatter across the whole ^{166}Ho image. This emphasizes how the application of window-based scatter correction is only an approximation to correct a complex, non-linear, phenomenon.

Patient scans showed the same k-factor dependence as demonstrated in the phantom study. Earlier work resulted in a k-factor of 1.15, which was based on simulations for ^{166}Ho (by ignoring the 81 keV emission line) and by comparing counts in the projection windows for ^{99m}Tc. In the current work, however, the effect of the k-factor used to correct for ^{99m}Tc downscatter was measured directly on the resulting ^{166}Ho reconstructions by considering the count density in the healthy liver compartment (similar to patient dosimetry) depending on the presence of ^{99m}Tc. A combined analysis of all patient and phantom scans (shown in **Figure 3.7**) indicated that a k-factor of 1.05 resulted in the lowest impact of ^{99m}Tc on ^{166}Ho reconstructions overall.

The direct effect of inadequate scatter correction on ^{166}Ho image reconstruction is an over- or under estimation of the count density, primarily in the healthy liver compartment (due to the presence of ^{99m}Tc stannous phytate). In clinical practice, dosimetry is often performed by first scaling the ^{166}Ho scout image such that the total of counts in the image (including tumor uptake and extrahepatic depositions) corresponds to the planned therapeutic activity. Therefore, due to this scaling procedure, the impact of scatter on healthy liver dosimetry is dependent on the relative activity distribution amongst the compartments. The measured percentage in ^{166}Ho count-density difference in the healthy liver serves as an upper bound to the error in healthy liver dosimetry. I.e.: when all ^{166}Ho activity resides within the healthy liver compartment, the count-density offset due to poor scatter correction is negated as a result of the scaling process.

Limitations and future developments

The presented value for the optimal k-factor is specific for the energy windows used in this work and includes the weight factor to account for the difference in window widths between the 81 keV and 118 keV windows. When different energy window settings are applied, care has to be taken to properly adapt, or re-evaluate, the required k-factor.

Whereas the phantom was filled with uniform activity, a more heterogeneous ^{99m}Tc activity distribution will be encountered in patients. This may cause a relatively low ^{99m}Tc activity in the healthy tissue to be classified as non-healthy tissue. Thus, the possibility to automatically segment the heathy liver based on a threshold approach using ^{99m}Tc images needs to be

validated in clinical practice by comparing against manual segmentations of contrast enhanced CT images. In particular, the impact of adopting this method rather than the current manual approach for segmentation and registration has to be investigated with respect to dosimetry, time required to perform these tasks and inter-observer influence.

Conclusion

Within the context of the ^{166}Ho-^{99m}Tc dual isotope protocol, the impact of ^{99m}Tc on reconstructed ^{166}Ho count density in the healthy liver could mostly be negated, provided an adequate k-factor for downscatter correction was applied during image reconstruction. The healthy liver compartment of the phantom could accurately be segmented on the ^{99m}Tc images using a thresholding method, irrespective of the amount of ^{99m}Tc activity or in presence or not of ^{166}Ho, and the healthy liver compartment was recovered to 100% of its nominal volume (Sørensen-Dice index >0.9).

Because additional scatter due to the presence of ^{99m}Tc can effectively be corrected, the dual isotope protocol can safely be applied without compromising ^{166}Ho image quality. However, validation of the automatic segmentation method, and its effect on dosimetry, needs to be assessed in clinical practice.
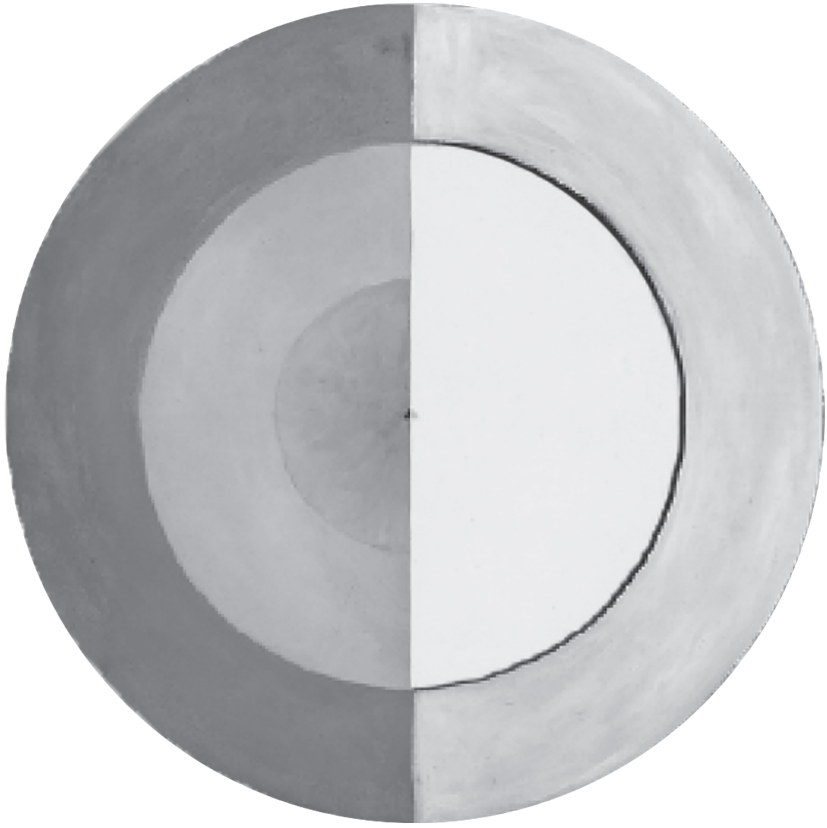
CHAPTER 4

Acquisition and reconstruction parameters for ^{166}Holmium SPECT imaging

Abstract

Background: To achieve individualized treatment for Holmium-166 (^{166}Ho) radioembolization, dose assessment is a crucial step for which reliable ^{166}Ho images are essential. The objective of this study is to quantitatively assess image quality of ^{166}Ho clinical reconstructions performed without any scatter correction (noSC; baseline) compared to dual-energy-window (DEW; current clinical standard) and triple-energy-window (TEW) scatter correction method.

Methods: To this purpose, a cylindrical phantom and a NEMA Image Quality phantom with an activity concentration ratio between spheres and background of 8:1 were filled with 600 MBq of ^{166}Ho chloride. The images were acquired at three different activity levels to assess the impact of activity and detector dead time on the image quality. For each activity level, NEMA scans were performed three times. Each scan was reconstructed using noSC, DEW and TEW based scatter correction methods. Resulting ^{166}Ho reconstructions were evaluated on homogeneity and noise, for the cylindrical phantom, and by contrast recovery coefficients (CRCs) and contrast to noise ratios (CNRs), for the NEMA phantom. Furthermore, post filtering and energy-window widths were varied for further optimization.

Results: By applying DEW and TEW, both axial and radial homogeneity increased, to the detriment of noise (+33% and +44% relative to noSC, at medium activity level, for the DEW and TEW, respectively). Similarly, CRCs improved when scatter correction was applied, with TEW based scatter correction exceeding DEW (+77% and +42%, for the largest sphere insert, for the TEW and DEW, respectively). CNRs were comparable between DEW and TEW, both outperforming noSC reconstructions (+15% for the largest sphere insert). The application of image smoothening and enlarged energy window width, to reduce noise, showed the possibility to improve scatter correction, by using TEW method, achieving higher CRCs, without decreasing the CNRs.

Conclusion: TEW based scatter correction method was demonstrated to improve downscatter correction for ^{166}Ho SPECT image reconstruction. The increased image quality is beneficial for ^{166}Ho dosimetry. TEW based scatter correction is easier to implement within the clinical reconstruction software compared to the current DEW reconstruction protocol and would facilitate ^{166}Ho SPECT imaging harmonization.

Background

Dosimetry is increasingly regarded as an essential step in radioembolization, either using yttrium-90 (^{90}Y) or holmium-166 ([166]Ho) microspheres. In case of [166]Ho, accurate dosimetry relies on quantitative SPECT images. However, SPECT imaging suffers from limited resolution, and the image quality is dependent on many factors, such as the emission properties of the isotope used, the collimator, the recorded energy windows, and the reconstruction parameters. Therefore, the accuracy of dosimetry, and of tumor dosimetry in particular, is susceptible to the choice of these parameters. In addition, if dosimetric cut-off values are to be applied globally, and when comparing results between different imaging centers, it is important to have similar image quality and thus the harmonization of these parameters is especially compelling. Even if much effort has been deployed in recent years to propose procedures to harmonize SPECT/CT image quality [41], [42], imaging protocols for [166]Ho are still not standardized.

[166]Ho has a complex emission spectrum, shown in **Figure 4.1** panel **A**, with a relatively low energy photopeak used for imaging (6.7% abundance of 80.6 keV photons). It presents also high energy gamma emissions (1.38 MeV/0.93%, 1.58 MeV/0.19%, 1.66 MeV/0.12%) and bremsstrahlung photons, interacting within the patient and collimator-detector system. Thus, the [166]Ho main photopeak energy window is influenced by the combination of primary photopeak photons, photopeak-scatter and attenuation, downscatter of high energy emissions and lead x-rays that originate from the collimator at around 75 keV. Photopeak-scatter derives from all primary photopeak and higher energy photons that end up in the photopeak window after having had Compton interactions; "downscatter" is instead represented by all photons that end up in the energy window originating from either higher energy photon interactions or bremsstrahlung. When imaging [166]Ho with SPECT, these interactions should be estimated and accounted for.

As a straightforward scatter correction by means of a scatter window placed below the photopeak was considered not possible due to lead x-rays energy close to the primary photopeak window, dedicated methods were developed for these estimations. These included a Monte Carlo simulations of the photopeak physics combined with window-based estimations for higher-energy contributions [23], and a full Monte Carlo simulator including all physics [32].

Clinical practice is however limited to the scanner options and therefore current clinically used [166]Ho SPECT imaging protocol only corrects the downscatter, using a dual-energy window-based approach (DEW) with a window centered at 118 keV [23].

A

B
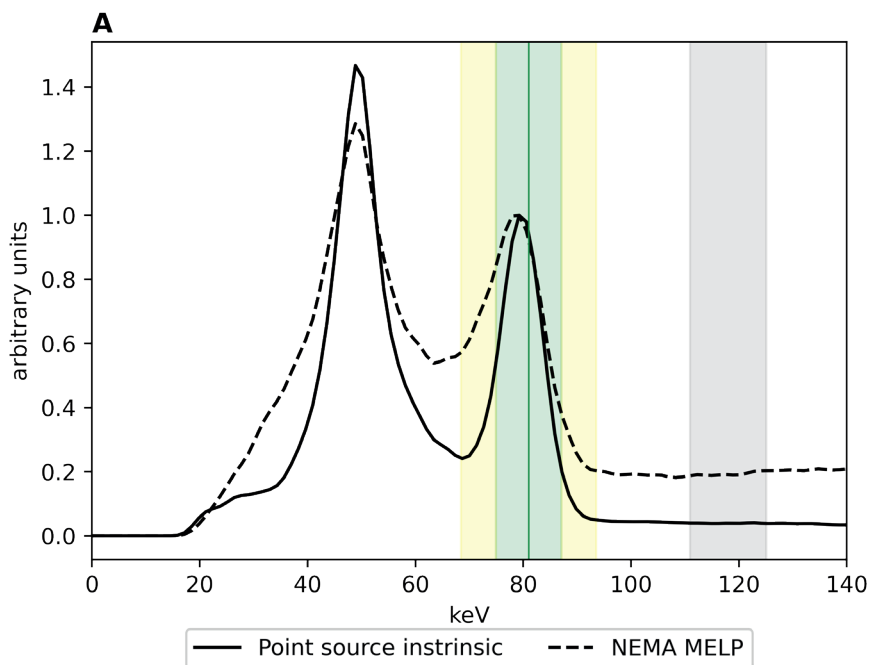
	Center [keV]	Width [%]	Width [keV]	Start [keV]	End [keV]
Photopeak	81.00	15	12.15	74.92	87.08
Lower scatter	71.69	8 (of pp*)	6.48	68.44	74.93
Upper scatter	90.32	8 (of pp*)	6.48	87.08	93.56
General scatter	118.00	12	14.16	110.92	125.08

Figure 4.1

Spectrum and acquisition parameters for the scans performed with a main photopeak window width of 15%. Panel **A** shows the intrinsic ^{166}Ho spectrum for a point source (solid black line) and the extrinsic (MELP collimators) ^{166}Ho spectrum acquired for the NEMA phantom (dashed black line). Spectra were scaled to match the main photopeak for visual purposes. Main photopeak window is colored in green. Lower and upper scatter windows used for the TEW_{15} reconstruction are colored in yellow. Gray area represents the scatter used for the DEW_{15} reconstruction. Panel **B** reports the window settings for the acquisition protocol adopted. *pp = photopeak.

Given the increased use of [166]Ho as radioembolization device, [166]Ho SPECT imaging would benefit from an imaging protocol including photopeak scatter correction and that is easy to implement clinically. A triple-energy window (TEW) approach would suit this purpose, similar to protocols typically employed for isotopes such as Iodine-131 [43], Iodine-123 [44], Indium-111 [45], and Lutetium-177 [46]. Moreover, a standard TEW scatter correction method is easier to implement compared to the DEW based approach currently used in clinical practice. In the case of [166]Ho, the conventional DEW scatter correction method needs to be adjusted to take into account the high energy emissions of the [166]Ho spectrum. Firstly, the scatter window is located above the main photopeak (whereas it is typically below); secondly, the scatter window is not directly connected to the main photopeak, but at some distance, to ensure a non-contaminated downscatter estimate; and thirdly, it requires a specific scatter correction factor (k-factor). All these non-standard settings call for greater attention when implementing the DEW scatter correction workflow for [166]Ho, making it prone to error, while a TEW method is straightforward to implement in the commercial reconstruction, facilitating its adoption.

The scope of this study is to quantitatively assess image quality of [166]Ho reconstructions performed without any scatter correction (baseline) compared to DEW (clinical standard) and TEW scatter correction method. Furthermore, post filtering and energy-window widths (for TEW based method) were varied for further optimization.

Materials and Methods

A standard 20 cm diameter, 20 cm long fillable cylindrical phantom with no insert was used to assess image uniformity and noise. A NEMA Image Quality (IQ) body phantom (**Figure 4.2** panel **A**) containing six fillable spheres (inner diameters of 10, 13, 17, 22, 28 and 37 mm) and a 51 mm diameter lung insert filled with polystyrene beads and water was used to assess contrast recovery coefficients (CRCs) and contrast-to-noise ratios (CNRs).

Both phantoms were filled with ~600 MBq of [166]Ho chloride (HolmiumSolution, Quirem Medical B.V., The Netherlands) dissolved in 0.1 M hydrogen chloride to ensure homogeneous solutions and prevent sticking (or plating) of activity to the phantom walls. The cylindrical phantom (6266 mL) was homogenously filled, while the NEMA phantom was filled with an 8:1 sphere-to-background activity concentration ratio.

4
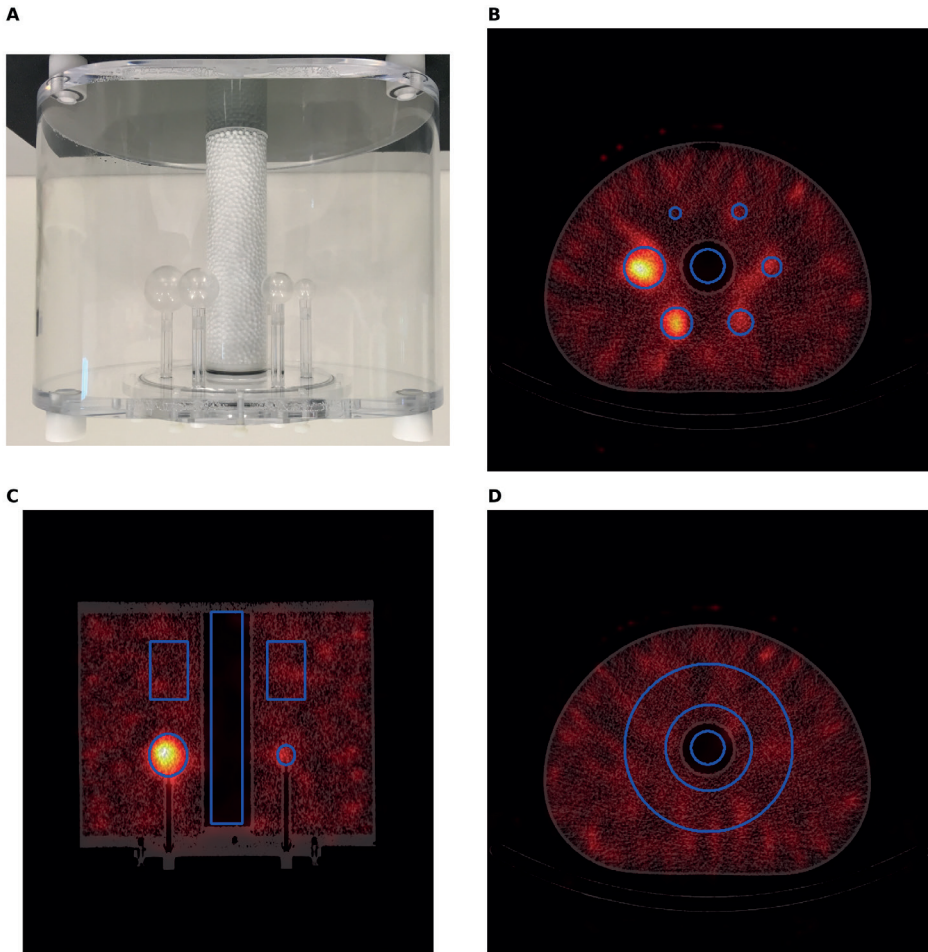
Figure 4.2
The NEMA IQ phantom used for the experiment is shown in a picture in panel **A**. Panel **B**, **C**, and **D** show the CT with the corresponding SPECT acquired at ~ 300 MBq (TEW$_{15}$ reconstruction) for the axial, coronal and sagittal view, respectively. VOIs used to assess the contrast recovery coefficients and contrast-to-noise ratios are depicted in blue.

To determine the influence of different scatter correction methods on ^{166}Ho reconstructions, a dedicated acquisition protocol mimicking the current clinical protocol with additional scatter windows was defined. All windows specified in **Figure 4.1** were recorded. Alongside this protocol, with a main photopeak window width of 15%, additional acquisitions with a main photopeak window width of 20% were tested to assess the impact of the window width on the TEW scatter correction method (**Figure 4.3**).

A

B
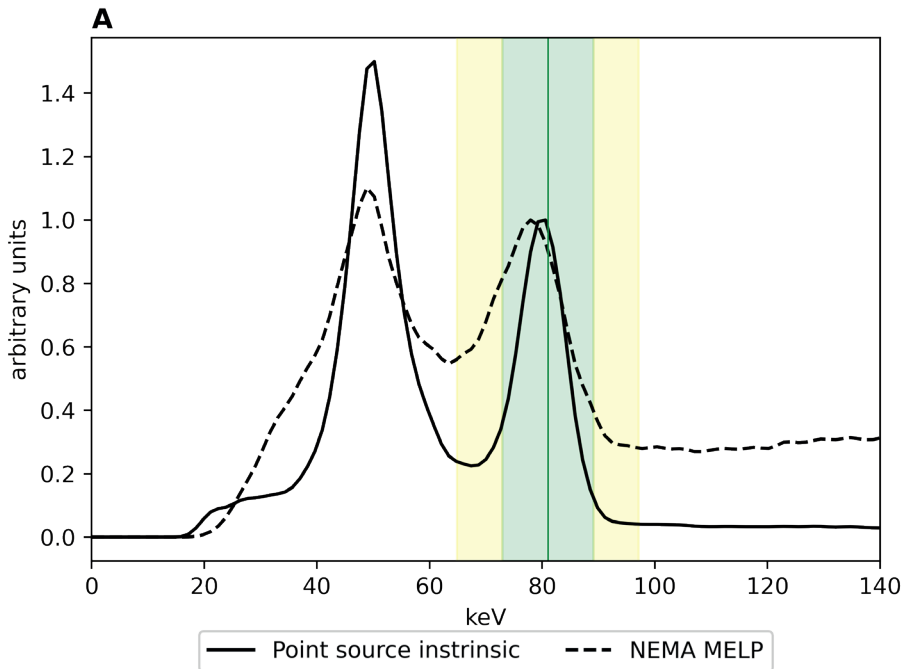
	Center [keV]	Width [%]	Width [keV]	Start [keV]	End [keV]
Photopeak	81.00	20	16.20	72.90	89.10
Lower scatter	68.85	10 (of pp*)	8.10	64.80	72.90
Upper scatter	93.15	10 (of pp*)	8.10	89.10	97.20

Figure 4.3

Spectrum and acquisition parameters for the scans performed with a main photopeak window width of 20%. Panel **A** shows the intrinsic ^{166}Ho spectrum for a point source (solid black line) and the extrinsic (MELP collimators) ^{166}Ho spectrum acquired for the NEMA phantom (dashed black line). Spectra were scaled to match the main photopeak for visual purposes. Main photopeak window is colored in green. Lower and upper scatter windows used for the TEW$_{20}$ reconstruction are colored in yellow. Panel **B** reports the window settings for the acquisition protocol with enlarged energy window width. *pp = photopeak.

All images were obtained using a Symbia T16 SPECT/CT scanner (Siemens, Erlangen, Germany), currently used in our institution for clinical studies. Scanner specifications and imaging parameters are reported in **Table 4.1**. All images were reconstructed using Flash3D (Siemens), with 10 iterations, 8 subsets and without any post-reconstruction filtering and

attenuation correction. For each scan with a main photopeak window width of 15%, three reconstructions were performed: without any scatter correction (noSC) used as baseline, with a DEW based scatter correction identical to the current clinical imaging protocol with a k-factor of 1.05 and with a TEW based scatter correction (automatic scatter window weights of 0.94, correcting for window width differences). The scan acquired with a main photopeak window width of 20% were reconstructed using a TEW based scatter correction. The resulting reconstructions were named after the scatter correction method applied and the main photopeak window width (namely $noSC_{15}$, DEW_{15}, and TEW_{15} and TEW_{20}).

Manufacturer	Siemens
Model	Symbia T16
Detector crystal	3/8" NaI
Year of installation	2011
Software version	VB10E
Collimator	Medium Energy Low Penetration (MELP)
Number of projections	120 (60 view per head)
Matrix size	128 x 128
Time per projections	20 sec/views
Orbit	Non-circular
Mode	Step-and-shoot

Table 4.1
Characteristics of the used SPECT/CT system

The images were acquired at three different activity levels (high: ~600 MBq, medium: ~350 MBq and low: ~200 MBq) to assess the impact of activity and detector dead time on the image quality. Prior to every measurement, the energy spectrum as recorded by the gamma camera was stored. For each activity level, NEMA scans were performed three times. A total of 3 and 9 scans at low, medium and high [166]Ho activity level were obtained for the cylindrical and the NEMA phantom, respectively (**Figure 4.4** panel **B**).

Prior to any SPECT acquisition, the scanner was peaked using a 6 MBq [166]Ho source in a syringe (1 mL) placed at ~ 1 m from detector heads (without collimators) turned to face the syringe.

To compare the three [166]Ho image reconstructions ($noSC_{15}$, DEW_{15}, and TEW_{15}) multiple metrics were assessed: homogeneity and noise (cylindrical phantom), and contrast recovery coefficients (CRCs) and contrast-to-noise ratios (CNRs) (NEMA IQ phantom), respectively. ANOVA test was used to determine if there was a significant difference between the measurements acquired at different activity levels. P-values were reported only if a statistically significant difference was found.

The count density profile along the axial (**Figure 4.5** panel **A**) and radial (**Figure 4.5** panel **B**) directions of the cylindrical phantom provided a measure for the homogeneity. Ideally the axial and radial profiles resemble step functions, proportional to the activity concentration in the phantom. A non-flat profile may indicate inadequate scatter correction.

The coefficient of variation (COV), defined as the ratio of the standard deviation to the mean, computed within 70% of the cylindrical phantom volume, along the axial direction, (**Figure 4.5** panel **A**) was used as a metric to quantify noise in the reconstructions.

For the NEMA phantom assessment, contrast recovery coefficients were computed. The CRCs for the hot spheres and the lung insert were calculated as follows:

$$CRC = \frac{\frac{C}{C_B} - 1}{R - 1}$$

where C is either C_H, the the average number of counts in the hot sphere volume VOI, or C_L, the average number of counts in the lungs, while C_B is the average number of counts in the background VOI. R is the ratio between activity concentration in the VOI and in the background, equal to either 8 or 0 for spheres and lungs, respectively. The six spherical regions of interest (VOIs) (10, 13, 17, 22, 28, 37 mm diameter) were centered on the hot spheres, while a cylindrical VOI (30 mm diameter) was centered on the lung insert (**Figure 4.2** panel **B**). The background VOI was defined within the uniformly filled background compartment of the NEMA phantom, distant from the spheres, and to resemble their radial positions, to obtain equivalent scatter and attenuation. This resulted in a background VOI with the shape of a toroid with a rectangular cross-section (radius of revolution = 5.7 cm, height = 5 cm and width = 3.7cm), as depicted in **Figure 4.2**, panel **C** and **D**.

Contrast-to-noise ratio was defined as:

$$CNR = \left| \frac{C - C_B}{\sigma_B} \right|$$

Where C and C_B are defined as above, while σ_B is the standard deviation in the background VOI.

Finally, the impact of post-filtering and energy window width (for TEW based scatter correction) on CRCs and CNRs was tested using the DEW$_{15}$ (current clinical practice) as reference. DEW$_{15}$, TEW$_{15}$ and TEW$_{20}$ reconstructions were smoothened with a Gaussian filter (FWHM of 10 mm) and compared to the corresponding non-filtered images. This analysis focused on the three acquisitions performed at the medium activity level, averaged for statistical purpose.

Results

The activity at the scanning time, together with the number of measurements and the scanner dead time are reported in **Figure 4.4**, panel **B**. **Figure 4.4** panel **A** depicts the measured counts rate in the main photopeak window (15% window width) on the Symbia scanner. For measurements acquired at the high activity level (~600 MBq), dead time was greater than 10%. The intrinsic energy peaking procedure resulted in a 2% shift of the energy windows.

A — Counts per second vs. ^{166}Holmium activity at the scanning time [MBq]

Legend: ◆ Cylinder   ● NEMA

B

	Activity Level	N	Activity [MBq]	Dead Time [%]
Cylinder	High	1	590	13
Cylinder	Medium	1	332	7
Cylinder	Low	1	211	5
NEMA	High	3	550, 565, 580	12.3, 12.6, 12.9
NEMA	Medium	3	328, 346, 356	7.5, 7.9, 8.1
NEMA	Low	3	198, 203, 208	4.6, 4.7, 4.8
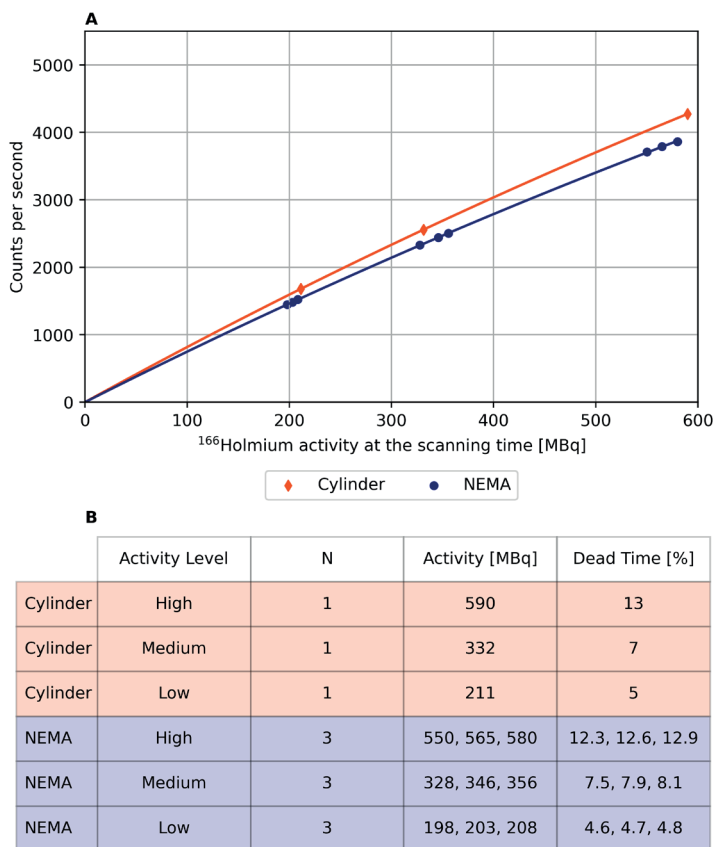
Figure 4.4

Panel **A** shows the count rate measured in the main ^{166}Ho photopeak (15% window width) for cylinder (orange diamond) and NEMA (blue dot) phantom. Paralyzable detector dead time model is depicted by the solid lines. Panel **B** shows an overview of the acquired measurements.

For the sake of visual clarity, only metrics measured at medium activity level were reported. When statistically significant differences among activity levels were found for a specific metric, metric values were reported, together with the resulting p-value for the ANOVA test.

Noise and homogeneity assessed in the cylindrical phantom are depicted in **Figure 4.5**.
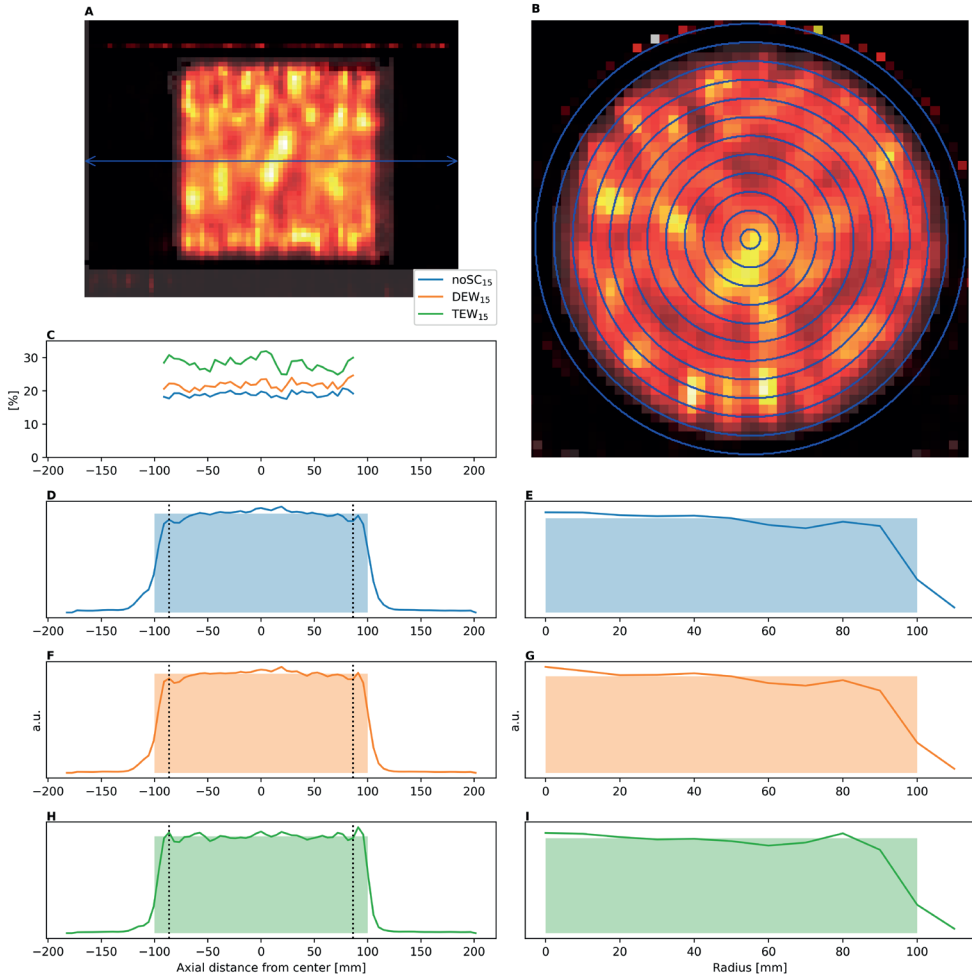
Figure 4.5

Panel **A** shows a sagittal view of the cylindrical phantom for the TEW_{15} reconstruction acquired at ~ 300 MBq. The blue arrow depicts the direction along which noise and axial homogeneity are computed. Panel **B** shows the central axial view of the cylindrical phantom for the TEW_{15} reconstruction acquired at ~ 300 MBq. Annuli used for the radial homogeneity are superimposed in blue. Panel **C** shows the noise within the phantom along the axial direction. Panel **D, F, H** and **E, G, I** show the homogeneity in the axial and radial direction, respectively, for the three different reconstruction methods ($noSC_{15}$, DEW_{15} and TEW_{15}). Colored rectangular areas represent the ideal profiles. $noSC_{15}$ = no scatter correction, DEW_{15} = dual-energy window, TEW_{15} = triple-energy window, for the 15%-wide photopeak window.

Noise increases with the increasing scatter correction applied (**Figure 4.5** panel **C**) with an average COV value of 16.5%, 22.0% and 23.8% for $noSC_{15}$, DEW_{15}, and TEW_{15}, respectively. Noise is dependent on the total activity with COV decreasing with increasing activity. Mean COV for the three activity levels and different reconstruction methods is reported in **Table 4.2**.

	Low	Medium	High
$noSC_{15}$	19.01	16.46	15.50
DEW_{15}	25.86	22.04	19.22
TEW_{15}	28.24	23.75	20.49

Table 4.2
Mean coefficient of variation (measuring the noise), expressed as percentage, in the cylindrical phantom for the three reconstruction methods ($noSC_{15}$, DEW_{15}, TEW_{15}) for different activity levels. $noSC_{15}$ = no scatter correction, DEW_{15} = dual-energy window, TEW_{15} = triple-energy window, for the 15%-wide photopeak window.

From a visual assessment of both axial and radial homogeneity (**Figure 4.5** panel **D** and **E**), TEW_{15} reconstruction showed the flattest line profile. This result was confirmed by the lower root mean square error values (computed between the ideal and the measured line profile) for the TEW_{15} compared to DEW_{15} and $noSC_{15}$ reconstructions. Root mean square error values are reported in **Table 4.3**. Activity levels had no influence on the homogeneity.

	Axial	Radial
$noSC_{15}$	$2.51e^{-3}$	$1.52e^{-1}$
DEW_{15}	$2.26e^{-3}$	$1.56e^{-1}$
TEW_{15}	$2.09e^{-3}$	$1.38e^{-1}$

Table 4.3
Root-mean-squared error (RMSE) computed between the measured and the ideal line profile, a rectangular and a step function for the axial and the radial homogeneity, respectively. RMSE are reported for the medium activity level. $noSC_{15}$ = no scatter correction, DEW_{15} = dual-energy window, TEW_{15} = triple-energy window, for the 15%-wide photopeak window.

Figure 4.6 depicts the contrast recovery coefficients (panel **A**) and the contrast-to-noise ratios (panel **B**) assessed for the hot sphere VOIs and the lung insert.

For each activity level considered, the three measurements acquired were averaged. CRCs increased with increasing scatter correction, particularly for the two biggest spheres, as reported in **Table 4.4**.
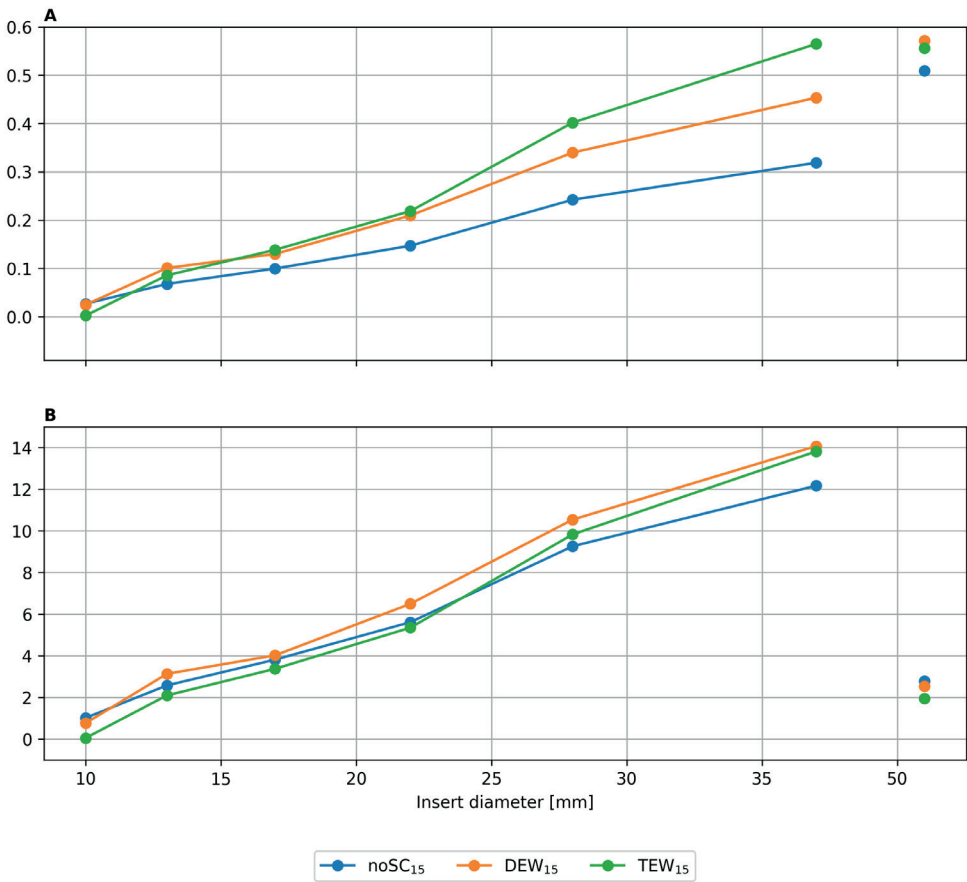
Figure 4.6

Panel **A** and **B** show the contrast recovery coefficients and contrast-to-noise ratios for the hot sphere VOIs and the lung insert (unconnected data point), respectively. $noSC_{15}$ = no scatter correction, DEW_{15} = dual-energy window, TEW_{15} = triple-energy window, for the 15%-wide photopeak window.

Different activity levels showed no statistically significant difference with respect to the CRCs. When considering the biggest hot sphere VOI, DEW_{15} and TEW_{15} reconstructions showed similar CNR values (min-max) of 14.1 (11.4-14.8) and 13.8 (11.5-14.5), respectively. Since the relative noise level (COV) also increases with decreasing activity, the CNR values are generally higher at the highest activity level considered (~600 MBq). CNRs for the hot spheres and lung insert VOIs and coefficient of variation in the background are reported in **Table 4.5** for the activity levels investigated (high, medium and low) for the three reconstruction methods tested ($noSC$, DEW_{15} and TEW_{15}).

	Sphere diameter [mm]						Lung insert diameter [mm]
	10	*13*	*17*	*22*	*28*	*37*	*51*
noSC$_{15}$	2.66	6.78	9.96	14.68	24.22	31.87	50.96
DEW$_{15}$	2.47	10.07	12.98	20.96	33.99	45.35	57.17
TEW$_{15}$	0.22	8.56	13.84	21.86	40.20	56.49	55.58

Table 4.4
Contrast recovery coefficients, expressed as percentages, for the hot sphere and lung insert VOIs at medium activity level. Each value is the average from three SPECT acquisitions. noSC$_{15}$ = no scatter correction, DEW$_{15}$ = dual-energy window, TEW$_{15}$ = triple-energy window, for the 15%-wide photopeak window.

		Sphere diameter [mm]						Lung insert diameter [mm]	Background COV
		10	*13*	*17*	*22*	*28*	*37*	*51*	
noSC$_{15}$	High	0.64	1.89	3.40	7.78	10.24	12.29	3.19	16.55
	Medium	1.02	2.57	3.81	5.61	9.26	12.17	2.78	18.34
	Low	1.47	2.82	2.55	5.35	7.82	10.52	2.23	22.34
		-	-	-	-	-	-	1.51e^{-3}	1.32e^{-4}
DEW$_{15}$	High	1.20	1.99	3.36	7.85	11.95	14.84	2.96	19.60
	Medium	0.76	3.13	4.02	6.49	10.54	14.07	2.53	22.58
	Low	1.54	2.75	2.70	5.84	8.49	11.44	1.90	28.63
		-	-	-	1.9 e^{-2}	1.2 e^{-2}	6.2e^{-3}	8.67e^{-5}	1.52e^{-6}
TEW$_{15}$	High	0.24	0.98	2.77	6.31	10.40	14.51	2.15	24.99
	Medium	0.05	2.09	3.37	5.35	9.83	13.81	1.94	28.63
	Low	1.09	1.97	2.08	5.66	7.90	11.51	1.51	35.85
		-	-	-	-	4.7e^{-3}	-	2.5e^{-3}	5.48e^{-5}

Table 4.5
Contrast-to-noise ratios for the hot spheres and lung insert VOIs measured at different activity levels. In the right column, the coefficient of variation in the NEMA background, measuring the noise, is also reported. noSC$_{15}$ = no scatter correction, DEW$_{15}$ = dual-energy window, TEW$_{15}$ = triple-energy window, for the 15%-wide photopeak window.

Figure 4.7 shows CRCs (panel **A**) and CNRs (panel **B**) for DEW$_{15}$, TEW$_{15}$ and TEW$_{20}$ comparing reconstructions without and with a post-reconstruction Gaussian filter applied. When considering the biggest sphere, CRC for TEW$_{15}$ (both with and without filter) and TEW$_{20}$ (non-filtered) is higher than the DEW$_{15}$ reconstruction. CNRs, on the contrary, are comparable among reconstructions grouped by the usage of a Gaussian filter.
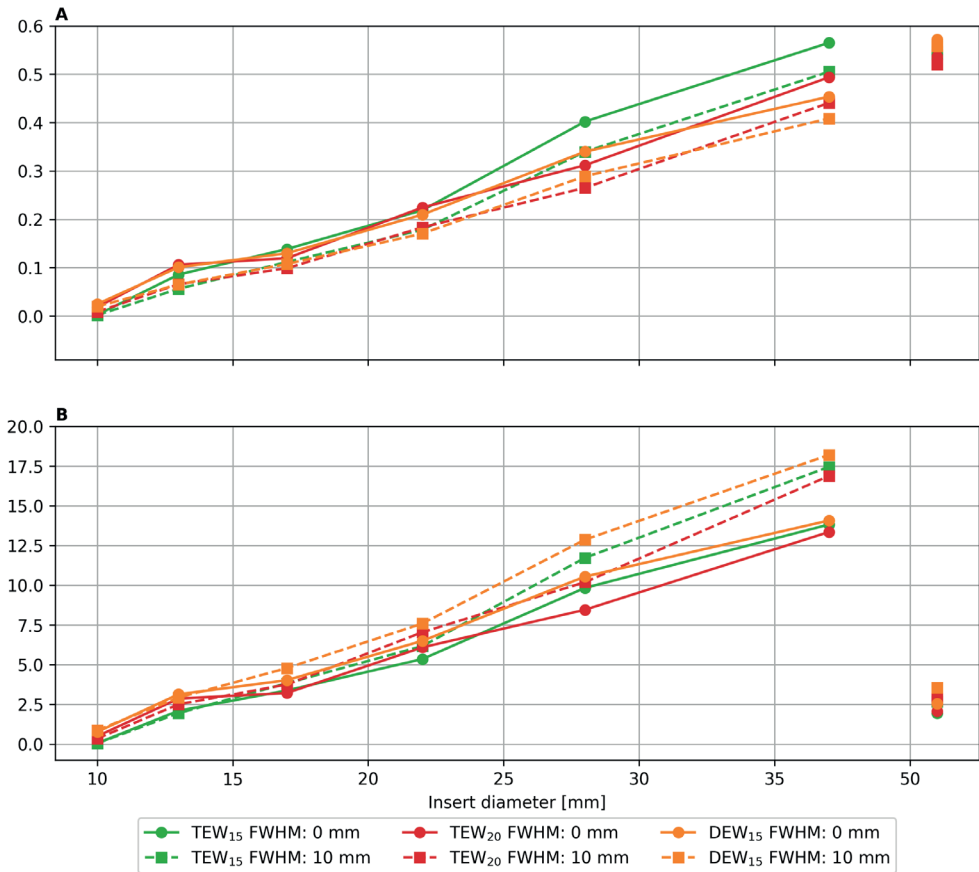
Figure 4.7

Impact of Gaussian filter and window width on the CRCs (panel **A**) and CNRs (panel **B**) for the hot sphere VOIs and the lung insert (unconnected data point). Solid line and circle markers represent reconstructions without any Gaussian filter, while dashed line and square markers represent reconstructions with a Gaussian filter size FWHM of 10 mm. Green, red and orange lines depict TEW$_{15}$, TEW$_{20}$ and DEW$_{15}$ reconstructions, respectively, for the medium activity level.

Discussions

Much effort has been invested in recent years to propose procedures to harmonize image quality, including the successful EANM Research Ltd. (EARL) accreditation program. EARL was initially aimed at harmonizing FDG-PET, and other PET tracers, but recently

proposed the first program dedicated to SPECT in order to harmonize Lutetium-177 imaging [11]. In the field of radioembolization, however, SPECT-CT imaging protocols for ^{166}Ho are still not standardized, making it difficult to compare dosimetry outcomes between centers, which may be vital to determine dose-response relationships, and thus to plan the injected activity accordingly.

The current clinical protocol for ^{166}Ho SPECT imaging is based on a 2006 study performed by de Wit *et al.* [23] in which the downscatter was corrected using an energy window centered at 118 keV. This window was positioned relatively far from the photopeak window at 81 keV in order to leave room for another energy window at 100 keV, which was used for a transmission CT with a Gadolinium-153 (^{153}Gd) source (Eγ = 97 and 103 keV). The 118 keV window provided the downscatter estimate from the high energy ^{166}Ho emissions into both the ^{166}Ho photopeak and the ^{153}Gd window. Nowadays, with most SPECT cameras being hybrid systems including a dedicated CT scanner, the 100 keV ^{153}Gd window is no longer required and the scatter window position at 118 keV is arbitrary. Reconstructing ^{166}Ho with the scatter window at 118 keV can be prone to error when setting up on new systems or in other institutions, because it is not a standard window configuration. It requires several workflow steps which may not be straightforward to set up, e.g., extracting the scatter window from the projection set and applying a k-factor before reconstruction. Furthermore, photopeak scatter was not corrected for due to the lack of a lower scatter window or the lack of Monte Carlo modeling of photopeak scatter in the clinical reconstructor. For these reasons, assessing the viability of a straightforward TEW scatter correction implementation is warranted.

In this study, an acquisition protocol for ^{166}Ho SPECT imaging has been proposed and different reconstruction methods, all clinically available, have been compared. The reconstruction methods investigated included no scatter correction (noSC$_{15}$), used as baseline, dual-energy window method (DEW$_{15}$), correcting only the downscatter and currently used in the clinical practice in our institution, and triple-energy window method (either TEW$_{15}$ or TEW$_{20}$), correcting both the down- and the photopeak- scatter and proposed as a new reconstruction method.

Reconstructions including scatter correction (either DEW or TEW based method) improve the image homogeneity in the cylindrical phantom, as shown in **Figure 4.5**, panel **D** and **E**, where the blue line (noSC$_{15}$) deviates the most from an ideal flat line (perfect scatter correction). The orange line, representing the DEW$_{15}$ reconstruction, even if closer to a flat line than noSC$_{15}$, still presents a profile which deviates from a flat line, showing a partial scatter correction (downscatter is corrected while photopeak-scatter is not). The

homogeneity further improved for the TEW$_{15}$ reconstruction which corrects for both down- and photopeak-scatter. The improved scatter correction comes at a price, however, as noise increases, as depicted in **Figure 4.5** panel **C**.

Contrast improved when both down- and photopeak- scatter were compensated for (**Figure 4.6** panel **A**), but because noise levels increased by a slightly larger factor, the contrast-to-noise ratio decreased (**Figure 4.6** panel **B**). Different activity levels did not impact the CRCs, but they did affect the noise (see **Table 4.5**) and thus the CNRs. Noise, and consequently CNRs, improve with increasing activity. CRC results for DEW$_{15}$ reconstructions are in line with findings reported by Elschot *et al.* [32]. Both hybrid Monte Carlo/window-based reconstruction [23] and full Monte Carlo simulator [32], on the contrary, seem to outperform the TEW based scatter correction method proposed in this study. However, a straightforward comparison is limited by the different method used for the CRCs computation.

Several options are available to reduce noise without increasing activity or imaging time. Among these, the image reconstruction can be smoothed with a Gaussian filter and/or the energy window width can be increased to improve count statistics. Both these parameters and their impact on CRCs and CNRs have been tested, using the DEW$_{15}$ (current clinical practice) as reference. This protocol was investigated not only to assess its impact on noise, but also to test an acquisition protocol less susceptible to a potential shift in the energy peaking of the camera. When compared to the DEW reconstructions, the higher CRCs measured for the TEW (TEW$_{15}$ with and without filter, and TEW$_{20}$ non-filtered), along with the undiminished CNRs, demonstrated the improved scatter correction when using TEW methods and the possibility to achieve higher CRCs without decreasing the CNRs.

This study was performed in a single institution using one SPECT/CT system (Siemens Symbia T16), thus the presented results are vendor specific. For this reason, a multi-center study involving five academic centers among The Netherlands and a total of seven scanners was initiated aiming to harmonize ^{166}Ho SPECT imaging. The acquisition and reconstruction protocols presented in this study (**Figure 4.1** and **Figure 4.3**) have been adopted in the multi-center study. This would allow a comparison among different centers and scanner vendor and models. For the multi-center study, a medium activity level was suggested to avoid dead time greater than 10% and to resemble the current ^{166}Ho activity used for the scout procedure (250 MBq). When available, automatic energy peaking prior to scanning was suggested. Additionally, vendor neutral reconstructions will be performed.

The analysis of this multi-center study is currently on going. Data will be shared in a publicly available repository to support institutions when setting up ^{166}Ho SPECT imaging.

Conclusion

[166]Ho SPECT imaging is lacking a clear acquisition and reconstruction protocol, easily adoptable in clinical practice. In this study, an acquisition protocol including three reconstruction methods to correct for scatter was investigated. TEW scatter correction improved the overall image quality compared to the current DEW protocol, and was straightforward to implement, thus facilitating the harmonization of [166]Ho SPECT imaging for multi-center studies.

4

PART II

Dosimetry

CHAPTER 5

^{166}Holmium SPECT dosimetry from a dual-isotope acquisition with ^{99m}Technetium

Abstract

Background: Accurate dosimetry is essential in radioembolization. To this purpose, an automatic protocol for healthy liver dosimetry based on dual isotope (DI) SPECT imaging, combining holmium-166 (^{166}Ho)-microspheres and technetium-99m (^{99m}Tc)-colloid, was developed: ^{166}Ho-microspheres used as scout and therapeutic particles and ^{99m}Tc-colloid to identify the healthy liver. DI SPECT allows for an automatic and accurate estimation of absorbed doses, introducing true personalized dosimetry. However, photon crosstalk between isotopes can compromise image quality. This study investigates the effect of ^{99m}Tc downscatter on ^{166}Ho dosimetry, by comparing ^{166}Ho-SPECT reconstructions of patient scans acquired before (^{166}Ho-only) and after additional administration of ^{99m}Tc-colloid (^{166}Ho-DI).

Methods: The ^{166}Ho-only and ^{166}Ho-DI scans were performed in short succession by injecting ^{99m}Tc-colloid on the scanner table. To compensate for ^{99m}Tc downscatter, its influence was accounted for in the DI image reconstruction using energy window-based scatter correction methods. The qualitative assessment was performed by independent blinded comparison by two nuclear medicine physicians assessing 65 pairs of SPECT/CT. Inter-observer agreement was tested by Cohen's kappa coefficient. For the quantitative analysis, two volumes of interest within the liver, VOI_{TUMOR} and $VOI_{HEALTHY}$, were manually delineated on the ^{166}Ho-only reconstruction and transferred to the co-registered ^{166}Ho-DI reconstruction. Absorbed dose within the resulting VOIs, and in the lungs (VOI_{LUNGS}), was calculated based on the administered therapeutic activity.

Results: The qualitative assessment showed no distinct clinical preference for either ^{166}Ho-only or ^{166}Ho-DI SPECT (kappa=0.093). Quantitative analysis indicated that the mean absorbed dose difference between ^{166}Ho-DI and ^{166}Ho-only was -2.00±2.84 Gy (median 27 Gy; p-value<0.00001), -5.27±8.99 Gy (median 116 Gy; p-value =0.00035) and 0.80±1.08 Gy (median 3 Gy; p-value<0.00001) for $VOI_{HEALTHY}$, VOI_{TUMOR} and VOI_{LUNGS} respectively. The corresponding Pearson's correlation coefficient between ^{166}Ho-only and ^{166}Ho-DI for absorbed dose was 0.97, 0.99 and 0.82, respectively.

Conclusion: The DI protocol enables automatic dosimetry with undiminished image quality and accuracy.

Background

Over the past decade, the number of radioembolization procedures in the treatment of liver-only or liver-dominant hepatic malignancy has rapidly increased [34]. Radioembolization is a catheter-based therapy that delivers internal radiation to tumors. Currently, three devices are commercially available: SIR-Spheres® (SIRTeX Medical Ltd.) and TheraSphere® (BTG Ltd. / Boston Scientific), both loaded with yttrium-90 (^{90}Y), and QuiremSpheres™ (Quirem Medical B.V., The Netherlands), loaded with holmium-166 ([166]Ho). Radioembolization requires a comprehensive initial safety evaluation (identifying potential non-target tissue irradiation) and assessment of intrahepatic microsphere distribution for dosimetric evaluation. Pre-treatment image-based dosimetry enables radioembolization optimization, because it allows assessment of the biodistribution of microspheres in the liver, which is often heterogeneous and clustered. Because absorbed dose and treatment outcome (toxicity and efficacy) are correlated, dosimetry should ultimately lead to improved patient selection and individualized treatment planning [47]. For this reason, prior to treatment, either ^{99m}Tc-MAA or a [166]Ho-scout dose (QuiremScout™, Quirem Medical B.V., The Netherlands) is administered to simulate the actual treatment. [166]Ho-microspheres may be preferred as simulation particles (i.e. scout dose), because they are identical to the treatment particles, which makes them superior in the prediction of the treatment dose distribution [9], [48]. Additionally, [166]Ho allows for quantitative SPECT analysis and consequently dosimetric assessment [32].

For personalized treatment planning, several dosimetric thresholds need to be determined: 1) the minimum required tumor radiation absorbed dose to obtain an adequate tumor response, 2) an acceptable healthy liver tissue absorbed dose to limit post-treatment toxicities and 3) the maximum tolerable lung shunt dose to prevent radiation pneumonitis. Obtaining these dosimetric values requires delineation of the liver, tumors and lungs using anatomical images such MRI and CT. Accurate tumor and healthy liver delineation (segmentation) and image co-registration are challenging. Segmentation is usually done manually, which is time-consuming and user dependent. Registration between anatomical images (MRI or contrast-enhanced CT), acquired hours to weeks prior to the treatment, and the functional image (SPECT) following the scout procedure is challenging due to interval deformations of the liver. Therefore, a dual-isotope SPECT/CT protocol was developed to improve dosimetry [49], having the potential to allow for the automatic delineation of tumor and healthy liver, and obviating the need for co-registration. To this end, a [166]Ho-scout dose for treatment simulation is followed by intravenously injected colloid (^{99m}Tc-stanneous phytate,

PHYTACIS® by Curium Pharma, Petten, The Netherlands). The colloid accumulates in Kupffer cells, present in healthy liver tissue and absent in tumorous tissue[50]. It allows for automatic normal liver tissue segmentation by thresholding the ^{99m}Tc image. This dual-isotope protocol enables the automatic estimation of the healthy tissue absorbed dose, which is considered to be the major dose-limiting factor. It facilitates performing dosimetry in every patient, which may lead to an improved and more personalized prescribed activity, avoiding over-dosing or, even more frequently, under-dosing the target, sacrificing efficacy for safety [51]. Dual isotope (DI) SPECT however comes with the technical challenge of correcting for the cross-talk between the two isotopes: scatter from ^{99m}Tc contaminating the main ^{166}Ho energy window and vice versa.

In previous work, van Rooij *et al.* [15]demonstrated the technical feasibility of quantitative ^{166}Ho SPECT reconstructions in the presence of ^{99m}Tc in a phantom study. These reconstructions were obtained using in-house developed Monte Carlo SPECT reconstruction software (UMCS). However, a systematic comparison between ^{166}Ho-DI SPECT and ^{166}Ho-only SPECT using patient data reconstructed using a commercially available software is required to consider this DI concept for clinical practice. For this reason, a qualitative and quantitative comparison between ^{166}Ho-only acquisitions and ^{166}Ho acquisitions in presence of ^{99m}Tc was investigated.

Materials and Methods

Study population

For all SPECT/CT acquisitions used in this study, informed consent was obtained as part of the HEPAR PLuS study [40]. Thirty-one patients with liver metastases of neuroendocrine tumors were analyzed, 29 scout (pre-treatment) procedures (average administered activity 208 ± 52 MBq) and 36 therapeutic treatments (average administered activity 5757 ± 2716 MBq). Baseline characteristics of these patients are presented in **Table 5.1**.

Two subjects were excluded because of the impossibility of segmenting the minimum desired volumes of interest (25 ml) in compliance with the defined resolution requirements for a proper absorbed dose estimate using SPECT. This constrain was introduced in order to limit the errors related to registration and dosimetry quantification accuracy, affected by small volume definition. According to the mentioned study protocol, for each of the 65 procedures considered, two SPECT/CT images were acquired after the activity injection, a ^{166}Ho-only and ^{166}Ho-DI SPECT. According to the image acquisition protocol, all scans

were performed when the total activity at the scanning time was approximately 250 MBq, enabling a comparison between pre and post-treatment images.

Characteristics	N or median	
N patient	29	
Pre-Treatment	26	
Post-Treatment	32‡	
Sex		
Male	21	
Female	8	
Age (years)*	63 ± 8	
Treatment Type	Pre-Treatment	Post-Treatment
Whole liver	21†	15†
Partial liver	5	17

Table 5.1

Characteristics of patients with neuroendocrine liver metastases treated in the HEPAR PLuS trial, included in this study.

*at first treatment, †after right side hemi hepatectomy, ‡ multiple radioembolization treatment based on the same scout procedure

Image acquisition

All patients were scanned on a Symbia T16 dual head SPECT/CT scanner (Siemens, Erlangen, Germany), using a medium-energy low-penetration collimator, on a 128 × 128 matrix (pixel spacing, 4.8 × 4.8 mm), with 120 angles (15 s per projection) over a non-circular 360° orbit. An energy window centered at the 81 keV photopeak with a width of 15% was used for both 166Ho-only and 166Ho-DI acquisitions (see **Figure 5.1**). An additional energy window centered at 118 keV (12% width) was used to correct the 166Ho photopeak data for downscatter using a window-based scatter correction [23]. 99mTc was imaged using a 140 keV, 15% wide, energy window, with an upper scatter window at 170 keV (12% width) to correct for 166Ho downscatter. The first SPECT/CT was acquired after the intra-arterial injection of 166Ho-microspheres (166Ho-only SPECT), while the second SPECT/CT was acquired 10 minutes after additional 50 MBq 99mTc-stannous phytate injection (166Ho-DI SPECT). To minimize patient motion, 99mTc-stannous phytate was administered while the patient remained on the SPECT/CT table in supine position. The optimal 166Ho - 99mTc ratio, yielding a high accuracy in DI reconstruction, was previously empirically determined by van Rooij *et al.* [15] in our institution, based on phantom data, and the resulting 5:1 166Ho - 99mTc activity ratio was adopted for this study.

SPECT reconstruction

SPECT images were reconstructed using a 3D OSEM algorithm (Flash 3D; Siemens) with 10 iterations, 8 subsets, incorporating attenuation correction. To correct for scatter during the reconstruction of the ^{166}Ho activity distribution, downscatter in the 81 keV photopeak window due to higher energy emissions of both ^{166}Ho and ^{99m}Tc was estimated from the 118 keV energy window by applying a single combined k-factor of 1.15 (see Supplemental material for details). Photopeak scatter, i.e., scattered photons originating from the 81 keV primary photopeak, was not accounted for.
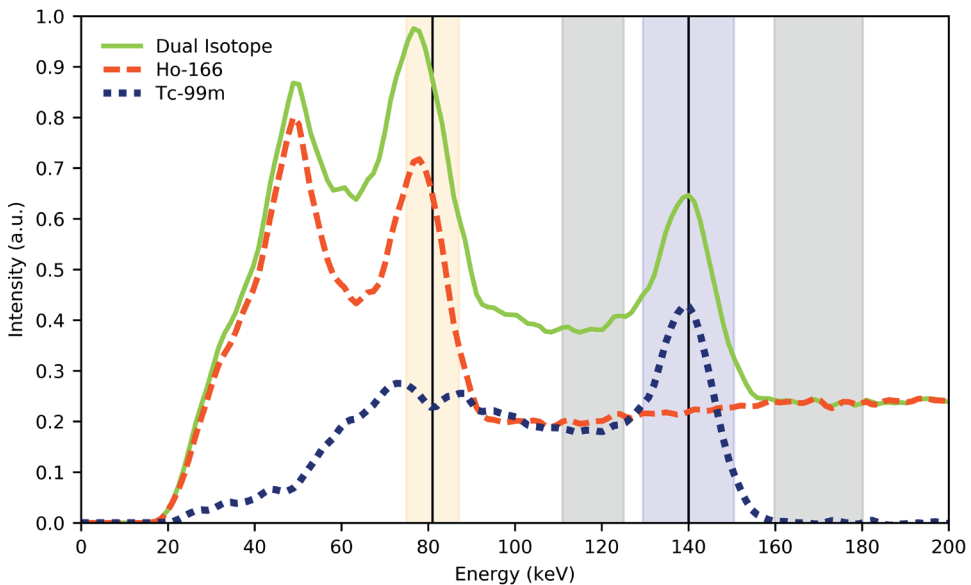
Figure 5.1
Dual Isotope energy spectrum: the solid black vertical lines at 80.6 keV (within the orange window) and 140 keV (within the blue window) denote the ^{166}Ho and ^{99m}Tc photopeak respectively. The solid green curve is the dual isotope spectrum, recorded when both ^{166}Ho and ^{99m}Tc were present, the dashed orange curve represents the ^{166}Ho spectrum. The dotted blue curve was obtained by subtracting the ^{166}Ho spectrum from the dual isotope spectrum and represents the ^{99m}Tc spectrum. Energy windows used to estimate the downscatter correction (centered at 118 keV, 12% width and at 170 keV, 12% width) are indicated in gray.

Qualitative Analysis

For the qualitative assessment, 65 pairs of SPECT/CT reconstructions (^{166}Ho-only and DI) were considered, divided into 29 scout dose SPECTs and 36 post-treatment SPECTs, a

Gaussian filter with σ = 4.2 mm was applied to reduce the noise. Two nuclear medicine physicians (M.L. and A.B., >5 years' experience) were randomly and blindly presented each pair of acquisitions (an example is depicted in **Figure 5.2**). Then they were independently asked to express clinical preference for either [166]Ho-only or DI and whether both acquisitions could be considered clinically acceptable for diagnostic purpose or not.
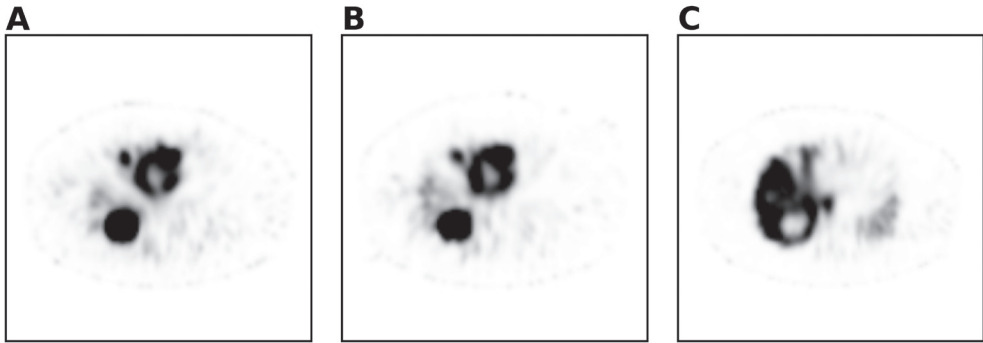
Figure 5.2

SPECT images of a 69 year old male with neuroendocrine tumor in the pancreas. The patient was diagnosed with metastatic spread to the liver, which was treated with a [166]Ho radioembolization procedure in the whole liver (prescribed activity: 9900 MBq). [166]Ho-DI (panel **A)** and [166]Ho-only (panel **B)** acquisition images have been, independently and blindly, presented to the nuclear medicine physicians for the qualitative assessment. [99m]Tc image (panel **C)** acquired during the DI protocol where an additional 50 MBq of ^{99m}Tc-colloid was administered.

Quantitative Analysis

To allow for a comparison between pre- and post-treatment data, all SPECT images were scaled to units of Bq/ml, in such a way that for each image the total activity matched the administered treatment activity, based on the assumption that the entire activity was present in the reconstructed field-of-view. Under the general assumption that microspheres remain lodged long enough for their entire activity to decay, the absorbed radiation dose in a VOI can be calculated as:

$$Dose[Gy] = 15.87 \left[\frac{mJ}{MBq}\right] \frac{Activity\ concentration\ [Bq/\text{ml}] \ * \ 10^{-6}}{VOI\ density[g/\text{ml}]}$$

Where 15.87 mJ/MBq represents the deposited energy due to the β decay of 1 MBq initial [166]Ho activity. For the liver, a soft tissue density of 1.06 g/cm^3 was applied [52], while the lung density value was set to 0.3 g/cm^3 [53], assuming, for both organs, a homogenous organ density value, constant among patients. Since the mean penetration of the β emission of

^{166}Ho (2.5 mm) is small compared to the voxel size (4.8 mm), all energy was assumed to be absorbed within the considered voxel [48]. The β radiation accounts for 96% of the emitted energy (=15.87 mJ/MBq), the other 4% of the energy is for the most part emitted through γ radiation. Because of the relatively large penetration distance of these γ and the inverse square law, the absorbed radiation dose due to γ emissions was ignored in this study.

For the assessment of the mean absorbed dose in the liver, all of the ^{166}Ho-DI SPECT/CT images were co-registered with the corresponding ^{166}Ho-only SPECT/CT images to compensate for possible patient movement during the time lag between the two acquisitions (10 minutes to account for ^{99m}Tc-stannous phytate injection and distribution). Since the patient remained on the table, a rigid registration was performed. The registration was carried out with Elastix [36], based on the SPECT related LDCT (primarily used to compute the attenuation correction map), using an adaptive stochastic gradient descendent approach as optimizer and a mutual information metric. Subsequently, two volumes of interest (VOIs) for each pair of acquisitions were manually defined on the ^{166}Ho-only SPECT/CT: $VOI_{HEALTHY}$ (3D ellipsoidal shape within the healthy liver), and VOI_{TUMOR} (one manually segmented tumor among the multiple tumors present), as depicted in **Figure 5.3** panel **B**. For both $VOI_{HEALTHY}$ and VOI_{TUMOR}, it has been decided to constrain the minimum volume to 25 ml, to ensure a reliable activity recovery. These VOIs were applied to the co-registered ^{166}Ho-DI SPECT to compute the mean absorbed dose within these VOIs for comparison.

To estimate the mean lung shunt dose, the lungs were semi-automatically delineated on both the corresponding ^{166}Ho-only CT and ^{166}Ho-DI CT images with Q-suite™ software (Quirem Medical B.V., The Netherlands). Before the lung masks were applied to the SPECT reconstructions for the absorbed dose computation, the delineations were shrunk by 2 cm to avoid any partial volume effect close to the edges and to minimize the influence of scatter from activity in the liver.

The mean absorbed dose, expressed in gray [Gy], was chosen as the metric for comparison since it was deemed the most clinically relevant parameter. The dose difference between ^{166}Ho-DI and ^{166}Ho-only was reported, since it was considered more relevant from a clinical point of view than a relative measurement (e.g. percentage difference).

Statistical analyses

In each comparative analysis, the ^{166}Ho-only SPECT/CT images were considered as reference standard. Inter-observers' agreement was measured by means of Cohen's kappa statistic (κ) [54], for the qualitative assessment. For this analysis it was assumed that ^{166}Ho-

only and 166Ho-DI SPECT/CT data were paired, as both scans were acquired within a short time interval (<10 minutes), with patient and bed table in the same position. Pre and post-treatment results were also independently reported for completeness of the data presented. To compare the absorbed dose in the VOIs between 166Ho-only and 166Ho-DI, after a visual assessment for data normality, Bland Altman analyses were performed. For each plot, the mean absorbed dose difference between 166Ho-DI and 166Ho-only, expressed in Gy, and limits of agreements (LoA), [Gy], were reported. LoA are computed as mean ± coefficient of reproducibility (CRP), equal to 1.96*standard deviation. The linear correlation between absorbed dose in 166Ho-only and 166Ho-DI was expressed in terms of the Pearson correlation coefficient r. In addition, two-sided paired T-test (at $\alpha = 0.05$) was performed to check the statistical difference between mean absorbed dose based on 166Ho-only and on 166Ho-DI SPECT (null hypothesis is no difference between mean absorbed dose values computed on 166Ho-only and on 166Ho-DI SPECT).
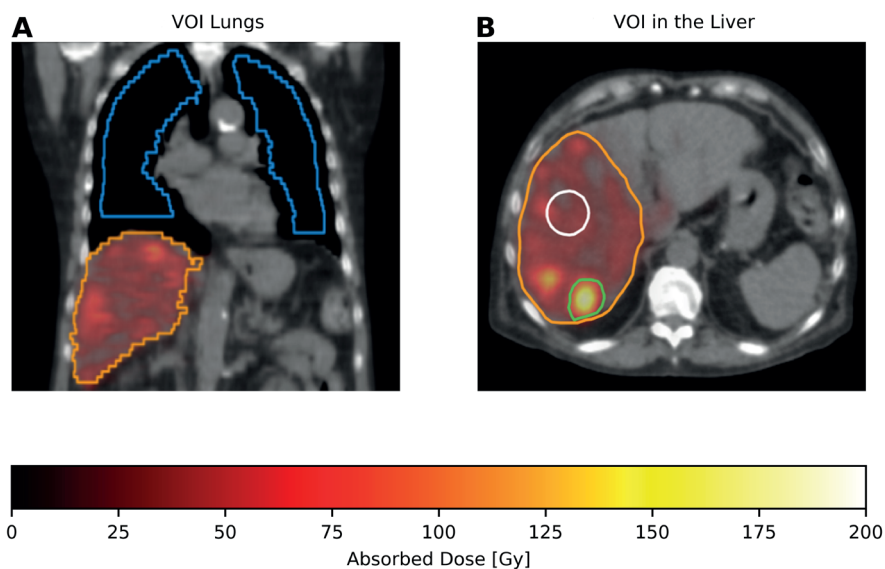
Figure 5.3
166Ho-SPECT/CT images of a 70 year old male diagnosed with multiple liver metastases of neuroendocrine origin, after receiving a 166Ho radioembolization treatment (right liver lobe, 4207 MBq). Panel **A** shows the coronal view where the orange line defines the treated liver and the blue line depicts the semi-automatically delineated lungs, after the shrinkage process. Panel **B** shows the axial view of the liver with 3 VOIs superimposed: orange line delineates the treated liver (right lobe), green line delineates the tumor (VOI_{TUMOR}) while white line defines the $VOI_{HEALTHY}$.

Results

Qualitative Analysis

According to the qualitative assessment carried out by two expert nuclear medicine physicians, all [166]Ho-SPECT reconstructions were considered reliable for a diagnostic purpose. Based on their preference for either [166]Ho-only or [166]Ho-DI, their inter observer agreement (Cohen's kappa coefficient) was equal to 0.09 (k = -0.63 and k = 0.14 for pre-treatment and post-treatment data respectively). The Cohen's k value, close to 0, shows the lack of agreement on a favorite imaging option ([166]Ho-only or [166]Ho-DI). Moreover, both were considered suitable for diagnostic use. Therefore, no distinct preference for either one of the reconstructions for use in clinical practice could be concluded.

Quantitative analysis

The constraint in volume for the VOIs (≥ 25 ml), led to the exclusion of 21 procedures for the VOI_{TUMOR}, and of 7 procedures for the $VOI_{HEALTHY}$, since they did not satisfy this requirement. The lower limit for the VOI volume was introduced to ensure an adequate dose recovery. The included dataset is reported in **Table 5.2**.

A	Pre-Treatment		Post-Treatment	
VOI	Number	Volume	Number	Volume
Healthy	26	27.57 ml	32	27.57 ml
Tumor	21	27.50 ml ± 3.91	23	26.27 ml ± 2.23
Lungs	26	2399.30 ml ± 971.77 ([166]Ho-Only)	31	2578.09 ml ± 1026.67 ([166]Ho-Only)
		2182.47 ml ± 794.58 ([166]Ho-DI)		2263.47 ml ± 841.22 ([166]Ho-DI)
B	[166]**Ho-only**		[166]**Ho-DI**	
VOI	Median	Quartile Deviation (IQR/2)	Median	Quartile Deviation (IQR/2)
Healthy	27.12 Gy	7.08 Gy	26.22 Gy	8.00 Gy
Tumor	116.27 Gy	44.91 Gy	108.96 Gy	46.00 Gy
Lungs	2.99 Gy	0.99 Gy	3.88 Gy	1.07 Gy

Table 5.2
Quantitative dataset characteristics. **A** top row reports the number of $VOI_{HEALTHY}$ and related volume value (mean and standard deviation) for both pre- and post-treatment dataset, the middle row refers to VOI_{TUMOR}; while the bottom row illustrates the data related to VOI_{LUNGS} with volumes values after the shrinkage process for both [166]Ho-only and [166]Ho-DI. **B** median and quartile deviation of mean absorbed dose recovered in VOIs, for both [166]Ho-only and [166]Ho-DI are reported. First row refers to $VOI_{HEALTHY}$, second to VOI_{TUMOR} and third to VOI_{LUNGS} respectively.

The results, for each of the three VOIs, for both the dataset considered entirely and split among pre- and post-treatment data, are reported in **Table 5.3**.

		VOI $_{HEALTHY}$	VOI $_{TUMOR}$	VOI $_{LUNGS}$
All Data	Average ± SD [Gy]	- 2.00 ± 2.84	- 5.27 ± 8.99	0.80 ± 1.08
	Limits of Agreement [Gy]	- 7.56 + 3.56	- 22.89 +12.35	- 1.32 +2.92
Pre-Treatment Data	Average ± SD [Gy]	- 2.69 ± 3.23	- 4.51 ± 8.69	0.86 ± 1.24
	Limits of Agreement [Gy]	- 9.02 + 3.64	- 21.54 + 12.52	- 1.57 + 3.29
Post-Treatment Data	Average ± SD [Gy]	- 1.44 ± 2.27	- 5.96 ± 9.01	0.74 ± 0.92
	Limits of Agreement [Gy]	- 5.89 + 3.01	- 23.62 + 11.70	- 1.06 + 2.54

Table 5.3
Mean Absorbed Dose Difference (^{166}Ho-DI - ^{166}Ho-only), standard deviation, and lower and upper limits of agreement for VOIs of interest (VOI$_{HEALTHY}$, VOI$_{TUMOR}$ and VOI$_{LUNGS}$). Top row depicts values for the dataset considered entirely, while middle and bottom row report values for pre- and post-treatment data, respectively.

Bland Altman plots for VOI$_{HEALTHY}$, VOI$_{TUMOR}$ and VOI$_{LUNGS}$ are shown in **Figure 5.4** panel **A**, **B** and **C**, respectively. The mean absorbed dose difference between ^{166}Ho-DI and ^{166}Ho-only was negative for the VOIs within the liver, while it was slightly positive for VOI$_{LUNGS}$. CRP was equal to 5.56 Gy for VOI$_{HEALTHY}$, 17.62 Gy for VOI$_{TUMOR}$ and 2.12 Gy for VOI$_{LUNGS}$.

The linear correlation between ^{166}Ho-only and ^{166}Ho-DI, assessed using Pearson's correlation coefficient (depicted in **Figure 5.4** panel **D-E-F**), was equal to 0.99 for VOI$_{TUMOR}$ (for both pre- and post-treatment data), 0.97 for VOI$_{HEALTHY}$ (r=0.96 for pre- and r=0.98 for post-treatment data) and 0.82 for VOI$_{LUNGS}$ (r=0.72 for pre- and r=0.89 for post-treatment data).

T-test p-values results are <0.00001, 0.00035 and <0.00001 for VOI$_{HEALTHY}$, VOI$_{TUMOR}$ and VOI$_{LUNGS}$ respectively.

5
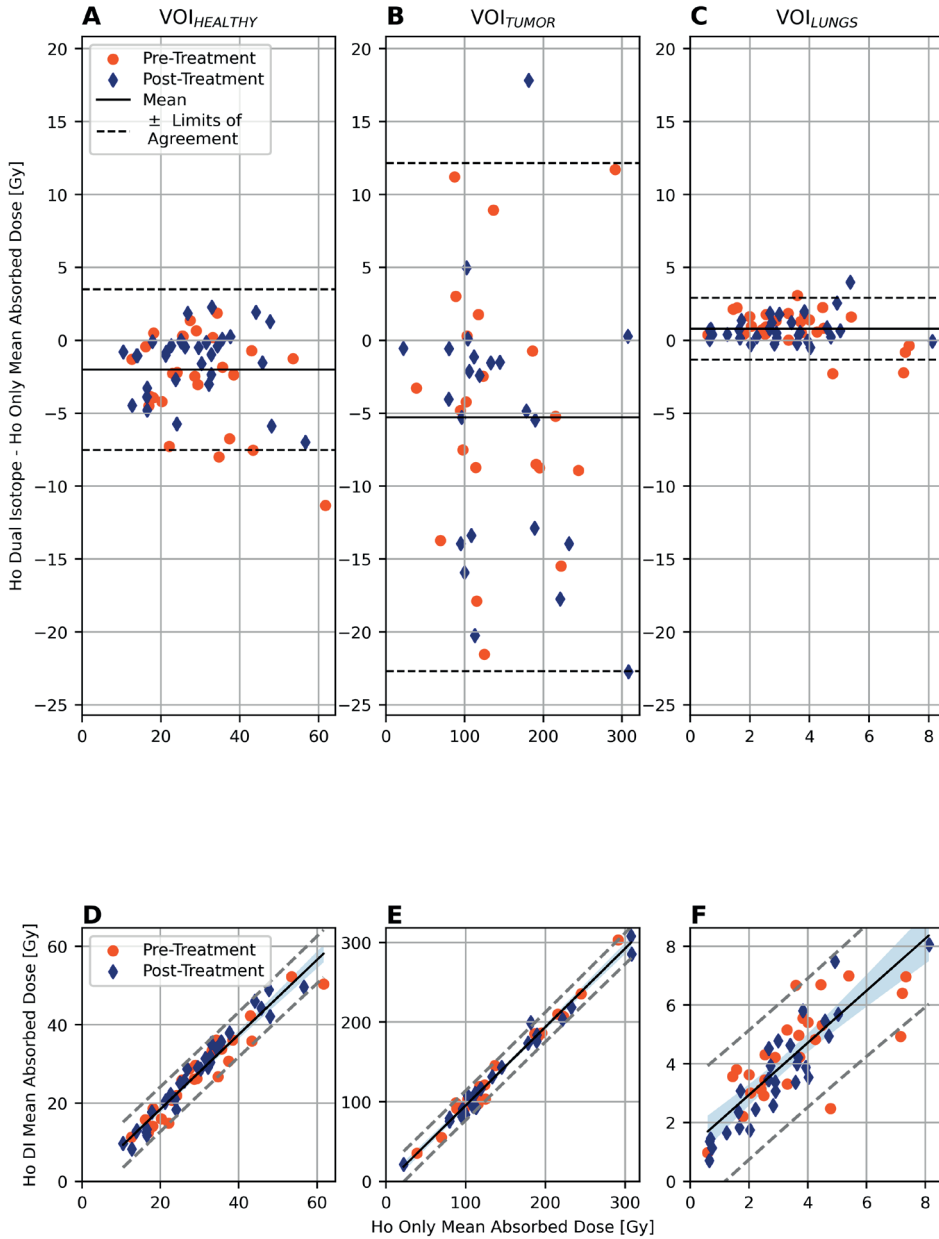
Figure 5.4

Bland-Altman plot (difference between mean absorbed dose recovered in [166]Ho-DI and in [166]Ho-only against mean absorbed dose in [166]Ho-only) is depicted in the bottom row. Orange circles refer to pre-treatment dataset while blue diamonds to post-treatment. Mean of difference between absorbed dose recovered in [166]Ho-DI and in [166]Ho-only ($\overline{dose}$ [166]Ho-DI − $\overline{dose}$ [166]Ho-only) is depicted by the black solid line,

Figure 5.4 (Continued)

while black dashed lines define ± limits of agreement. Data in panel **A** refers to VOI$_{\text{HEALTHY}}$, in panel **B** to VOI$_{\text{TUMOR}}$ and panel **C** depicts data referring to VOI$_{\text{LUNGS}}$. Linear correlation plot between ^{166}Ho-only and ^{166}Ho-DI with respect to the mean absorbed dose for VOI$_{\text{HEALTHY}}$ (**D**), VOI$_{\text{TUMOR}}$ (**E**) and VOI$_{\text{LUNGS}}$ (**F**), subdivided between pre-treatment (circles) and post-treatment (diamonds), is reported in the bottom row. The solid line depicts linear regression, while the dashed lines indicate the ± 95% confidence intervals.

Discussions

In this study, the qualitative and quantitative accuracy of a ^{166}Ho reconstruction derived from a DI acquisition was investigated. The inter-observer agreement (κ = 0.093) indicated no specific preference for either the ^{166}Ho-only or DI acquisition in the qualitative analysis. The quantitative analysis demonstrated a good correlation between ^{166}Ho-only and ^{166}Ho-DI with a Pearson's correlation coefficient > 0.95 for both VOI$_{\text{HEALTHY}}$ and VOI$_{\text{TUMOR}}$ and 0.82 for VOI$_{\text{LUNGS}}$. The difference between mean absorbed dose between ^{166}Ho-only and ^{166}Ho-DI SPECT was statistically significant for all VOIs (p-value < *0.0005*), however the mean difference was considered clinically not relevant. The limits of agreement for the difference between ^{166}Ho-DI and ^{166}Ho-only were deemed acceptable by experienced nuclear medicine physicians. Because assessments of dose to the tumor, healthy liver and lungs serve a different purpose clinically, physicians defined different acceptable limits of agreement for each category prior to this study. A mean difference of 2 Gy with a limit of agreement of ±5 Gy was considered adequate for healthy liver assessment (median absorbed dose for ^{166}Ho-only VOI$_{\text{HEALTHY}}$: 27 ± 7.08 Gy), being the dose-limiting factor for radioembolization treatments. A less restrictive value may be applied for the absorbed dose in the tumor because the clinical range for efficacy is variable and not well defined (median absorbed dose for ^{166}Ho-only VOI$_{\text{TUMOR}}$: 116 ± 44.91 Gy). With respect to the lungs, according to ^{166}Ho-miscrospheres instructions for use [11], a predicted average lung absorbed dose > 30 Gy is a contraindication for the radioembolization treatment. In this study, the clinical acceptable deviation from the difference between ^{166}Ho-only and ^{166}Ho-DI was defined at approximately 3 Gy. This overestimation prevents underestimation of the lung absorbed dose (median absorbed dose for ^{166}Ho-only VOI$_{\text{LUNGS}}$: 3 ± 0.99 Gy). For all VOIs, 95% of the data was well within the corresponding clinically acceptable limits of agreement

Even though rarely encountered (<1%) [55], radiation pneumonitis is a serious complication that can occur when microspheres inadvertently shunt to the lung parenchyma. So far, lung shunt fraction (LSF) has been the most used metric in clinical routine to determine

the activity that shunts to the lungs. Counts in liver and lungs are determined on planar scintigraphy. Despite that the inadequacy of this approach has been demonstrated in multiple studies [33], it is still used in clinical practice. Within the scope of this study, to estimate the difference in the mean absorbed dose between ^{166}Ho-DI and on ^{166}Ho-only in the VOI_{LUNGS}, the lungs were delineated on the corresponding attenuation correction LDCT. However, the lungs were not always entirely visible within the field of view of the SPECT. This drawback is negligible in case the lung perfusion is homogeneous, but this assumption is not always correct [56][57]. In addition, the very low values of mean absorbed dose in VOI_{LUNGS}, were more affected by this drawback. This explains the lower Pearson correlation coefficient (0.82) and the higher number of outliers.

The use of the proposed DI protocol has potential benefits, amongst which the possibility to (semi) automatically identify and delineate tumor and healthy tissue within a single SPECT/CT acquisition. Additionally, simultaneous acquisition of both isotopes avoids the registration difficulties, both being time consuming and prone to additional errors in dosimetry.

SPECT images showing either ^{99m}Tc distribution or ^{166}Ho accumulation can be processed to obtain an automatic delineation of the regions of interest. Healthy liver might be delineated on the ^{99m}Tc reconstruction while tumor lesions presenting focused ^{166}Ho uptake can be delineated on the ^{166}Ho image. The definition of these two compartments is a requirement for the use of the partition model [35]. This method allows the determination of a selective prescribed activity aiming at maximization of the absorbed dose to the tumor tissue, while restricting radiation absorbed dose to the healthy tissue.

Some limitations apply to this study. All images were acquired with the same SPECT/CT scanner, which restricts the used k-factor to this imaging setup. Nonetheless, it is possible to extend this study to other scanners (see Supplemental material). Furthermore, the liver VOIs were manually segmented to ensure an adequate volume definition, similar among all datasets (as can be seen in **Table 5.2**), and to avoid the introduction of errors due to thresholding of the ^{99m}Tc images. Because of the need to apply the same VOIs to both ^{166}Ho-only and ^{166}Ho-DI for tumor and healthy liver, a co-registration process was involved. This can lead to small misalignments, which may have impacted on the mean absorbed dose difference. In addition, tumors with a volume smaller than the 25 ml considered for this study could be more affected by registration related error and partial volume effect which will further hamper the tumor dosimetry quantification.

To cope with the mentioned limitations, some future steps can be taken. A phantom experiment could help to determine the accuracy with which it is possible to recover the

absorbed dose at different activity concentration, both with and without the presence of ^{99m}Tc-colloid. To compensate for the lungs region just partially covered by the SPECT field of view, it could be possible to implement a two-bed position protocol to cover both the liver and the abdominal region. An assessment of ^{99m}Tc crosstalk impact on [166]Ho acquisitions stratified by volume of interest dimensions, could provide a better insight in the possibility to perform [166]Ho-DI acquisition without being hampered by an increase effect of partial volume effect due to the presence of an additional isotope.

The possibility to skip the [166]Ho-only SPECT/CT acquisition has a beneficial effect on patients, decreasing the discomfort related to an imaging procedure that takes half an hour. Further analysis is required to implement a clinical workflow to automatically process information derived from the DI protocol and obtain personalized planning for radioembolization.

Conclusion

Based on a qualitative, as well as a quantitative analysis on patient data, a [166]Ho-DI SPECT can be safely used instead of a [166]Ho-only acquisition. The differences between the [166]Ho-only and [166]Ho-DI protocol reconstructions were considered to be clinically acceptable and thus the dual isotope protocol can be adopted in clinical practice.

Supplemental material

k-factor analysis

The downscatter in the 81 keV window can be expressed as the sum of the contributions from ^{166}Ho and ^{99m}Tc separately:

$$S_{81} = S_{81}^{Tc} + S_{81}^{Ho} \tag{I},$$

where S_{81} is the total downscatter estimate in the 81 keV window and S_{81}^{Tc} and S_{81}^{Ho} represent the individual scatter contributions from ^{99m}Tc and ^{166}Ho respectively. These only include scattered photons originating from higher energy emissions (including bremsstrahlung from the β^- emissions), but not the photopeak scatter (originating from the primary 81 keV photopeak). These contributions can be estimated from the 118 keV window, using their individual k-factors:

$$S_{81}^{Tc} = k_{118 \to 81}^{Tc} * S_{118}^{Tc} \tag{II},$$

and similarly for ^{166}Ho:

$$S_{81}^{Ho} = k_{118 \to 81}^{Ho} * S_{118}^{Ho} \tag{III},$$

where the $k_{E1 \to E2}^{A}$ are the k-factors for isotope A to estimate scatter in window E2 from window E1. Because the 118 keV energy window does not cover any gamma emission lines, the projection images recorded in the 118 keV window (P_{118}) are composed of the sum of the scatter contributions S_{118}^{Tc} and S_{118}^{Ho}, and hence, $S_{118}^{Tc} = P_{118} - S_{118}^{Ho}$. Furthermore, since the 170 keV energy window contains counts from ^{166}Ho downscatter exclusively, S_{118}^{Ho} can be estimated from the projection images recorded in the 170 keV window (P_{170}) as: $S_{118}^{Ho} = k_{170 \to 118}^{Ho} * P_{170}$. Thus S_{118}^{Tc} can be written as $S_{118}^{Tc} = P_{118} - k_{170 \to 118}^{Ho} * P_{170}$. Substituting in (II) and (III) yields:

$$S_{81}^{Tc} = k_{118 \to 81}^{Tc} * (P_{118} - k_{170 \to 118}^{Ho} * P_{170})$$

and:

$$S_{81}^{Ho} = k_{118 \to 81}^{Ho} * k_{170 \to 118}^{Ho} * P_{170}.$$

After rearranging, equation (I) can be expressed in terms of the projection images recorded in the 118 keV and 170 keV windows:

$$S_{81} = k^{Tc}_{118\to81} * P_{118} + \left(k^{Ho}_{118\to81} - k^{Tc}_{118\to81}\right) * k^{Ho}_{170\to118} * P_{170} \tag{IV}$$

The factors $k^{Ho}_{118\to81}$ and $k^{Ho}_{170\to118}$ can be estimated from measurement because the windows do not contain any gamma emission lines.

The factor $k^{Ho}_{118\to81}$, however, cannot be measured directly due to the ^{166}Ho photopeak in the 81 keV window. Using a Monte-Carlo simulation, the 81 keV ^{166}Ho gamma emission line can be artificially ignored such that the simulated projections only contain downscatter contributions, similar to the 118 keV window. In previous work, using a digital anthropomorphic phantom (XCAT), $k^{Ho}_{118\to81}$ was simulated to be 1.15 [26]. This method was repeated for this work, but using the patient scans rather than the digital phantom, resulting in a k-factor of 1.17 (see **Table 5.4**).

	Width dependent	Width independent
$k^{Ho}_{170\to140}$	0.97	0.95
$k^{Ho}_{170\to118}$	0.61	0.88
$k^{Ho}_{170\to81}$ *	0.77	1.30
$k^{Ho}_{118\to81}$ *	1.17	1.37
$k^{Tc}_{118\to81}$	1.15	1.34

Table 5.4
Median values for the computed k-factors, reported both energy window width dependent (i.e., specific to the window widths applied in this work) and independent. Subscripted values refer to the energy windows considered, the corresponding isotope is superscripted.
*Downscatter simulation excluding photopeak

In this work, the factor $k^{Tc}_{118\to81}$ (and $k^{Ho}_{170\to118}$ similarly) was computed by dividing the counts in the 81 keV and 118 keV energy window of ^{99m}Tc (or ^{166}Ho) projections. More specifically, for every projection angle (120 in total) a relevant Region of Interest (ROI) was determined by thresholding the corresponding 140 keV ^{99m}Tc projection image (20% of maximum intensity after smoothing with a 15mm Gaussian filter). The sum of counts within the ROIs in both windows (81 keV and 118 keV) was divided for each angle and a k-factor was determined as the mean over all angles, as shown in **Figure 5.5** panel **A**. This procedure was repeated for 65 patient scans to obtain a median k-factor of $k^{Tc}_{118\to81}$=1.15, as it is marked with the solid line in **Figure 5.5** panel **C**, with a quartile deviation equal to 0.05.
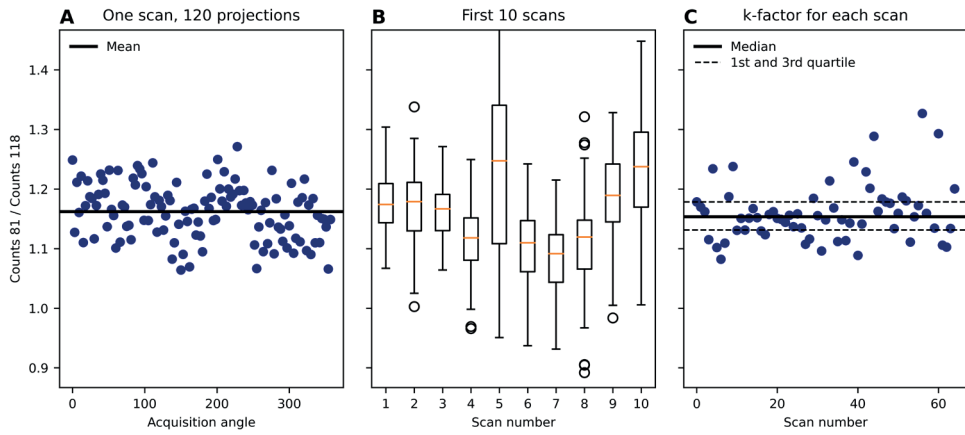
Figure 5.5

Panel **A** depicts the ratio between counts, due to ^{99m}Tc downscatter, in the 81 keV and 118 keV energy windows, for each acquisition angle, for a single patient. The solid black line represents the mean value over the acquisition angles. Panel **B** shows the box plots indicating the median and interquartile ranges (IQR) of the count ratios for the first 10 patient scans (whiskers indicate the range, excluding points further than 1.5 IQR from the box). Panel **C** shows the mean ratios for all the scans, with a solid line representing the overall median value (1.15), and 1st and 3rd quartiles (dashed lines)

Because $k^{Ho}_{118\to81}$ and $k^{Tc}_{118\to81}$ do not differ significantly (see **Table 5.4**), Eq. IV can be approximated as:

$$S_{81} = k^{Tc}_{118\to81} * P_{118}.$$

As the P_{170} contribution is negligible since the $(k^{Ho}_{118\to81} - k^{Tc}_{118\to81}) * k^{Ho}_{170\to118}$ term is equal to 0.01. Therefore, to estimate the downscatter in the 81 keV window, a k-factor of 1.15 can be applied independent of the relative contributions of ^{166}Ho and ^{99m}Tc. However, it is dependent on average patient geometry, definition of energy windows and collimator/detector specifics. The computed k-factors are reported in the **Table 5.4** (median values reported for both window width dependent and independent measurements).

5

CHAPTER 6

Automatic healthy liver segmentation for ^{166}Holmium radioembolization dosimetry

Abstract

Background: Dosimetry is crucial to plan and evaluate holmium-166 liver radioembolization. To this purpose, healthy liver definition is required. The current clinical standard relies on manual segmentation and registration of a separately acquired contrast enhanced CT (CECT), a prone-to-error and time-consuming task. An alternative is offered by simultaneous imaging of holmium-166 and technetium-99m stannous-phytate that accumulates in healthy liver cells (^{166}Ho-^{99m}Tc dual isotope protocol). This study compares healthy liver segmentation performed with an automatic method using ^{99m}Tc images derived from a ^{166}Ho-^{99m}Tc dual isotope acquisition to the manual segmentation, focusing on healthy liver dosimetry and corresponding hepatotoxicity.

Methods: Data from HEPAR PLuS study were included. For each procedure, a ^{166}Ho-^{99m}Tc dual isotope SPECT/CT was acquired. Automatic healthy liver segmentation was obtained by thresholding the ^{99m}Tc image, while manual segmentation was performed by a physician on CECT, and then manually registered to the corresponding SPECT/CT. The resulting segmentations were applied to the corresponding ^{166}Ho SPECT to compute the absorbed dose in healthy liver.

Results: 31 patients (66 procedures) were assessed. Manual segmentation and registration took a median of 30 minutes per patient, while automatic was instantaneous. Mean ± standard deviation of healthy liver absorbed dose was 18 Gy ± 7 Gy and 20 Gy ± 8 Gy for manual and automatic segmentations, respectively. Mean difference ± coefficient of reproducibility between healthy liver absorbed doses using the automatic versus manual segmentation was 2 Gy ± 6 Gy. No correlation was found between mean absorbed dose in the healthy liver and hepatotoxicity.

Conclusion: The ^{166}Ho-^{99m}Tc dual isotope protocol can be used to automate the healthy liver segmentation without hampering the ^{166}Ho dosimetry assessment.

Background

Radioembolization, also known as selective internal radiation therapy, has been used for many years for treatment of non-operable primary and/or secondary liver lesions. Among commercially available devices, holmium-166 ([166]Ho) loaded microspheres (QuiremSpheres™/ QuiremScout™, Quirem Medical B.V., The Netherlands) allows the use of the same particles for dosimetric assessment during treatment planning and for post-treatment evaluation.

In line with conventional radiation oncology, dosimetry, defined as amount of absorbed dose delivered by ionizing radiation, plays a key role both during treatment planning and for the post-treatment evaluation phase.

For hepatic radioembolization, dosimetry is calculated using a partition model which assumes that the liver can be divided in distinct volumes of interest (VOIs), corresponding to different sets of compartments: healthy liver and tumors [58]. Current clinical practice for [166]Ho radioembolization relies on manual segmentation of these compartments on a previously acquired contrast enhanced CT (CECT) or MRI, and its subsequent registration to the low dose CT (LDCT) accompanying the SPECT. These two tasks, manual segmentation and registration, present multiple drawbacks: they are time-consuming and prone-to-error. Additionally, the manual segmentation and registration introduce an inter-observer variability [59]. These drawbacks might prevent the systematic implementation into clinical practice, ultimately hampering a personalized approach to dosimetry and might impair the post-treatment validation, hindering the determination of a dose-response and potential treatment outcome prediction.

An alternative to manual segmentation and the consequent manual registration is provided in a protocol based on the simultaneous imaging of [166]Ho, simulating the distribution of microspheres [21] in tumors and healthy liver tissue, and technetium-99m (^{99m}Tc) stannous-phytate, accumulating in Kupffer cells located only in healthy tissue ([166]Ho-^{99m}Tc dual isotope) [14]. As Kupffer cells are absent in tumorous tissue, this allows an easy differentiation between tumorous and healthy liver tissue, enabling physiological healthy liver tissue delineation based on ^{99m}Tc stannous-phytate uptake [15].

Additional to the [166]Ho isotope used for treatment planning and validation, 50 MBq of ^{99m}Tc stannous-phytate is intravenously injected only right before start of the SPECT/CT as the kinetic uptake is fast. This allows simultaneous acquisition of the two isotopes (dual-isotope acquisition), [166]Ho and ^{99m}Tc, which can then be reconstructed into a [166]Ho and a ^{99m}Tc image, visualizing therapy distribution and healthy liver tissue segmentation, respectively [15]. This protocol was applied in a clinical study (HEPAR PLuS) and feasibility of dosimetry on [166]Ho images deriving from this dual-isotope acquisition was previously demonstrated [27].

Reconstruction parameters for both ^{166}Ho and ^{99m}Tc SPECT were previously analyzed in a phantom study and used in this study [60].

The aim of this study is to compare dosimetric assessments by manual segmentation (current standard clinical practice) versus the proposed automatically defined healthy liver VOI using the ^{166}Ho-^{99m}Tc dual-isotope protocol. Furthermore, based on the automatic healthy liver segmentations and the corresponding dosimetry results, the dose-hepatotoxicity relation will be investigated.

Materials and Method

Data Population

For all SPECT/CT acquisitions used in this study, informed consent was obtained as part of the HEPAR PLuS study (NCT02067988) [13],[40]. The study has been approved by the institutional review board, and all subjects signed an informed consent form. This study included 31 patients with liver metastases of neuroendocrine tumors (NET), 33 pre-treatment procedures and 38 therapeutic treatments. Baseline characteristics are presented in **Table 6.1**. According to study protocol, for each of the procedures, a SPECT/CT image was acquired after additional activity injection of ^{99m}Tc stannous-phytate. For the dataset under consideration, lung shunt was previously reported [27].

Images acquisition and reconstruction

All patients were scanned on a Symbia T16 dual head SPECT/CT scanner (Siemens, Erlangen, Germany), using a medium-energy low-penetration collimator, on a 128 × 128 matrix (pixel spacing, 4.8 × 4.8 mm), with 120 angles (15 s per projection) over a non-circular 360° orbit. An energy window centered at 81 keV photopeak with a width of 15%, together with an additional energy window centered at 118 keV (12% width) to correct the ^{166}Ho photopeak data for downscatter using a window-based scatter correction were used [60]. ^{99m}Tc was imaged using a 140 keV, 15% wide, energy window, with an upper scatter window at 170 keV (12% width) to correct for ^{166}Ho downscatter. ^{99m}Tc was reconstructed with triple-energy-window scatter correction, using both 118 keV and 170 keV scatter windows. SPECT/CT was acquired following the ^{166}Ho radioembolization procedure when activity had decayed to approx. 250 MBq, to avoid dead time effects. Right before the SPECT scan, ~50 MBq of ^{99m}Tc stannous-phytate to perform the simultaneous ^{166}Ho-^{99m}Tc dual-isotope acquisition is intravenously injected while the patient remained on the SPECT/CT table in

supine position. Reconstruction parameters for both [166]Ho and ^{99m}Tc SPECT were previously analyzed in a phantom study and used in this study [60]. Data were retrospectively assessed to compute the dose in the healthy liver VOI. To this purpose, two approaches were used: manual segmentation and manual rigid registration of CECT on top of SPECT, currently used in standard clinical practice, and the automatic segmentation on intrinsically registered ^{99m}Tc SPECT using a threshold based method.

	N (%)
Number of patients	31
Age - median (IQR)[*]	65.1 (57.6–70.2)
Gender	
Male (%)	23 (74.2%)
Female (%)	8 (25.8%)
Origin of tumor	
Pancreas	10 (32.3%)
Small intestine	8 (25.8%)
Colorectal	4 (12.9%)
Lung	3 (9.7%)
Unknown primary	6 (19.4%)
ECOG	
0	17 (54.8%)
1	13 (41.9%)
2	1 (3.2%)
WHO Grade	
1	12
2	19
Tumor[†] burden in % - median (IQR)	6.9% (3.1–22.5%)
Procedures	70
Pre-treatment	32
Post-treatment	38
Holmium-166 activity in GBq – median (IQR)	5.4 (3.6 – 8.0)
Technetium-99m activity in MBq – median (IQR)	52 (50 - 53)

Table 6.1
Baseline characteristics of patients with neuroendocrine liver metastases treated in the HEPAR PLuS trial
[*]at first treatment
[†]it refer to tumor computed on the CECT acquired at the baseline

Manual segmentation

For each patient, healthy liver and tumor VOI were manually segmented by an experienced nuclear medicine physician using commercially available software dedicated to [166]Ho

radioembolization (Q-Suite™ 2.1, Quirem Medical B.V., The Netherlands). Delineation of VOI was performed on pre-treatment CECT, up to several weeks before treatment. Subsequently, the CECT was rigidly registered on the SPECT acquired after the [166]Ho administration procedure through the corresponding LDCT intrinsically registered to the SPECT. Healthy liver VOI was defined by subtracting the manually segmented tumor VOI from total liver volume VOI. Additionally, necrotic tissue was manually segmented as well, to be excluded from healthy liver VOI. Only tumors with a diameter greater than 1 cm were included in the VOI processing. Manual segmentation time for each patient was recorded.

Automatic segmentation

Since ^{99m}Tc stannous-phytate accumulates also in the spleen, a preliminary procedure was applied to remove the spleen from the ^{99m}Tc reconstructions. Subsequently, automatic healthy liver segmentation was performed on the ^{99m}Tc reconstruction using a threshold method previously assessed in a phantom study [60]. First, the maximum value in a smoothened version of the ^{99m}Tc image is determined (using a 3D Gaussian filter with width of 15 mm). Then, the original ^{99m}Tc image is thresholded to 40% of this maximum to produce the segmentation. **Figure 6.1** illustrates the manual and automatic segmentation methods within the [166]Ho radioembolization workflow.

Dosimetry

To estimate dose in healthy liver VOI, all [166]Ho images were converted from count density to MBq/ml using administered therapeutic activity, on the assumption that all activity was in the SPECT field of view. [166]Ho images were scaled considering only counts within the patient–body mask, automatically delineated on LDCT acquired together with SPECT. Since some patients received a partial liver treatment, [166]Ho pre-treatment images were scaled either using the partial treatment activity or the sum of the activities administered combining the complementary treatments (e.g. [166]Ho pre-treatment image targeting the whole liver of a patient who subsequently underwent two partial treatments was converted to MBq/ml based on the sum of the therapeutic activities received in the two treatment sessions).

For all VOIs, dose was computed as:

$$Dose[Gy] = 15.87 \left[\frac{mJ}{MBq} \right] \frac{Activity\ concentration_{VOI}\ [MBq/\text{ml}]}{VOI\ density[g/\text{ml}]}$$
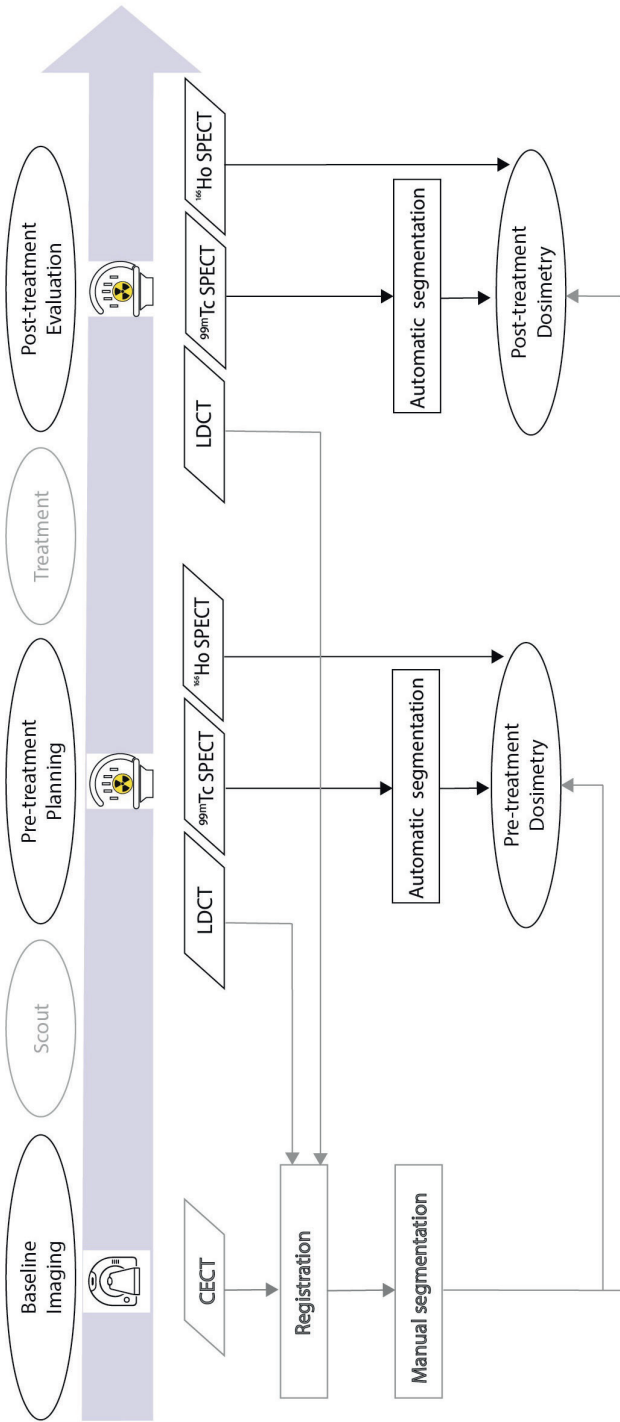
Figure 6.1

Schematic workflow representing the comparison between manual (left) and automatic (middle and right) segmentation with respect to the dosimetry purpose. The methods have been integrated with corresponding inputs and their timeline within the [166]Ho radioembolization workflow (upper blue arrow).

where 15.87 mJ/MBq represents the deposited energy due to β decay of 1 MBq ^{166}Ho. For the liver, a soft tissue density of 1.06 g/cm^3 was applied, assuming a homogenous organ density value, constant among patients. Since the mean penetration of β-emission of ^{166}Ho (2.5 mm) is small compared to voxel size (4.8 mm), all energy was assumed to be absorbed within the considered voxel. β-radiation accounts for 96% of the emitted energy, the other 4% of the energy is mostly emitted through γ-radiation. Because of the relatively large penetration distance of these γ and the inverse square law, absorbed radiation dose due to γ emissions was considered negligible in this study [27][9].

Segmentation evaluation

Healthy liver segmentations obtained using the manual and automatic approach were compared considering the resulting healthy liver volume difference and using two overlapping indices: the Sørensen–Dice coefficient (SDC) and the Hausdorff distance (HD). Since mean absorbed dose within the considered VOI was deemed as a more representative clinical metric, a Bland-Altman plot was used to compare resulting mean absorbed dose computed in the healthy liver manually and automatically segmented. Pearson's test was used to assess the correlation. As there is no current standard for dose-volume-histogram (DVH) reporting, minimum dose to 70% of the volume (D_{70}) and volume receiving at least 50 Gy (V_{50}) were used to compare the two segmentations methods [61]. In each comparative analysis, manual segmentation was considered as reference standard.

Hepatotoxicity was assessed at baseline and up to 12 months, every 3 months, according to the five point standardized scale of hepatotoxicity after radioembolization proposed by Braat *et al.*[62], and a score of ≥3 was considered significant. To assess the dose-hepatotoxicity relation for patients who underwent multiple treatments, mean absorbed doses in the healthy liver resulting from all the treatments received up to the time-point under investigation were summed. Dose-hepatotoxicity relation was investigated considering the worst grade hepatotoxicity during the follow-up and cumulative absorbed dose in the healthy liver received by that time-point.

To check the statistical difference between resulting doses computed on manual and automatic segmentation (null hypothesis is no difference), a two-sided paired T-test (at α = 0.05) was performed.

Results

For thirty-one subjects and a total of 66 procedures (29 pre- and 37 post-treatment), [166]Ho-^{99m}Tc dual-isotope acquisition was performed and included for segmentation assessment. One patient died within 3 months after [166]Ho-radioembolization because of a hypoglycemic crisis caused by an overproducing insulinoma. For another patient who underwent two radioembolization treatments, [166]Ho-^{99m}Tc dual-isotope acquisition was available for only one of the two treatments. These patients were included in the segmentation method comparison, but were excluded in the dose-hepatotoxicity correlation analysis. This resulted in a total of 29 subjects (30 treatments) assessed for hepatotoxicity during follow-up.

Manual segmentation and registration of CECT onto SPECT took a median (IQR) of 30 (15) minutes per patient, while automatic segmentation was instantaneous. Median (IQR) difference between healthy liver volume automatically segmented on the ^{99m}Tc images and manually segmented using the baseline CECT was 171 mL (341 mL), resulting in a statistically significant difference with a p-value < 0.05. Median (IQR) SDC and HD were 0.8 (0.12) and 8.6 cm (1.4 cm), respectively.

Mean ± standard deviation of health liver absorbed dose was 18 Gy ± 7 Gy and 20 Gy ± 8 Gy for manual and automatic segmentations, respectively. Bland-Altman plot and correlation between dose computed in the healthy liver manually and automatically segmented are shown in **Figure 6.2**. Mean difference ± coefficient of reproducibility between healthy liver absorbed doses using the automatic segmentation versus manual segmentation was 2 Gy ± 6 Gy (**Figure 6.2** panel **A**), resulting in limit of agreement of 8 Gy and -4 Gy. A statistically significant difference in mean healthy liver absorbed doses was found between the two methods (p-value < 0.05), with the dose computed by automated segmentation, on average, 2 Gy higher. The linear correlation between healthy liver dose computed using these two methods, assessed using Pearson's correlation coefficient (depicted in **Figure 6.2** panel **B**), was 0.92.

Mean ± standard deviation of D_{70} was 10 Gy ± 6 Gy and 11 Gy ± 6 Gy for manual and automatic segmentations, respectively. A Bland-Altman plot and the correlation between D_{70} is shown in Supplemental materials (Supplemental material **Figure 6.5**). Mean difference ± coefficient of reproducibility between D_{70} computed using the automatic segmentation versus manual segmentation was 1 Gy ± 4 Gy (Supplemental material **Figure 6.5** panel **A**). A statistically significant difference in D_{70} was found between the two methods, resulting in a mean 1 Gy difference for D_{70} by automated segmentation (p-value < 0.05). The linear correlation between D_{70} computed using these two methods, assessed using Pearson's correlation coefficient (depicted in Supplemental material **Figure 6.5** panel **B**), was 0.95.

6
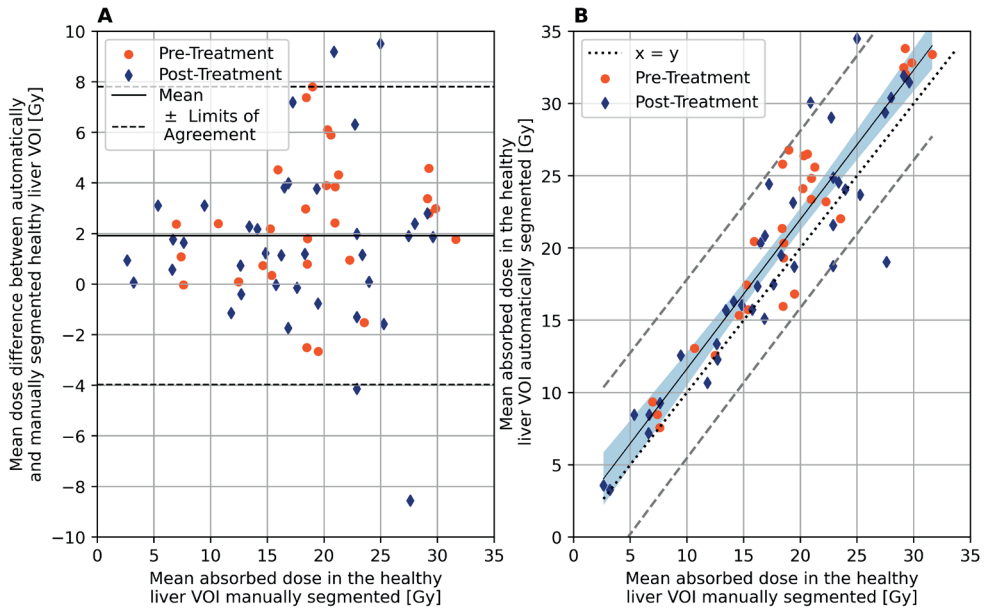
Figure 6.2

Panel **A**: Bland-Altman plot on the difference between mean absorbed dose; recovered mean dose in the healthy liver VOI automatically and manually segmented against mean absorbed dose in the healthy liver VOI manually segmented. Mean of the difference is depicted by the black solid line, while black dashed lines show limits of agreement. Panel **B**: linear correlation plot between manual and automatic segmentation of the healthy liver VOI with respect to the mean absorbed dose. The solid line depicts linear regression, while the dashed lines indicate the ± 95% confidence intervals. Dotted line represents the x = y line. [166]Ho pre-treatment images were scaled considering the therapeutic activity.

Mean ± standard deviation of V_{50} was 3 % ± 3 % and 4 % ± 5 % for manual and automatic segmentations, respectively. Bland-Altman plot and correlation between V_{50} computed in the healthy liver manually and automatically segmented are shown in Supplemental materials (Supplemental material **Figure 6.6**). Mean difference ± coefficient of reproducibility between V_{50} computed using the automatic segmentation versus manual segmentation was 1 % ± 5 % (Supplemental material **Figure 6.6** panel **A**). A statistically significant difference in V_{50} was found between the two methods (p-value < 0.05), resulting in a mean 1% difference for V_{50} by automated segmentation. The linear correlation between V_{50} computed using these two methods, assessed using Pearson's correlation coefficient (depicted in Supplemental material **Figure 6.6** panel **B**), was 0.82.

Analysis of hepatotoxicity during the 12 months follow-up after [166]Ho radioembolization, including the number of subjects per each toxicity grade, together with the corresponding

mean absorbed dose in the healthy liver manually and automatically segmented is reported in **Table 6.2**. Hepatotoxicity with a significant grade (≥ 3) was found in three patients graded 3, 4 and 5 with a corresponding mean absorbed dose in the manually (and automatically) segmented healthy liver of 19 Gy (20 Gy), 23 (22 Gy) and 30 Gy (32 Gy) respectively.

	0	**1**	**2**	**3**	**4**	**5**
Number of subjects	1	17	8	1	1	1
Dose Manual [Gy]	21	23±7	22±12	19	23	30
Dose Automatic [Gy]	30	24±11	21±9	20	22	32

Table 6.2
Worst hepatotoxicity grade scored according to Braat *et al.*[62]. Median ± IQR of the absorbed dose in the healthy liver is reported for manual and automatic segmentation.

No correlation was found between hepatotoxicity and healthy liver dose. A boxplot representing the healthy liver dose (manually and automatically segmented) per each toxicity grade is depicted in **Figure 6.3**.
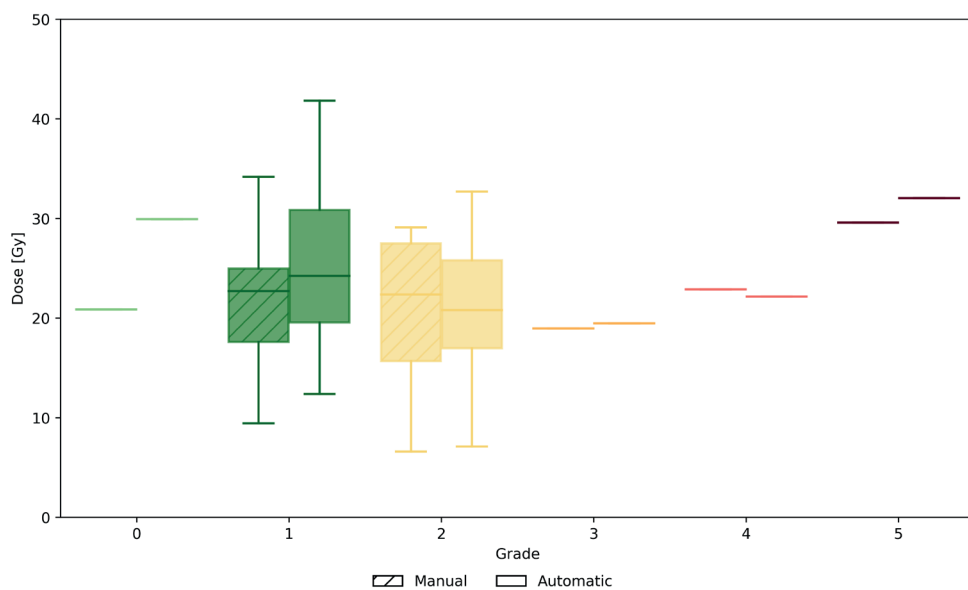
Figure 6.3
Boxplot representing the healthy liver dose (manually and automatically segmented) for the worst hepatotoxicity grade during follow-up.

Discussions

It is commonly accepted that optimal radioembolization requires accurate dosimetry [63], although dose-response and dose-toxicity values for ^{166}Ho radioembolization need further validation. However, multiple factors hamper dosimetry to become a routinely applied process, being perceived as complex and time-consuming. The ^{166}Ho-^{99m}Tc dual isotope protocol offers an alternative to manual segmentation and consequent registration of the healthy liver by automatizing this process to streamline dosimetry within the clinical practice. This paves the way to automatic pre-treatment planning for which a personalized treatment optimization may be obtained by considering mainly the healthy liver. The ^{166}Ho-^{99m}Tc dual isotope protocol can also facilitate rapid post-treatment evaluation providing insights on dose delivered to the healthy liver and eventually predicting whether significant hepatotoxicity might be encountered, especially for neuroendocrine tumor patients, for whom long term toxicity is feared [64]. The possibility to optimize radioembolization treatment considering the healthy liver dose and corresponding toxicity as limiting factor in order to deliver the maximum tolerable absorbed dose to healthy liver tissue was suggested by Chiesa *et al.* [14] who investigated this approach for hepatocellular carcinoma patients treated with yttrium-90 glass microspheres.

However, multi-compartment dosimetry relies on an adequate balance, considering healthy liver dose, but also tumor dose [35]. The possibility to perform tumor dose assessment using the (pre- or post-treatment) SPECT image is again subject to manual segmentation and registration of lesions by physicians. Thus, as for healthy liver, dosimetry would benefit from automatic tumor segmentation. Despite ^{166}Ho uptake occurring primarily in tumors (for hypervascular lesions), a minor amount of ^{166}Ho is distributed in healthy liver tissue. For this reason, a robust thresholding approach to segment tumors based on the ^{166}Ho image is challenging to implement. The use of the ^{99m}Tc image derived from the ^{166}Ho-^{99m}Tc dual-isotope protocol for automatic tumors segmentation would rely on automatic identification of cold spots (considered as tumors due to the lack of Kupffer cells present in parenchyma). This approach presents several challenges since the limited SPECT resolution would play a bigger role in identification of small volumes of interest. The resolution will limit detection of small tumors, whilst miss identification of cold spots as tumors could potentially be benign lesions (e.g. liver cysts). Additionally, to perform automatic tumor dosimetry, the perfused volume during treatment should be identified. While the ^{166}Ho image itself provides an indication of the perfused volume, this task is not straightforward (especially for lobar treatments) and brings a further challenge to automatic tumor dosimetry using the ^{166}Ho-^{99m}Tc dual isotope protocol.

In this study, feasibility of automatic healthy liver segmentation using ^{99m}Tc images deriving from the ^{166}Ho-^{99m}Tc dual isotope protocol was demonstrated on patient data.

A straightforward benefit of the suggested protocol is the time saved to perform healthy liver segmentation (~ 30 minutes per patient when using the manual segmentation versus instantaneous with this [166]Ho-^{99m}Tc dual isotope protocol), together with the avoidance of inter-observer variability [59].

The mean absorbed dose difference between automatically and manually segmented healthy liver is limited to 2 Gy, which, even though statistically significant, was considered acceptable for healthy liver assessment by experienced nuclear medicine physicians [27]. The same considerations apply to the D_{70} and V_{50} used to assess the DVH. Despite overlapping indices like SDC and HD are easy to implement and useful summary measures of spatial overlap, they poorly outline the considerations assessing the segmentation methods (manual versus automatic) for the purpose of [166]Ho radioembolization dosimetry. An explanatory example showing how overlapping indices might lead to partial conclusions on the resulting dosimetry is depicted in **Figure 6.4**.

The hepatotoxicity analysis showed no correlation between healthy liver dose and toxicity grades. This is in line with previous results by Ebbers *et al.* [65] in which no significant relationship between absorbed dose in treated healthy liver and biochemical toxicity was found when assessing a NET patient population treated with yttrium-90 glass microspheres.

In this study, all patients presented a mean healthy liver absorbed dose (manually or automatically segmented) < 35 Gy (range 3 Gy – 32 Gy), below the reported acceptable healthy liver dose limits reported for patients with different tumor types treated with radioembolization [66][67][68]. However, due to the limited REILD occurrence within this study (1 case) and low incidence of significant hepatotoxicity (1 case), no strong conclusion can be drawn on maximum tolerable healthy liver dose for this patient population. Further investigations on more dedicated data should be performed to determine tolerable dose limits. Additionally, the dependence of this dose limit on patient characteristics (i.e. underlying liver disease, previous treatments, lesion types) prevents a generally applicable limit for all patients.

Several limitations apply to this study. Primarily, the healthy liver segmentation manually performed on baseline anatomical image and rigidly registered on SPECT is known to be far from ideal (as shown in **Figure 6.4**, panels **A**-**C**), thus the reference standard ('ground truth') to which the automatic segmentation outcome was compared is limited. Also the automatic segmentation method, which relies on a fixed threshold for all patients, can lead to suboptimal segmentation for some patients, hampering the consequent personalized dosimetry. [99m]Tc stannous-phytate accumulates in Kupffer cells only, representing healthy liver, however its uptake is not homogenous and does not provide any information regarding regional liver function. An intrinsic limitation of [166]Ho-^{99m}Tc dual isotope approach is the limited resolution of SPECT, which does not allow for the identification of small lesions, widely present in NET patients.

6
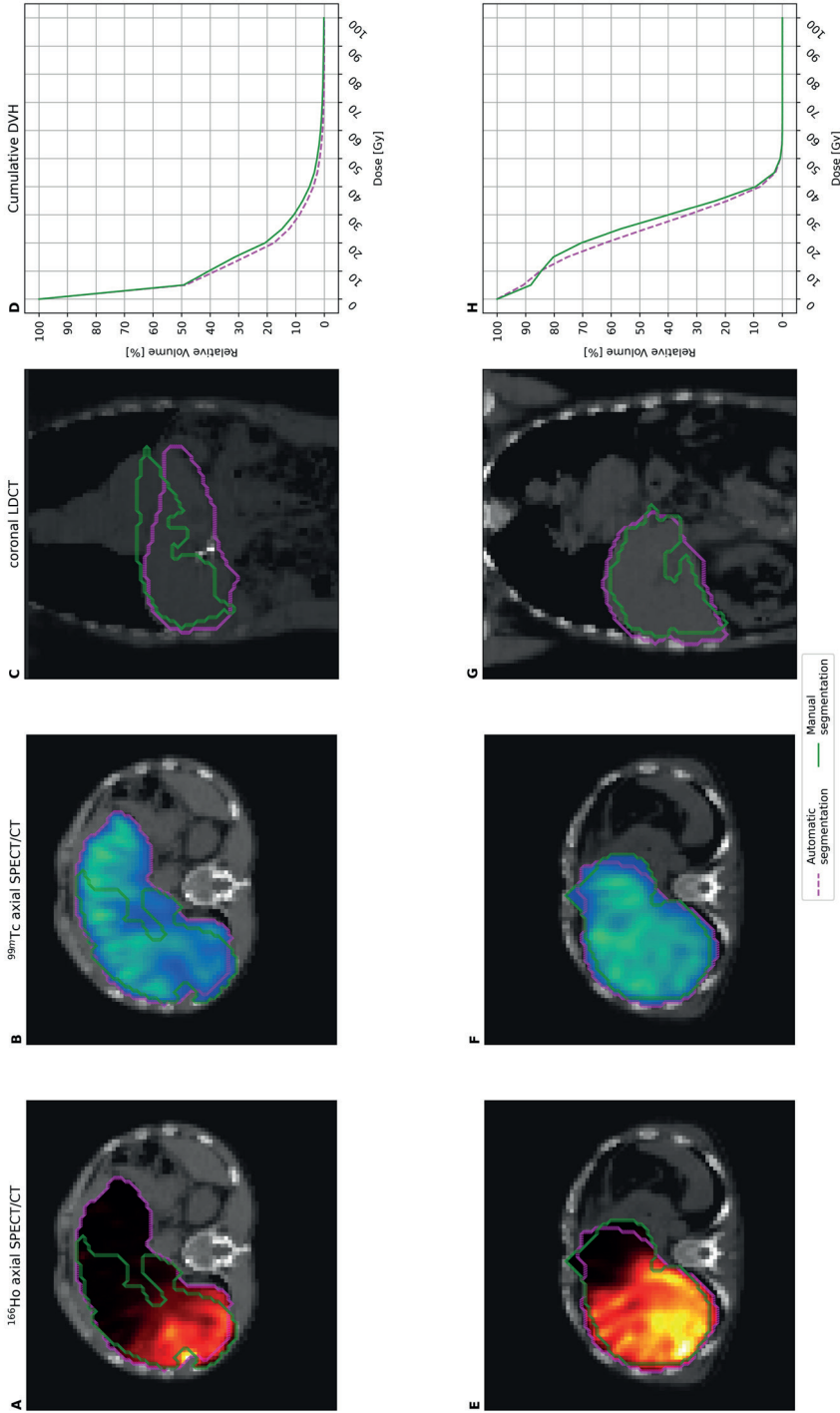
Figure 6.4

Examples of automatic segmentation outcome. **A-D**. 56 years male subject treated with 3850 MBq of ^{166}Ho microspheres in the right liver. **E-H**. 65 years male subject treated with 4982 MBq of ^{166}Ho microspheres in the right liver. Panels **A** and **E**, and **B** and **F**, show the axial view of ^{166}Ho and ^{99m}Tc SPECT/CT respectively, while panels **C** and **G** show the coronal view of the LDCT acquired with the SPECT. Manual (solid green) and automatic (dashed magenta) segmentation are depicted. Upper panels (**A**, **B**, **C**, Sørensen Dice Coefficient = SDC = 0.62), show a clear discrepancy between segmentations, which is due to non-rigid deformation of liver because of breathing. Segmentations are quite comparable in the bottom panels (**E**, **F**, **G**, SDC = 0.84). Panels **D** and **H** show the resulting cumulative dose-volume histogram (DVH). Despite the segmentation differences, the corresponding dose difference is below 2 Gy.

Additionally, the definition of a clear dose-hepatotoxicity relation is hampered by various limitations. Firstly, the patient baseline condition is of influence on the development of hepatotoxicity, and the adopted scale scores the hepatotoxicity relatively to the baseline. Secondly, the limited population size (and number of events) limits the applicability of robust statistic models. Thirdly, hepatotoxicity following radioembolization is related to multiple risk factors such as previous liver directed treatments or intra-arterial therapies, tumor burden, toxicity of concomitant medications [62].

A clinical validation study of the [166]Ho-^{99m}Tc dual isotope protocol, including more patients, should be performed to confirm the presented promising data and prove its ease in the clinical workflow, due to rapid automated image segmentation without image misregistration. The thresholding approach used for the automatic segmentation would benefit from additional data to determine its robustness. This may further pave the way to rapid implementation of personalized dosimetry in clinical routine for radioembolization.

Conclusion

[166]Ho-^{99m}Tc dual isotope imaging allows automatic segmentation of the healthy liver tissue using a thresholding method without compromising assessment of healthy liver absorbed dose. [166]Ho-^{99m}Tc dual-isotope imaging paves the way for automated partition model-based activity calculation for [166]Ho radioembolization, feasible in clinical practice. In addition, this will accelerate treatment planning and post-treatment evaluation.

6

Supplemental material
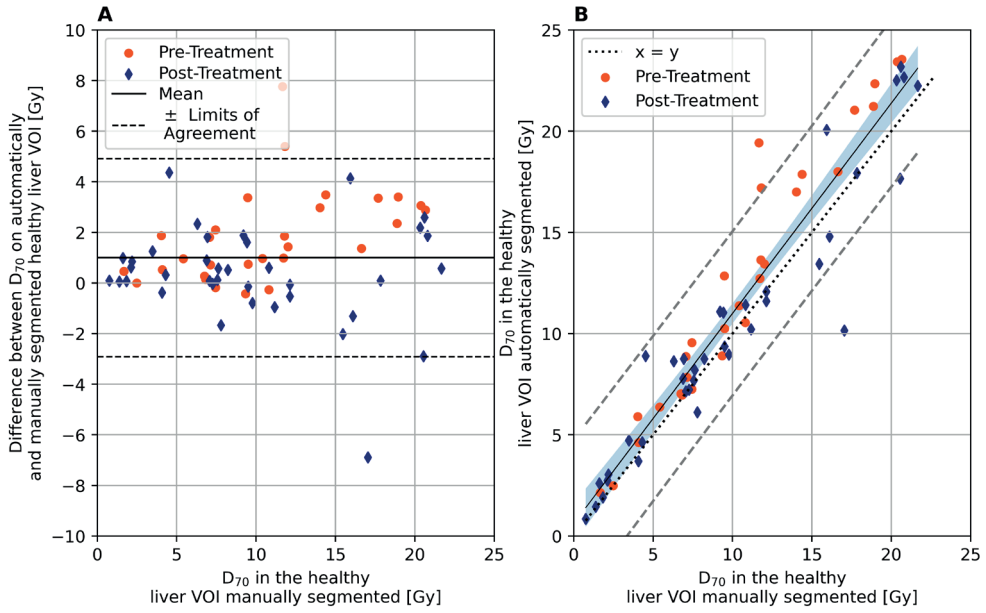
Figure 6.5

Panel **A**: Bland-Altman plot on difference between D_{70}; D_{70} in the healthy liver VOI automatically and manually segmented against D_{70} in the healthy liver VOI manually segmented. Mean of difference is depicted by the black solid line, while black dashed lines define ± limits of agreement. Panel **B**: linear correlation plot between manual and automatic segmentation of the healthy liver VOI with respect to the D_{70}. The solid line depicts linear regression, while the dashed lines indicate the ± 95% confidence intervals. Dotted line represents the x = y line. [166]Ho pre-treatment images were scaled considering the therapeutic activity.
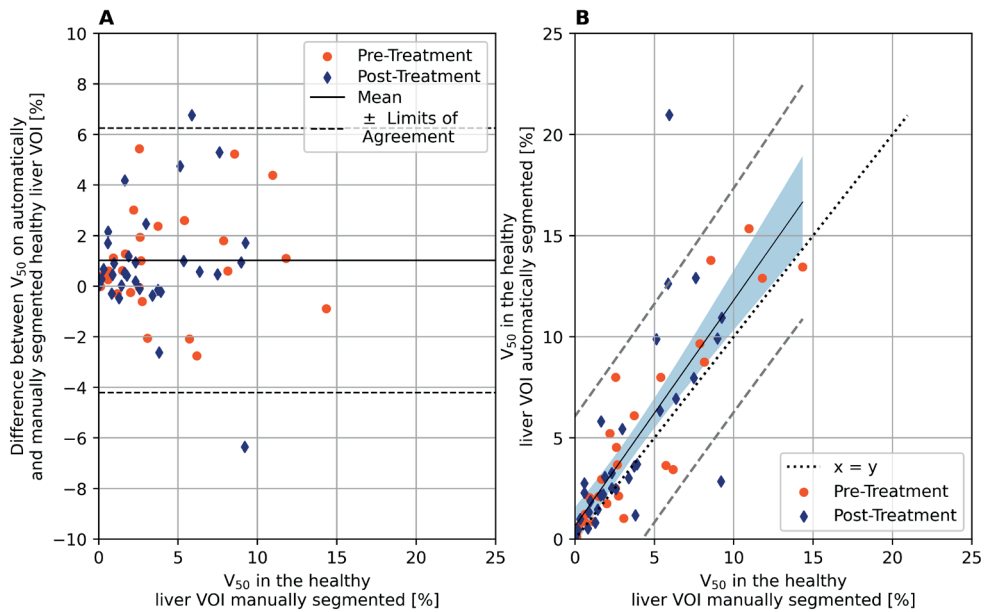
Figure 6.6

Panel **A**: Bland-Altman plot on difference between V_{50}; V_{50} in the healthy liver VOI automatically and manually segmented against V_{50} in the healthy liver VOI manually segmented. Mean of difference is depicted by the black solid line, while black dashed lines define ± limits of agreement. Panel **B**: linear correlation plot between manual and automatic segmentation of the healthy liver VOI with respect to the V_{50}. The solid line depicts linear regression, while the dashed lines indicate the ± 95% confidence intervals. Dotted line represents the x = y line. [166]Ho pre-treatment images were scaled considering the therapeutic activity.

6

CHAPTER 7

Lung dose measured on ^{90}Yttrium PET/CT and incidence of radiation pneumonitis

Abstract

Background: Radiation pneumonitis is a rare but possibly fatal side effect of Yttrium-90 (^{90}Y) radioembolization. It may occur 1 to 6 months after therapy, in case a significant part of the ^{90}Y microspheres shunt to the lungs. In current clinical practice, a predicted value of lung dose greater than 30Gy is considered a criterion to exclude patients from treatment. However, contrasting findings regarding the occurrence of radiation pneumonitis and lung dose were previously reported in literature. In this study, the relationship between the lung dose value and the eventual occurrence of radiation pneumonitis after ^{90}Y radioembolization was investigated.

Methods: A total of 317 ^{90}Y liver radioembolization procedures performed during an 8-years period (Feb.2012–Sep.2020) were retrospectively analyzed. Predicted lung mean dose using ^{99m}Tc-MAA planar scintigraphy (LMD_{MAA}) acquired during the planning phase and left lung mean dose (LMD_{Y-90}) using the ^{90}Y PET/CT acquired after the treatment were calculated. For the lung dose computation, it was chosen to use the left lung as representative lung volume, to compensate for the scatter from the liver moving in the cranial-caudal direction due to breathing and mainly affecting the right lung.

Results: Two hundred and seventy-two patients underwent ^{90}Y procedures, of which 63% performed with glass microspheres and 37% with resin microspheres. Median injected activity was 1974MBq (range: 242-9538MBq). Median LMD_{MAA} was 3.5Gy (range: 0.2–89.0Gy). For 14 procedures LMD_{MAA} was >30Gy. Median LMD_{Y-90} was 1Gy (range: 0.0–22.1Gy). No patients had a LMD_{Y-90} >30Gy. Of the three patients with a LMD_{Y-90} >12Gy, two patients (LMD_{Y-90} = 22.1Gy, LMD_{MAA} = 89Gy and LMD_{Y-90} = 17.7Gy, LMD_{MAA} = 34.1Gy, respectively) developed radiation pneumonitis and consequently died. A third patient with a LMD_{Y-90} equal to 18.4Gy (LMD_{MAA} = 29.1Gy) died 2 months after treatment, before imaging evaluation, due to progressive disease.

Conclusion: The occurrence of radiation pneumonitis as a consequence of lung shunt following ^{90}Y radioembolization is rare (<1 %). No radiation pneumonitis developed in cases with a measured LMD_{Y-90} lower than 12Gy.

Background

Radioembolization is a well-established treatment for primary and metastatic liver malignancies [69]. It is defined as the injection via percutaneous trans-arterial techniques [70] of embolic particles (diameter size range: 20 – 60μm) loaded with yttrium-90 (^{90}Y) or holmium-166 ([166]Ho). As hepatic tumors are preferentially fed by the blood supply from the hepatic artery, radioembolization preferentially deposits radioactive microspheres in the peritumoral and intratumoral arterial vasculature through the hepatic artery, relatively sparing normal liver parenchyma [71]. Three devices are commercially available: glass ^{90}Y microspheres (TheraSphere®; Boston Scientific Corporation, Marlborough, Massachusetts, US), resin ^{90}Y microspheres (SIR-spheres®; SIRTeX Medical Limited, North Sydney, NSW, Australia) and poly-L-lactic acid [166]Ho microspheres (QuiremSpheres™; Quirem Medical B.V., The Netherlands). Since microspheres can pass through tumor-associated arteriovenous shunts and lodge in the pulmonary vasculature, if this pulmonary deposition is significant, a dose-dependent radiation-induced pneumonitis may ensue. Therefore, presence of significant hepatopulmonary shunting is a relative contraindication for radioembolization. The current approach to radioembolization with respect to radiation pneumonitis is mainly driven by two seminal publications[72]·[73] that have strongly influenced the guidance on lung dose limits following radioembolization. Based on clinical evidence from these studies, lung dose limit of 30Gy was recommended for single radioembolization treatment [74] and adopted in the instructions for use manual (IFU) of these devices. For this reason, the assessment of the lung shunt fraction (LSF), which is a prediction of the eventual lung dose following the radioembolization treatment, is paramount prior to the administration of the radioactive particles.

For ^{90}Y, this prediction is performed using 99m-technetium-macroaggregated albumin (^{99m}Tc-MAA). Despite being the current clinical practice, ^{99m}Tc-MAA is poor in predicting the dose to the lungs, especially when computing the lung shunt fraction (LSF_{MAA}), and consequently the predicted lung mean dose (LMD_{MAA}) using planar scintigraphy. SPECT/CT imaging technique can improve the LSF computation [75]. However, discrepancies between ^{90}Y and ^{99m}Tc-MAA particles reduce its predictive value [76]·[77].

The aim of this study is to assess the occurrence of radiation pneumonitis after ^{90}Y liver radioembolization and perform lung dosimetry on ^{90}Y-PET/CT to evaluate the currently assumed lung dose restriction of <30Gy. Although multiple studies on lung dose following ^{90}Y radioembolization are reported in literature, they all focus on the ^{99m}Tc-MAA based lung dose estimate during the pre-treatment phase. Conversely, this study retrospectively

quantified the actual dose received by the lungs following ^{90}Y radioembolization, exploiting the potential of post-treatment PET/CT [78] and ^{90}Y accurate dosimetry [79]. This would provide a better insight into the lung dose following ^{90}Y radioembolization and the related occurrence of radiation pneumonitis.

Materials and methods

This single center, retrospective analysis of all patients treated with ^{90}Y-radioembolization between February 2012 and September 2020 was approved by the ethical research committee and the need for informed consent was waived. Prior to radioembolization treatment, patient eligibility for treatment was assessed by ^{99m}Tc-MAA injection in the hepatic artery, to assess intrahepatic distribution and potential extrahepatic deposition of activity (including lung shunting). After ^{99m}Tc-MAA injection, a planar gamma camera scintigraphy (for LSF_{MAA} computation) and a SPECT/CT (to visually assess extrahepatic depositions) were acquired. To assess the treatment outcome, a post-treatment ^{90}Y-PET/CT was obtained the same day or the day after treatment. Lung mean dose after ^{90}Y radioembolization was assessed using the post-treatment ^{90}Y PET/CT.

^{90}Y-PET/CT protocol

Images were acquired on a Biograph mCT time-of-flight PET/CT scanner or on a Biograph Vision 600 time-of-flight PET/CT scanner (both Siemens Medical Solutions USA, Inc.), with a 40- and 64-slice CT scanner, respectively. To reconstruct the images, an iterative algorithm including a model-based scatter correction method, which encompasses a point spread function model of the detector response together with time-of-flight information, was used. To correct for attenuation, low-dose CT acquired right after the PET was employed. Both PET scanners and reconstruction protocol were validated for ^{90}Y quantitative imaging [80].

^{99m}Tc-MAA based lung mean dose predicted

To determine patient's eligibility, lung mean dose predicted using ^{99m}Tc-MAA (LMD_{MAA}) was calculated as follows:

$$LMD_{MAA} = \frac{Activity_{prescribed}\,[GBq] \times LSF_{MAA} \times 50\,[Gy \times kg/GBq]}{Lung\ mass\,[kg]}$$

Where lung mass is assumed to be equal to 1 kg and 50 [Gy*kg/GBq] is the standard conversion factor for [90]Y. LSF_{MAA} is the lung shunt fraction based on the ^{99m}Tc-MAA planar image and was computed as follows:

$$LMF_{MAA} = \frac{Count_{Lung}}{Count_{Lung} + Count_{Liver}} \times 100\%$$

The counts were computed using the geometric mean following standard clinical practice [30]. Lungs and liver were delineated on the planar scintigraphy by the imaging technicians.

[90]Y PET-based lung mean dose

To assess the mean absorbed dose in the lungs after the treatment, lungs masks were automatically segmented on the CTs corresponding to the PET scans used for the dosimetric purposes, using a freely available U-net, extracting right-left lung separately[81]. All masks were visually checked to ensure a correct segmentation. Since right lung was affected by scatter from the liver moving in the cranial-caudal direction due to breathing (see **Figure 7.1**), only the left lung was considered, as representative for the computation of the mean lung dose. [90]Y PET based left lung mean dose (LMD_{Y-90}) was computed as follows:

$$LMD_{Y-90} = \frac{Mean\ Activity\ Concentration_{LEFT\ LUNG} \left[\frac{Bq}{mL}\right] \times 5 \times 10^{-8}\ [J*s]}{Lung\ density\ [kg/cm^3]}$$

Mean activity concentration in the left lung was computed as the mean of the voxel value [Bq/mL] within the left lung mask. Lung density was assumed to be $2.6e^{-4}$ [kg/mm³][53], while $5e^{-8}$ [J*s] represents the deposited energy due to the β decay of 1 Bq of injected ^{90}Y activity[82]. Mean activity concentration was corrected for ^{90}Y decay considering the time difference between the activity administration time and the scanning time. Three commonly applied assumptions were adapted for this study. First, the maximal range for ^{90}Y betas in tissue is 1.2 cm, which is in the same order of magnitude as the resolution of ^{90}Y PET, thus it was assumed the total energy is deposited within the voxel of origin[35]. Second, that ^{90}Y distributes uniformly in case of lung shunting, and third, lung density was the same for all patients.

7
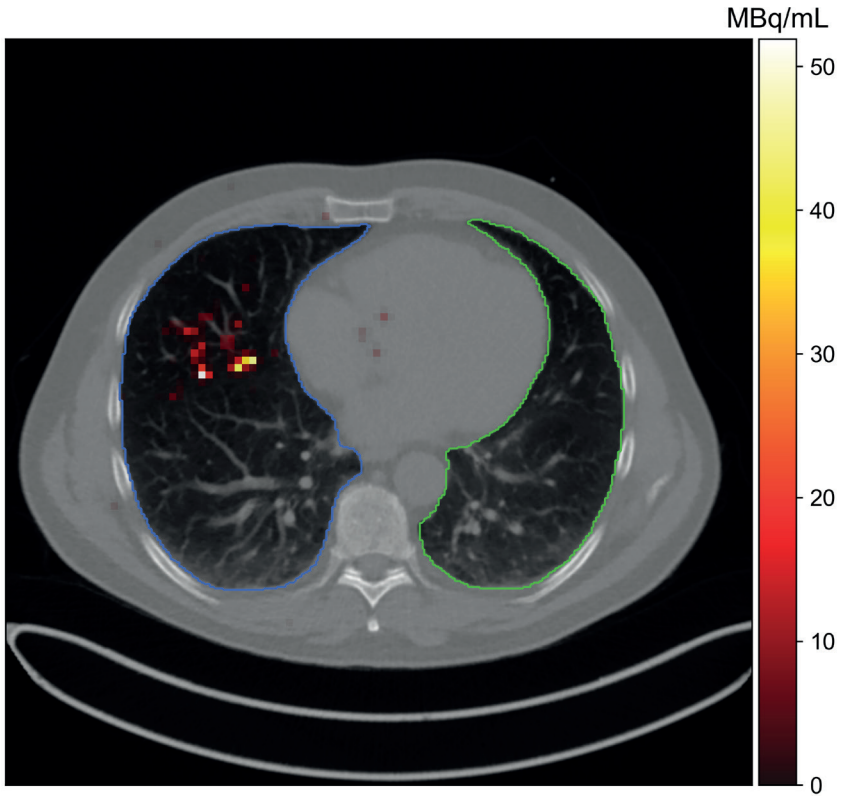
Figure 7.1

Post-treatment ^{90}Y PET/CT scan of 47-y-old man diagnosed with colorectal cancer. LMD considering both lobes was 61 Gy. ^{90}Y PET image shows activity in right lung (blue contour) due to liver motion in craniocaudal direction and rim field-of-view artifact and leading to right LMD of 100 Gy, which was main contributor to LMD. Left LMD (computed within green contour) was 3 Gy.

^{90}Y PET-based lung shunt fraction

Since planar based LSF_{MAA} is a poor predictor for the actual lung shunting, in this work lung shunt fraction measured using ^{90}Y PET/CT (LSF_{Y-90}) was used as metric to evaluate differences in biology.

To assess differences among tumor type, LSF_{Y-90} was computed. LSF_{Y-90} was defined as the ratio between the activity in the lungs and the total activity administered, as follow:

$$LSF_{Y\text{-}90} = \frac{Mean\ Activity\ Concentration_{LUNGS}\ \left[\frac{Bq}{mL}\right]\ x\ Lung\ volume\ [mL]}{Activity_{prescribed}\ [Bq]}\ x\ 100\%$$

As for the $LMD_{Y\text{-}90}$, mean activity concentration in the lungs was computed as the mean of the voxel value [Bq/mL] within both lungs mask. Lungs volume was assumed to be the same among all subjects, considering a lung mass of 1 kg and a lung density value of $2.6e^{-4}$ [kg/mL], previously assumed.

Statistical analysis

Statistical variables under investigation to characterize radiation pneumonitis were LMD_{MAA} and $LMD_{Y\text{-}90}$. When assessing the eventual difference among tumor types or, in case of HCC patients, between the presence or not of portal hypertension and thrombus, $LSF_{Y\text{-}90}$ was considered, to take into account the different activity delivered. The normality of their distribution was assessed visually and by mean of QQ plot. If variables were not normally distributed, non-parametric test were used for further analysis.

Mann–Whitney U-test with alpha significance level equal to 0.05 was used in case of HCC patients to assess whether the occurrence of thrombus or portal hypertension caused statistically significant left lung mean dose.

Kruskal-Wallis H-test with alpha significance level of 0.05 was used to determine whether statistical difference was found between different tumor types.

Results

Patients' population

Patients and treatments characteristics are summarized in **Table 7.1**. The institutional review board approved this study and waived the need for informed consent for this retrospective study. There were 170 men and 102 women for a total of 317 ^{90}Y radioembolization procedures (mean procedures per patient 1.17 range 1-5). Most of the patients were treated for liver metastases of various origins, while 25% had HCC. Glass microspheres were used for 200 treatments while the remaining 117 procedures were performed with resin microspheres. Median administered activity per procedure was 2278 MBq (range: 277 - 9636) and 1877 MBq (516 – 3245) for glass and resin microspheres respectively. Median volume within the PET field-of-view was 1713 cc (392 – 7851) and 733 cc (80-3792) for both lungs and left lung, respectively.

7

Characteristic	N (%) or median (range)
Patients	272
Procedures	317
Sex	
Male (%)	170 (62.5)
Female (%)	102 (37.5)
Mean Age (range)	64.56 (17 - 90)
Spheres Type	
Glass (%)	200 (63)
Resin (%)	117 (37)
Median Administered Activity [MBq] (range)	
Glass	2278 (277 – 9636)
Resin	1877 (516 – 3245)
Mean number of Y90 sessions (range)	1.17 (1 – 5)
Tumor Types N (%)	
CRC (colorectal cancer)	104 (38%)
HCC (hepatocellular carcinoma)	68 (25%)
NET (neuroendocrine tumor)	45 (16%)
ICC (cholangiocellular carcinoma)	21 (8%)
Others	34 (13%)
Thrombus	
Segmental right portal vein	9
Lobar left portal vein	4
Segmental R portal vein+lobar L portal vein	1
TT main portal vein	2
TT right hepatic vein	1
Portal Hypertension	33
Planar MAA LSF (%)	
Mean (range)	5.73 (0.49 – 50.44)
Median (IQR)	3. 87 (4.60)
Number of cases > 20%	11
^{90}Y LSF (%)	
Mean (range)	5.90 (0.27 – 39.02)
Median (IQR)	4.13 (5.28)
Number of cases > 20%	7
^{99m}Tc based lung mean dose prediction (Gy)	
Mean (range)	6.93 (0.17 – 89.03)
Median (IQR)	3. 52 (6.48)
Number of cases > 30Gy	14
^{90}Y PET based left lung dose (Gy)	
Mean (range)	1.59 (0.02 – 22.14)
Median (IQR)	0.95 (1.16)
Number of cases > 12Gy	3

Table 7.1 Continued

Characteristic	N (%) or median (range)
Total Lung volume (cc)	
Mean (range)	1827 (392 – 7851)
Median (IQR)	1713 (944)
Left Lung volume (cc)	
Mean (range)	795 (80 - 3792)
Median (IQR)	733 (465)

Table 7.1
Baseline and treatment characteristics. Qualitative data are number; continuous data are mean and range or median and interquartile range.

Data analysis

Median LMD_{MAA} was 3.5Gy (range: 0.2 – 89.0). For 14 patients planar LMD_{MAA} was greater than 30Gy, above which ^{90}Y radioembolization is contraindicated[83]. Nonetheless, after clinical considerations by the treating physicians, these patients underwent ^{90}Y radioembolization treatment.

Median post-treatment LMD_{Y-90} was 1.0 Gy (range 0.0 – 22.1), with three cases above 12 Gy. No cases of LMD_{Y-90} above 30Gy were reported.

Median LSF_{Y-90} was 4.13% (range 0.27 – 39.02). Overall, according to Kruskal-Wallis H-test, no statistical significant difference was reported among tumor type (p-value = 0.1). However, pairwise comparison among tumor type returned a statistical significant difference between NET patients compared to CRC, HCC and "others" patients, with a p-value of 0.008, 0.010 and 0.022 respectively. P-values for statistical significance difference resulting from the pairwise comparison among tumor types in term of LSF_{Y-90} are reported in **Table 7.2**.

	LSF_{Y-90}				
Type	Cholangiocellular carcinoma	Colorectal cancer	HCC	Neuroendocrine tumor	Others
Cholangiocellular carcinoma	-	0.5	0.5	0.06	0.5
Colorectal cancer		-	0.4	0.008*	0.5
HCC			-	0.01*	0.4
Neuroendocrine tumor				-	0.02*
Others					-

Table 7.2
Matrix of the statistical significance of the differences between the tumor types in terms of LSF_{Y-90}. *Statistically significant (P < 0.05).

Boxplot depicting the LSF$_{Y-90}$ per tumor type is shown in **Figure 7.2**.
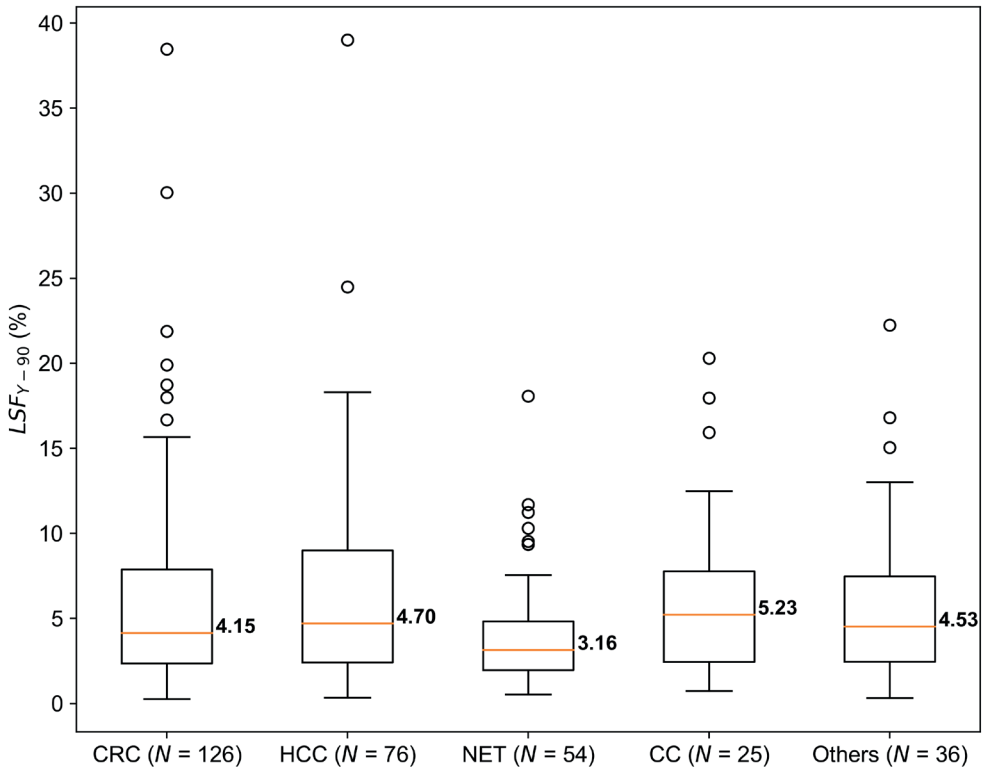
Figure 7.2

Box plots depicting LSF$_{Y-90}$, together with corresponding median, divided by tumor type. Statistically significant difference was reported between neuroendocrine tumor patients and colorectal cancer patients ($P=0.008$), between neuroendocrine tumor and HCC patients ($P=0.010$), and between neuroendocrine tumor and patients in group "others" ($P=0.022$). CC = cholangiocellular carcinoma; CRC = colorectal cancer; NET = neuroendocrine tumor.

LMD$_{Y-90}$ as function of LMD$_{MAA}$ is reported in **Figure 7.3**. This suggested that radiation pneumonitis did not occur among subjects with a LMD$_{Y-90}$ below 12Gy. Based on this empirical value and the 30Gy limit for LMD$_{MAA,}$ the number of true negative, true positive, false negative and false positive was reported in **Figure 7.3**.
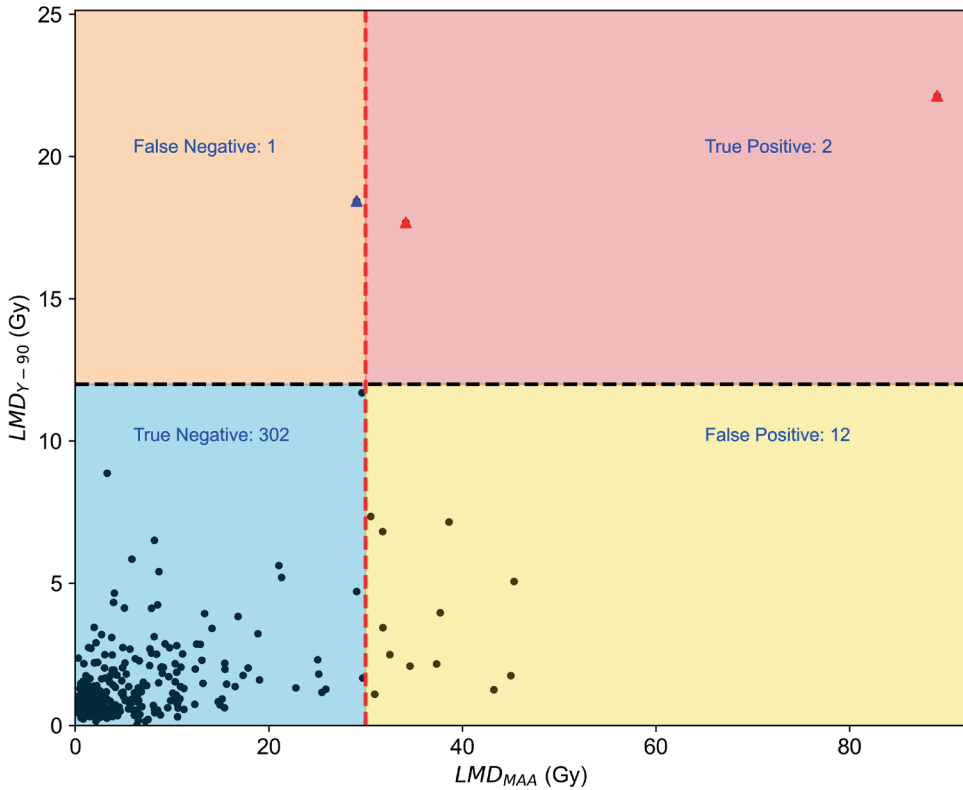
Figure 7.3

Distribution of LMD_{Y-90} as function of corresponding LMD_{MAA}. On the basis of limit of 30 Gy for estimate of absorbed radiation dose to lungs during pre-treatment phase and 12 Gy for LMD_{Y-90}, below which no radiation pneumonitis cases were reported, subjects were divided into 4 quadrants: true-positive, false-positive, true-negative, and false-negative. According to chosen limits, 12 false-positives were detected. True-positive (red triangles) corresponds to 2 patients who developed radiation pneumonitis, whereas false-negative (blue triangle) corresponds to patient who died of progressive disease before follow-up.

Radiation pneumonitis occurrence

Radiation pneumonitis did not occur among all the subjects with a LMD_{Y-90} below 12Gy. Radiation pneumonitis occurred in two patients, both diagnosed with HCC and treated with glass microspheres. The first patient presented the highest LMD_{Y-90} (22.1Gy) among the subjects considered in this study. The patient had no thrombus neither portal hypertension. During the pre-treatment work-up LMD_{MAA} was 89.0Gy (LSF_{MAA} = 23%), SPECT/CT showed no evidence of extrahepatic depositions in the upper abdomen. Total administered

activity was 7775 MBq. The second patient diagnosed had a LMD_{Y-90} of 17.7Gy, in the presence of both portal vein tumor thrombosis and portal hypertension. LMD_{MAA} was 34.1Gy (LSF_{MAA} = 50%), SPECT/CT showed no evidence of extrahepatic depositions in the upper abdomen. Total administered activity was 1300 MBq. Details of this case have been previously described by Alsultan et al.[78].

Another subject, with LMD_{Y-90} of 18.4Gy (LMD_{MAA} = 29.1Gy, LSF_{MAA} = 19%) died 2 months after treatment, before evaluation scan, due to progressive disease.

Discussions

The limit of 30Gy as maximum absorbed dose to the lungs for single radioembolization treatment was based on clinical evidence from two seminal publications[72][73] that have strongly influenced the guidance on lung dose limits following radioembolization. In this observational study, it has been shown that no patients with LMD_{Y-90} below 12Gy developed any lung-dose related side effect. Out of the 14 patients who had a LMD_{MAA} above 30Gy, two of them developed radiation pneumonitis. However, the twelve other patients with LMD_{MAA} > 30Gy did not developed any lung-dose related side effect, remarking the limitation of using ^{99m}Tc-MAA planar scintigraphy in predicting ^{90}Y lung shunt.

Radiation pneumonitis is a rare but potentially fatal side effect of radioembolization. During the past years different works, summarized by Cremonesi et al.[84], have been published reporting the lung-dose related side effect of ^{90}Y radioembolization, trying to provide a better insight in defining the upper dose limit to the lungs. However, although they all used the same approach to compute the lung dose, namely the ^{99m}Tc-MAA scintigraphy acquired prior to the ^{90}Y treatment and then multiplying the resulting LSF_{MAA} by the administered activity to estimate the LMD, different values for the lung dose above which radiation pneumonitis occurred were found (ranging between 10Gy and 56Gy). In line with the 12 false positive reported in this study (see **Figure 7.3**), Salem et al. [56], reported of 58 patients treated with cumulative and/or single treatment lung doses based on LSF_{MAA} derived calculations exceeding 30Gy who did not develop any radiation pneumonitis or lung toxicities. These findings further underline how ^{99m}Tc particle overestimates the actual lung shunt. On the contrary, Leung et al.[72] already reported radiation pneumonitis occurrence in three patients with a predicted lung mean dose lower than 30Gy. It is important to note, though, that the absorbed doses taken from the literature were derived without including the attenuation correction and thus should be rescaled by an average factor of 0.6[85]. For this reason, a straight comparison with the results presented in this study is difficult. In addition, in this

study, LMD_{Y-90} was computed on the post-treatment ^{90}Y PET and considering only the left lung as representative for the lungs volume. In this study, the same difficulties were found in determining a unique threshold for the ^{99m}Tc-MAA based LMD estimate values to avoid radiation pneumonitis, confirming an issue well documented in literature. As an example, in a multicenter study, Braat et al.[56] reported a patient with LSF_{MAA} of 3% who developed radiation pneumonitis, while another patient with the highest LSF_{MAA}, equal to 33%, did not develop a radiation pneumonitis. These contradictory findings in literature underline the limits of planar ^{99m}Tc-MAA lung shunt fraction, and consequently lung dose estimate, as predictive particle for assessing ^{90}Y distribution[77], stressing the need for a more reliable and robust method or particle. In the recent years, some alternatives to ^{99m}Tc-MAA were suggested. Kunnen et al.[86] demonstrated, in a phantom study, that bremsstrahlung SPECT/CT, reconstructed with a Monte Carlo algorithm, can estimate the lung shunt fraction for a ^{90}Y pre-treatment procedure using a theoretically safe ^{90}Y activity as low as 70 MBq. ^{166}Ho scout microspheres (250 MBq, QuiremScout™; Quirem Medical B.V., The Netherlands), already used as scout particles prior to ^{166}Ho radioembolization, were proposed as surrogate of ^{90}Y to determine patients' eligibility, thanks to its imaging possibility [48].

Both patients who developed radiation pneumonitis in this study had HCC. Both cirrhosis and HCC have been associated with increased arterio-venous shunting into the lungs, potentially causing increased lung doses[87]. However, significant differences were observed in LSF_{Y-90} only for HCC patients when compared to NET diagnosed subjects (**Figure 7.2**). In the subgroup of HCC patients only, the presence of either a thrombus or portal hypertension did not play a statistically significant role in LSF_{Y-90}, suggesting that these variables might be negligible when assessing the lung-dose related side effect of ^{90}Y. Conversely, Ward et al.[88], who reviewed 409 patients, reported a low, but significant, correlation between increased hepatopulmonary shunt fraction, measured using planar ^{99m}Tc-MAA, and HCC, hepatic vein tumor thrombus and portal vein tumor thrombus. Several limitations apply to this study, apart from its retrospective and single-center nature. Considering the planar ^{99m}Tc based LMD_{MAA} computation, the main limitation is the use of a surrogate model using MAA particle as an approximation to ^{90}Y microsphere distribution. In addition, lungs and liver were delineated on planar scintigraphy without anatomical reference and assuming a fixed lung mass of 1 kg. This means that female patients, who have a smaller organ mass[89], [90], with the same lung shunt as male patients may have received a larger lung radiation dose for the same treatment activity. As for the ^{90}Y PET based LMD_{Y-90} computation, a constant value for the lung density was used. However, as reported by Kappadath et al.[91], this might be a limiting factor in an accurate estimate of the LMD_{Y-90}. Although this study relied on the assumption of lung

7
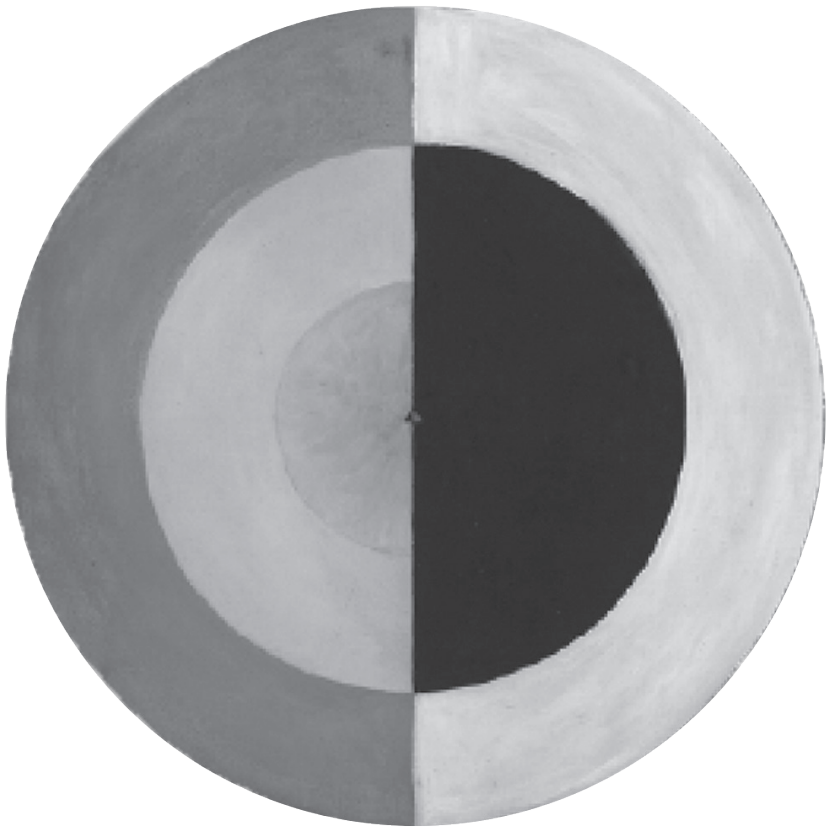
homogeneity, given the incomplete lungs within the PET field of view for some dataset, the distribution of microspheres in vivo is heterogeneous[35]. The gravitational dependence of alveolar and vascular pressures within the lung cause preferential distribution of blood flow and, in parallel, microspheres to the bases of the lung[57]. In addition, microsphere irradiation is not microscopically uniform[92]. However, in case of radiation pneumonitis occurrence, the assumption of uniform distribution in the lung was visually confirmed by the contrast enhanced CT acquired during the follow-up. Regardless, these limitations are a reflection of the current protocols and the treatment of patients. Moreover, radiation pneumonitis is a rare side effect of radioembolization, with just two cases over 317 procedures in this study, number of events is too limited for any realistic statistical analysis.

Despite the aforementioned limitations, a better predictive particle and a new lung dose limit are essential to improve the current general patient selection avoiding unjustified patient exclusion. Given the proven value of post-treatment ^{90}Y PET/CT[56], more insight should be gained in the real lung dose delivered after the treatment, compared to the predicted one.

Conclusion

This observational study showed that radiation pneumonitis did not occur among subjects with left mean lung dose below 12Gy, defined on post-treatment ^{90}Y-PET/CT. ^{99m}Tc-MAA-based planar lung dose estimate cut-off of >30Gy is capricious and, once encountered in pre-treatment imaging, should be evaluated with caution, to prevent unjustified treatment exclusion.

7

CHAPTER 8

Summary and Discussion

Summary

During the last decade, the use of holmium-166 (^{166}Ho) microspheres as radioembolization device has been increasing throughout Europe.

Chapter 1 presented the use of ^{166}Ho microspheres as an alternative to ^{90}Y for radioembolization, both during the scout and the treatment, describing the steps involved in the clinical workflow. ^{166}Ho imaging possibilities, particularly SPECT, were also presented. Additionally, the ^{166}Ho-^{99m}Tc dual isotope protocol was introduced.

Part I - ^{166}Ho SPECT imaging

Radioembolization planning and outcome is closely related to dosimetry assessment. However, dosimetry relies on adequate imaging, especially when clinical (non-quantitative) reconstructions are used. In the first part of this thesis, the technical challenges related to ^{166}Ho SPECT imaging in the clinical setting have been presented.

Since high activities (several GBq) of ^{166}Ho–labeled microspheres are used for therapeutic radioembolization, scanning patients shortly after administration can impact gamma camera performance, possibly hampering accuracy of dosimetry. **Chapter 2** assessed the impact of the high-count rate on ^{166}Ho SPECT imaging using an anthropomorphic phantom, filled with activity up to 2.7 GBq. The high-count regime did not affect image quality when visually assessed, nor the possibility of reliable dosimetry within the healthy liver. However, tumor dosimetry was hampered due to the gamma camera dead time.

Absolute activity is not the only parameter influencing ^{166}Ho SPECT imaging. ^{166}Ho has a complex spectrum, with the main photopeak window contaminated by scatter from ^{166}Ho high energy gamma emissions. In a separate study, ^{99m}Tc colloid is intravenously injected, after ^{166}Ho administration, with the purpose of imaging the healthy liver parenchyma. This requires a dedicated dual-isotope imaging protocol to separate ^{166}Ho and ^{99m}Tc signal into individual SPECT reconstructions. When a dual-isotope protocol is used as well, the additional isotope, ^{99m}Tc, and its main photopeak window centered at 140 keV can further influence ^{166}Ho main photopeak. To account for the scatter coming from ^{99}Tc and ^{166}Ho high energies, different scatter correction factors were tested in **Chapter 3**, using both phantom measurements and patient data.

To further optimize ^{166}Ho SPECT imaging, an additional imaging protocol was tested using phantom measurements. **Chapter 4** described the acquisition protocols and the impact of different reconstruction methods on image quality. The proposed protocols have been adopted

in a multi-center study performed among different centers in The Netherlands, with the purpose of harmonizing ^{166}Ho SPECT image quality.

Part II – Dosimetry

The ^{166}Ho-^{99m}Tc dual-isotope protocol can improve dosimetry by facilitating the delineation of the healthy liver parenchyma. However, ^{166}Ho images acquired in presence of an additional isotope should be proven to be suitable to conduct ^{166}Ho dosimetry. **Chapter 5** compared the resulting dosimetry using ^{166}Ho images acquired in presence or not of ^{99m}Tc, assessing three volumes of interest: lungs, healthy liver and tumors.

The automatic healthy liver segmentation method presented in **Chapter 3** for a phantom study was applied to patient data in **Chapter 6**. The resulting healthy liver masks were compared to the manual segmentation performed by an experienced physician with respect to dosimetry and overlap-indices. Relation between toxicity and healthy liver dose was also assessed.

Besides healthy liver toxicity, also radiation pneumonitis can be a side-effect of radioembolization. Radioembolization occurrence and lung dose measured on post-treatment PET following ^{90}Y radioembolization treatment was presented in **Chapter 7**.

Discussion

Radioembolization

The liver radioembolization procedure is based on two premises: i) hepatic tumors are mainly supplied by the hepatic artery; ii) radiation is tumoricidal if sufficient doses can be delivered selectively to the target volume. Thus, the use of a high-energy radiation source combined with an appropriate-size embolic microscopic particle administered transarterially would allow radiation to be delivered preferentially to the tumor. This allows the beads to irradiate the tumor while sparing healthy liver tissue.

The premises on which liver radioembolization is based should be verified on a patient-based level. This means that, prior to a treatment, a favorable dose distribution between tumor and healthy liver, and the exclusion of any extrahepatic deposition, should be confirmed. In particular, an important step before proceeding with a radioembolization treatment is to check for a potential lung shunt, to prevent radiation pneumonitis, a rare but severe complication. Following the treatment, dosimetry should again be performed, not only to assess the treatment outcome, but also to provide additional data to determine the dose-response and dose-toxicity thresholds that would ultimately unlock the large-scale implementation of personalized treatment.

Dosimetry

According to the current holmium-166 ([166]Ho)-microspheres (QuiremSpheres™, Quirem Medical B.V., The Netherlands) instruction for use, the recommended average whole-liver planned absorbed dose is 60 Gy, based on a phase 1, dose-escalation study [10]. This holds for all patients, despite the actual tumor-to-non-tumor absorbed dose estimated during the planning phase. However, a multi-compartmental model would better support the introduction of personalized dosimetry in the radioembolization field [35]. A personalized approach based on technetium-99m macroaggregated albumin (^{99m}Tc-MAA) SPECT/CT, showed improved objective response rate in patients treated with yttrium-90 (^{90}Y) [93]. [166]Ho radioembolization would benefit a similar prospective study, especially considering the possibility to personalize the treatment based on a commercially available scout particle which is the same as the one used for treatment. However, the implementation of a personalized approach for [166]Ho requires more insights to be gained in the relation between dose and tumor response and between dose and healthy liver toxicity [67]. To this end, dosimetry plays a key role. To obtain robust dosimetric data, two key components are essential: adequate images, and reliable segmentation to define volumes of interest that delineate healthy tissue and tumors. Additional to these two aspects, which will be further discussed in the following with respect to [166]Ho, some considerations on voxel-based dosimetry and standardized dosimetry apply to the field of radioembolization dosimetry regardless of the isotope used. Voxel-based dosimetry would allow a measure of dose heterogeneity within the tumors, especially relevant for some liver cancers presenting large, necrotic, and heterogeneous lesions. This approach might further elucidate the dose-response relation in different tumor types, even though its relevance and clinical applicability is still under debate [94]. Furthermore voxel-based dosimetry can be extracted from nuclear medicine images, but only with limited accuracy, thus requiring a high resolution imaging such as MRI. Standardized dosimetry, together with standardized methods through which dose thresholds are defined, would instead be directly applicable to retrospective analysis and prospective trials. This would facilitate and streamline the dose-response evaluation process in the coming years.

Imaging

Clinically reconstructed SPECT images are not intrinsically quantitative. This means that, provided a reconstructed image free of artefacts and corrected for attenuation and scatter, the value of each voxel does not directly express the activity in the voxel itself, for which a conversion factor is needed. Nonetheless they can be used for dosimetric purposes as long as they are scaled to the known injected activity. However, some precautions are needed when SPECT images are used for dose quantification. Especially for post-treatment

evaluation, in case the SPECT scan is acquired relatively shortly after treatment, activity levels in the patient are still high and may result in non-linear phenomena of the gamma camera, including the pulse pile-up effect and dead time. The resulting count-loss might cause an underestimation of the tumor absorbed dose during the post-treatment evaluation. Underestimation of tumor absorbed dose is further emphasized by the partial volume effect, which is more pronounced for smaller lesions. For these reasons, when clinically reconstructed SPECT images are used for dosimetry quantification, the performance of the gamma camera, used to acquire these scans, should be known exactly. In addition, the isotope ^{166}Ho has a complex spectrum that requires corrections for scatter from high-energy gamma emissions. So far, when reconstructing with commercially available software, this has been accounted for by using a dual energy window scatter correction method. This method implies the use of a scatter correction factor, weighting the scatter estimate in the main photopeak. However, this approach does not take into account the scatter coming from the main photopeak and uses a scatter correction factor dependent on window width. To tackle these issues, a triple energy window scatter correction method was proposed in this dissertation, allowing for an easier ^{166}Ho SPECT imaging protocol, in analogy with imaging procedures of other isotopes such as lutetium-177 (^{177}Lu) and iodine-123 (^{123}I). The benefit of a triple energy window scatter correction is not limited to an improved scatter correction, but also a more handy reconstruction implementation (automatic scatter window weights computation), which can favor the harmonization of ^{166}Ho SPECT acquisition in the clinical setting. Thus, the resulting ^{166}Ho-microspheres SPECT images can constitute the basic component to perform a dosimetric assessment during the pre- and post- treatment phase.

When mentioning ^{166}Ho imaging, it is worth to mention that this dissertation focused solely on ^{166}Ho SPECT imaging and dosimetry. ^{166}Ho, however, being a lanthanide, can also be imaged and quantified with MRI [6][95][7]. Roosen *et al.* [16] demonstrated the feasibility of intraprocedural MRI-based dosimetry, which could make ^{166}Ho radioembolization an image-guided procedure. Dosimetric evaluation of pre- and post-treatment ^{166}Ho imaging comparing SPECT and MRI are instead expected in the near future from secondary analyses of the HEPAR Primary study [17]. Voxel-based dosimetry for ^{166}Ho using MRI imaging could also provide further insight in the eventual benefit of a voxel-based approach compared to the currently used mean absorbed dose values.

Segmentation

A paramount step for radioembolization dosimetry is the delineation of the volumes of interest. The segmentation of these VOIs is a task that is still manually performed. The physician delineates the VOIs on the anatomical image (either a contrast enhanced CT or an

MRI), usually acquired up to weeks before the radioembolization treatment, and manually registers these onto the corresponding SPECT. This results into a time consuming and prone to error process, far from being optimal. Moreover, it prevents dosimetry to become a routinely applied step in the context of radioembolization. Being subject to mistakes coming from different sources, the reliability of the resulting dosimetric findings might be ultimately questioned. In particular, the registration between contrast enhanced CT and the corresponding SPECT/CT is a challenging task. The time passed between baseline CT/MRI and SPECT (i.e. usually around four weeks) and the longer acquisition time for SPECT (while patient breaths) might require the adjustment of the VOIs, eventually using a non-rigid registration to compensate for liver deformations that occurred between the scans. This introduces an additional user-dependent variability. In this dissertation, a simultaneous acquisition of ^{166}Ho, for both scout and treatment, and technetium-99m (^{99m}Tc) stannous phytate for non-tumorous healthy liver delineation was investigated. This ^{166}Ho-^{99m}Tc dual-isotope protocol proved to be a feasible option to provide an automatic segmentation of the healthy liver within the ^{166}Ho-microspheres radioembolization context. However, such dual-isotope SPECT protocol comes with its own set of challenges, most notably the need to ensure that ^{166}Ho and ^{99m}Tc reconstructions are suitable for dosimetry and automatic healthy liver segmentation, respectively.

^{166}Ho-^{99m}Tc dual-isotope

The introduction of ^{166}Ho-^{99m}Tc dual-isotope protocol has the main benefit of automation of the healthy liver segmentation process, making dosimetry a more feasible, less time-consuming tool in clinical practice. When the ^{166}Ho-^{99m}Tc dual-isotope protocol is adopted, the presence of the two radionuclides leads to a reciprocal influence between the two, which has to be taken into account during the image reconstruction phase. In particular, the ^{166}Ho main photopeak, at 81 keV, is affected by the downscatter from ^{99m}Tc, which has its main photopeak at 140 keV. Vice versa, ^{99m}Tc is contaminated by downscatter from the ^{166}Ho high-energy gamma emissions and bremsstrahlung. In this context, the choice of the correct scatter correction factor being able to reduce the impact of ^{99m}Tc on ^{166}Ho signal is especially important for accurate dosimetry. It is worth noting that there is no single k-factor that is optimal to fully compensate for scatter across the whole ^{166}Ho image, stressing how the application of window-based scatter correction is only an approximation to correct a complex, nonlinear, phenomenon.

Notwithstanding, it was shown that ^{166}Ho reconstructions derived from a ^{166}Ho-^{99m}Tc dual-isotope protocol have similar qualitative and quantitative quality compared with ^{166}Ho

reconstructions acquired in the presence of ^{166}Ho only. This gives confidence in adopting the ^{166}Ho-^{99m}Tc dual-isotope protocol in clinic, without hampering the ^{166}Ho dosimetry assessment. The technical challenges rising from the impact of additional ^{99m}Tc onto ^{166}Ho reconstructions should not discourage its adoption for the purpose of automatic healthy liver segmentation. The clinical routine would substantially benefit from a workflow that can automatically estimate the healthy liver dose estimate from the scout, without the tedious task of healthy liver delineation and registration. Using the healthy liver dose as driving parameter to determine the injected activity, ensuring a tolerable toxicity to the healthy liver, was also proposed for ^{90}Y microspheres [66] and could be adopted for ^{166}Ho, making the treatment planning a step closer to an individualized approach and facilitating same-day ^{166}Ho radioembolization simulation and treatment.

^{166}Ho-^{99m}Tc dual-isotope protocol could also be considered for automatic tumors segmentation. Whereas healthy liver dose can be used as driving parameter during the planning phase of radioembolization, dose-response values and tumor to non-tumor ratios require the determination of the tumor VOI. The information provided by ^{166}Ho and ^{99m}Tc reconstructions acquired simultaneously could be combined to automatically segment tumors. Lack of signal in the ^{99m}Tc reconstructions (since ^{99m}Tc stannous phytate accumulates in the Kupffer cells present in the healthy liver) and signal in the ^{166}Ho reconstructions (for hypervascular lesions) in the corresponding location indicate high probability of a tumorous region. Preliminary investigations were conducted in this direction to assess the feasibility of this approach. However, automatize dosimetry assessment for the tumor VOI presents additional challenges compared to the healthy liver VOI. Among these, the limited SPECT resolution, hampering the identification of small volumes of interest, and the identification of the perfused volume for lobar treatments.

Future prospective

More than a decade has passed since the first clinical study with ^{166}Ho-microspheres was carried out. Since then, ^{166}Ho-microspheres have become a valuable alternative to ^{90}Y-microspheres for liver radioembolization. Because the isotope ^{166}Ho is not only a beta but also a gamma emitter, and a lanthanide, it can be imaged using SPECT, and MRI, respectively. Additionally, the same particle can be used for both scout and treatment, while so far for ^{90}Y this was proven feasible in a phantom [3] and in a clinical study [4] but it is not (yet) commercially available. These unique features can be exploited in clinical practice, provided that a solid knowledge on both the technical and the clinical aspect is built.

8

In this dissertation, important technical aspects covering [166]Ho-microspheres SPECT imaging and the potential of a [166]Ho-^{99m}Tc dual-isotope protocol in clinical practice were covered. However, there is still room to further consolidate and improve the use of this radioisotope for liver radioembolization.

Looking at the recent innovations implemented in the field of SPECT imaging, the new digital detectors for gamma cameras might play a revolutionary role. These detectors are supposed to have an almost null dead time/detector saturation, addressing the nonlinear phenomena encountered at higher count-rate. They also have an improved energy and spatial resolution, beneficial for scatter correction and lesion detection. This could eventually allow SPECT-based automatic tumor segmentation and dosimetric assessment.

A decade ago, an improved reconstruction algorithm for quantitative [166]Ho SPECT, which includes Monte Carlo-based modeling of photon contributions from the full energy spectrum (scatter and attenuation effects in the patient, in combination with a distance- and energy-dependent model of the collimator-detector response in the patient), was proposed [32]. Back then, this approach was not applicable in clinical routine, partly because of the time needed to perform these reconstructions. However, with the improved computational power currently available, this approach can be validated for clinical use and adopted in clinical routine.

As stressed in this dissertation, a factor limiting the large-scale adoption of personalized dosimetry in current clinical practice is the necessity of segmenting the region of interest. The [166]Ho-^{99m}Tc dual-isotope protocol can offer an automatic alternative to the manual delineation of the healthy liver. However, further investigations need to be carried out to enable this protocol to become a robust method. This task too, can benefit from the recent advancements in the field of image analysis. With the increasing development of artificial intelligence, images derived from the [166]Ho-^{99m}Tc dual-isotope protocol could be a suitable input for a neural network trained for the automatic classification of the region of interest, provided that a reliable ground truth is also given. To this end, a contrast enhanced CT acquired together with the SPECT might improve the process, providing a better reference to which to compare resulting classified regions. Additionally, to compensate for respiration, a degrading effect on image quality, gating options should be investigated in the clinical scenario, given the promising results obtained with simulations [96].

If the improvement in the technology is a robust starting point to obtain images for reliable dosimetry, the dosimetric knowledge built using these images should be a cooperative effort. In this direction, a standardized [166]Ho SPECT imaging protocol would facilitate the comparison of dosimetric outcomes between centers, which may be vital to determine dose-

response relationships, and thus to plan the injected activity accordingly. Additionally, such protocol would facilitate a wide-spread adoption of [166]Ho-microspheres radioembolization, overcoming the imaging difficulties related to its complex spectrum, especially when acquired in presence of [99m]Tc. Guidelines for [166]Ho SPECT imaging should consider the differences among scanner systems (e.g. collimators characteristics) and the possibility to use vendor neutral software for reconstruction, to harmonize the resulting image quality among imaging centers. Dependent on the aim, either quantitation or visual image quality, scans should be reconstructed accordingly, to ensure both the possibility of performing dosimetry and providing images suitable for their assessment by physicians. [166]Ho-microspheres radioembolization would benefit from a unified methodology for dosimetry, similar to what has been proposed by EANM dosimetry committee series for ^{99m}Tc-MAA and ^{90}Y-microspheres [58]. Reliable images and shared methodologies would help the determination of dose-response and dose-toxicity values for [166]Ho-microspheres radioembolization. After the determination of these dose threshold values, a prospective study would be the ideal validation of these limits, which might help to finally introduce the partition model for [166]Ho-microspheres activity prescription.

With theranostics leading a transition from conventional nuclear medicine to contemporary personalized medicine, and the continuous development of imaging systems, [166]Ho-microspheres, with their unique characteristics, might have all the credentials to play a key role in liver radioembolization in the future. Optimizing SPECT imaging to this purpose will support personalized dosimetry in becoming a routine clinical practice.

8

CHAPTER 9

Bibliography

[1] T. Riemenschneider, C. Ruf, H. C. Kratzsch, M. Ziegler, and G. Späth, "Arterial, portal or combined arterio-portal regional chemotherapy in experimental liver tumours?," *J. Cancer Res. Clin. Oncol.*, vol. 118, no. 8, pp. 597–600, 1992, doi: 10.1007/BF01211803.

[2] R. J. Mumper, U. Y. Ryo, and M. Jay, "Neutron-activated holmium-166-poly (L-lactic acid) microspheres: a potential agent for the internal radiation therapy of hepatic tumors.," *J. Nucl. Med.*, vol. 32, no. 11, pp. 2139–43, Nov. 1991, [Online]. Available: http://www.ncbi.nlm.nih.gov/pubmed/1941151

[3] F. Nijsen *et al.*, "Targeting of liver tumour in rats by selective delivery of holmium-166 loaded microspheres: A biodistribution study," *Eur. J. Nucl. Med.*, vol. 28, no. 6, pp. 743–749, 2001, doi: 10.1007/s002590100518.

[4] M. L. J. Smits *et al.*, "Holmium-166 radioembolization for the treatment of patients with liver metastases: Design of the phase i HEPAR trial," *J. Exp. Clin. Cancer Res.*, vol. 29, no. 1, pp. 1–11, 2010, doi: 10.1186/1756-9966-29-70.

[5] J. F. W. Nijsen, W. Bult, and A. D. Van Het Schip, "A microsphere comprising an organic lanthanide metal complex," no. EP 2178817 B1. 2008. [Online]. Available: https://lens.org/082-243-414-405-157

[6] G. H. Van De Maat *et al.*, "MRI-based biodistribution assessment of holmium-166 poly(L-lactic acid) microspheres after radioembolisation," *Eur. Radiol.*, vol. 23, no. 3, pp. 827–835, 2013, doi: 10.1007/s00330-012-2648-2.

[7] M. L. J. Smits *et al.*, "In vivo dosimetry based on SPECT and MR imaging of 166Ho- microspheres for treatment of liver malignancies," *J. Nucl. Med.*, vol. 54, no. 12, pp. 2093–2100, 2013, doi: 10.2967/jnumed.113.119768.

[8] A. Kennedy *et al.*, "Recommendations for Radioembolization of Hepatic Malignancies Using Yttrium-90 Microsphere Brachytherapy: A Consensus Panel Report from the Radioembolization Brachytherapy Oncology Consortium," *Int. J. Radiat. Oncol. Biol. Phys.*, vol. 68, no. 1, pp. 13–23, 2007, doi: 10.1016/j.ijrobp.2006.11.060.

[9] A. J. A. T. Braat, J. F. Prince, R. van Rooij, R. C. G. Bruijnen, M. A. A. J. van den Bosch, and M. G. E. H. Lam, "Safety analysis of holmium-166 microsphere scout dose imaging during radioembolisation work-up: A cohort study," *Eur. Radiol.*, vol. 28, no. 3, pp. 920–928, 2018, doi: 10.1007/s00330-017-4998-2.

[10] M. L. J. Smits *et al.*, "Holmium-166 radioembolisation in patients with unresectable, chemorefractory liver metastases (HEPAR trial): a phase 1, dose-escalation study.," *Lancet. Oncol.*, vol. 13, no. 10, pp. 1025–34, Oct. 2012, doi: 10.1016/S1470-2045(12)70334-0.

[11] "Quirem Medical B.V. QuiremSpheres - Instruction for use.," 2020.

[12] C. van Roekel *et al.*, "Evaluation of the Safety and Feasibility of Same-Day Holmium-166 -Radioembolization Simulation and Treatment of Hepatic Metastases," *J. Vasc. Interv. Radiol.*, vol. 31, no. 10, pp. 1593–1599, 2020, doi: 10.1016/j.jvir.2020.01.032.

[13] A. J. A. T. Braat *et al.*, "Additional holmium-166 radioembolisation after lutetium-177-dotatate in patients with neuroendocrine tumour liver metastases (HEPAR PLuS): a single-centre, single-arm, open-label, phase 2 study.," *Lancet. Oncol.*, vol. 21, no. 4, pp. 561–570, Apr. 2020, doi: 10.1016/S1470-2045(20)30027-9.

[14] M. G. E. H. E. Lam *et al.*, "Fusion dual-tracer SPECT-based hepatic dosimetry predicts outcome after radioembolization for a wide range of tumour cell types," *Eur. J. Nucl. Med. Mol. Imaging*, vol. 42, no. 8, pp. 1192–1201, Jul. 2015, doi: 10.1007/s00259-015-3048-z.

[15] R. van Rooij, A. J. A. T. Braat, H. W. A. M. de Jong, and M. G. E. H. Lam, "Simultaneous 166Ho/99mTc dual-isotope SPECT with Monte Carlo-based downscatter correction for automatic liver dosimetry in radioembolization," *EJNMMI Phys.*, vol. 7, no. 1, 2020, doi: 10.1186/s40658-020-0280-9.

[16] J. Roosen *et al.*, "Intraprocedural MRI-based dosimetry during transarterial radioembolization of liver tumours with holmium-166 microspheres (EMERITUS-1): a phase I trial towards adaptive, image-controlled treatment delivery," *Eur. J. Nucl. Med. Mol. Imaging*, pp. 4705–4715, 2022, doi: 10.1007/s00259-022-05902-w.

[17] M. T. M. Reinders *et al.*, "Safety and efficacy of holmium-166 radioembolization in hepatocellular carcinoma - the HEPAR Primary study.," *J. Nucl. Med.*, vol. 44, no. S1, p. jnumed.122.263823, May 2022, doi: 10.2967/jnumed.122.263823.

[18] C. van Roekel *et al.*, "Use of an anti-reflux catheter to improve tumor targeting for holmium-166 radioembolization—a prospective, within-patient randomized study," *Eur. J. Nucl. Med. Mol. Imaging*, vol. 48, no. 5, pp. 1658–1668, 2021, doi: 10.1007/s00259-020-05079-0.

[19] J. F. Prince *et al.*, "Efficacy of Radioembolization with 166 Ho-Microspheres in Salvage Patients with Liver Metastases: A Phase 2 Study," *J. Nucl. Med.*, vol. 59, no. 4, pp. 582–588, Apr. 2018, doi: 10.2967/jnumed.117.197194.

[20] M. T. M. Reinders, M. L. J. Smits, C. van Roekel, and A. J. A. T. Braat, "Holmium-166 Microsphere Radioembolization of Hepatic Malignancies," *Semin. Nucl. Med.*, vol. 49, no. 3, pp. 237–243, 2019, doi: 10.1053/j.semnuclmed.2019.01.008.

[21] M. L. J. Smits *et al.*, "The superior predictive value of 166Ho-scout compared with 99mTc-macroaggregated albumin prior to 166Ho-microspheres radioembolization in patients with liver metastases," *Eur. J. Nucl. Med. Mol. Imaging*, Aug. 2019, doi: 10.1007/s00259-019-04460-y.

[22] M. Elschot, J. F. W. Nijsen, A. J. Dam, and H. W. A. M. de Jong, "Quantitative evaluation of scintillation camera imaging characteristics of isotopes used in liver radioembolization," *PLoS One*, vol. 6, no. 11, 2011, doi: 10.1371/journal.pone.0026174.

[23] T. C. de Wit *et al.*, "Hybrid scatter correction applied to quantitative holmium-166 SPECT.," *Phys. Med. Biol.*, vol. 51, no. 19, pp. 4773–87, Oct. 2006, doi: 10.1088/0031-9155/51/19/004.

[24] E. Garin *et al.*, "Dosimetry based on 99mTc-macroaggregated albumin SPECT/CT accurately predicts tumor response and survival in hepatocellular carcinoma patients treated with 90Y-loaded glass microspheres: Preliminary results," *J. Nucl. Med.*, vol. 53, no. 2, pp. 255–263, 2012, doi: 10.2967/jnumed.111.094235.

[25] S. Ho *et al.*, "Tumour-to-normal uptake ratio of 90Y microspheres in hepatic cancer assessed with 99TCm macroaggregated albumin," *Br. J. Radiol.*, vol. 70, no. AUG., pp. 823–828, 1997, doi: 10.1259/bjr.70.836.9486047.

[26] B. J. van Nierop, J. F. Prince, R. van Rooij, M. A. A. J. van den Bosch, M. G. E. H. Lam, and H. W. A. M. de Jong, "Accuracy of SPECT/CT-based lung dose calculation for Holmium-166 hepatic radioembolization before OSEM convergence," *Med. Phys.*, vol. 45, no. 8, pp. 3871–3879, 2018, doi: 10.1002/mp.13024.

[27] M. Stella, A. Braat, M. Lam, H. de Jong, and R. van Rooij, "Quantitative 166Ho-microspheres SPECT derived from a dual-isotope acquisition with 99mTc-colloid is clinically feasible," *EJNMMI Phys.*, vol. 7, no. 1, 2020, doi: 10.1186/s40658-020-00317-8.

[28] M. Silosky, V. Johnson, C. Beasley, and S. Cheenu Kappadath, "Characterization of the count rate performance of modern gamma cameras," *Med. Phys.*, vol. 40, no. 3, p. 032502, Feb. 2013, doi: 10.1118/1.4792297.

9

[29] P. A. Yushkevich *et al.*, "User-guided 3D active contour segmentation of anatomical structures: Significantly improved efficiency and reliability," *Neuroimage*, vol. 31, no. 3, pp. 1116–1128, 2006, doi: 10.1016/j.neuroimage.2006.01.015.

[30] H. Dittmann *et al.*, "A Prospective Study of Quantitative SPECT/CT for Evaluation of Lung Shunt Fraction Before SIRT of Liver Tumors," *J. Nucl. Med.*, vol. 59, no. 9, pp. 1366–1372, Sep. 2018, doi: 10.2967/jnumed.117.205203.

[31] J. Gear *et al.*, "EANM Dosimetry Committee series on standard operational procedures for internal dosimetry for 131I mIBG treatment of neuroendocrine tumours," *EJNMMI Phys.*, vol. 7, no. 1, p. 15, Dec. 2020, doi: 10.1186/s40658-020-0282-7.

[32] M. Elschot *et al.*, "Quantitative Monte Carlo-based holmium-166 SPECT reconstruction," *Med. Phys.*, vol. 40, no. 11, 2013, doi: 10.1118/1.4823788.

[33] J. D. Allred, J. Niedbala, J. K. Mikell, D. Owen, K. A. Frey, and Y. K. Dewaraja, "The value of 99mTc-MAA SPECT/CT for lung shunt estimation in 90Y radioembolization: a phantom and patient study," *EJNMMI Res.*, vol. 8, no. 1, p. 50, Dec. 2018, doi: 10.1186/s13550-018-0402-8.

[34] M. T. M. Reinders *et al.*, "Radioembolisation in Europe: A Survey Amongst CIRSE Members," *Cardiovasc. Intervent. Radiol.*, vol. 41, no. 10, pp. 1579–1589, 2018, doi: 10.1007/s00270-018-1982-4.

[35] R. Bastiaannet, S. C. Kappadath, B. Kunnen, A. J. A. T. Braat, M. G. E. H. Lam, and H. W. A. M. de Jong, "The physics of radioembolization," *EJNMMI Phys.*, vol. 5, no. 1, 2018, doi: 10.1186/s40658-018-0221-z.

[36] S. Klein, M. Staring, K. Murphy, M. A. Viergever, and J. P. W. Pluim, "elastix: A Toolbox for Intensity-Based Medical Image Registration," *IEEE Trans. Med. Imaging*, vol. 29, no. 1, pp. 196–205, 2010, doi: 10.1109/TMI.2009.2035616.

[37] D. P. Shamonin *et al.*, "Fast parallel image registration on CPU and GPU for diagnostic classification of Alzheimer's disease.," *Front. Neuroinform.*, vol. 7, no. JAN, p. 50, 2013, doi: 10.3389/fninf.2013.00050.

[38] M. Stella, A. J. A. T. Braat, M. G. E. H. Lam, H. W. A. M. de Jong, and R. van Rooij, "Gamma camera characterization at high holmium-166 activity in liver radioembolization," *EJNMMI Phys.*, vol. 8, no. 1, p. 22, Dec. 2021, doi: 10.1186/s40658-021-00372-9.

[39] A. Carass *et al.*, "Evaluating White Matter Lesion Segmentations with Refined Sørensen-Dice Analysis," *Sci. Rep.*, vol. 10, no. 1, pp. 1–19, 2020, doi: 10.1038/s41598-020-64803-w.

[40] A. J. A. T. Braat *et al.*, "Additional hepatic 166Ho-radioembolization in patients with neuroendocrine tumours treated with 177Lu-DOTATATE; a single center, interventional, non-randomized, non-comparative, open label, phase II study (HEPAR PLUS trial).," *BMC Gastroenterol.*, vol. 18, no. 1, p. 84, Jun. 2018, doi: 10.1186/s12876-018-0817-8.

[41] S. M. B. Peters *et al.*, "Towards standardization of absolute SPECT/CT quantification: a multi-center and multi-vendor phantom study," *EJNMMI Phys.*, vol. 6, no. 1, 2019, doi: 10.1186/s40658-019-0268-5.

[42] D. M. V. Huizing, M. Sinaasappel, M. C. Dekker, M. P. M. Stokkel, and B. J. de Wit – van der Veen, "177Lutetium SPECT/CT: Evaluation of collimator, photopeak and scatter correction," *J. Appl. Clin. Med. Phys.*, vol. 21, no. 9, pp. 272–277, 2020, doi: 10.1002/acm2.12991.

[43] Y. Dewaraja, Jia Li, and K. Koral, "Quantitative /sup 131/I SPECT with triple energy window Compton scatter correction," *IEEE Trans. Nucl. Sci.*, vol. 45, no. 6, pp. 3109–3114, Dec. 1998, doi: 10.1109/23.737672.

[44] V. Lagerburg, R. De Nijs, S. Holm, and C. Svarer, "A comparison of different energy window subtraction methods to correct for scatter and downscatter in I-123 SPECT imaging," *Nucl. Med. Commun.*, vol. 33, no. 7, pp. 708–718, 2012, doi: 10.1097/MNM.0b013e3283537cd0.

[45] M. Holstensson, C. Hindorf, M. Ljungberg, M. Partridge, and G. D. Flux, "Optimization of energy-window settings for scatter correction in quantitative 111In imaging: Comparison of measurements and Monte Carlo simulations," *Cancer Biother. Radiopharm.*, vol. 22, no. 1, pp. 136–142, 2007, doi: 10.1089/cbr.2007.307.

[46] A. P. Robinson, J. Tipping, D. M. Cullen, and D. Hamilton, "The influence of triple energy window scatter correction on activity quantification for 1 7 7Lu molecular radiotherapy," *Phys. Med. Biol.*, vol. 61, no. 14, pp. 5107–5127, 2016, doi: 10.1088/0031-9155/61/14/5107.

[47] R. Bastiaannet *et al.*, "First evidence for a dose-Response relationship in patients treated with 166Ho radioembolization: A prospective study," *J. Nucl. Med.*, vol. 61, no. 4, pp. 608–612, 2020, doi: 10.2967/jnumed.119.232751.

[48] J. F. Prince, R. van Rooij, G. H. Bol, H. W. A. M. de Jong, M. A. A. J. van den Bosch, and M. G. E. H. Lam, "Safety of a Scout Dose Preceding Hepatic Radioembolization with 166Ho Microspheres.," *J. Nucl. Med.*, vol. 56, no. 6, pp. 817–23, Jun. 2015, doi: 10.2967/jnumed.115.155564.

[49] A. Braat, R. van Rooij, M. van den Bosch, and M. Lam, "Improved dosimetry in radioembolization using a dual isotope SPECT/CT protocol with 166Ho-microspheres and 99mTc-stannous phytate: a proof of concept," in *Journal of Nuclear Medicine*, 2016, vol. 57, no. supplement 2, pp. 1423–1423.

[50] G. T. Krishnamurthy and S. Krishnamurthy, "Imaging of the Liver and Spleen Morphology BT - Nuclear Hepatology: A Textbook of Hepatobiliary Diseases," G. T. Krishnamurthy and S. Krishnamurthy, Eds. Berlin, Heidelberg: Springer Berlin Heidelberg, 2000, pp. 59–91. doi: 10.1007/978-3-662-22654-4_4.

[51] C. Chiesa *et al.*, "The conflict between treatment optimization and registration of radiopharmaceuticals with fixed activity posology in oncological nuclear medicine therapy," *Eur. J. Nucl. Med. Mol. Imaging*, vol. 44, no. 11, pp. 1783–1786, 2017, doi: 10.1007/s00259-017-3707-3.

[52] D. R. White, J. Booz, R. V Griffith, J. J. Spokas, and I. J. Wilson, "Report 44," *J. Int. Comm. Radiat. Units Meas.*, vol. os23, no. 1, p. NP, 1989, doi: 10.1093/jicru/os23.1.Report44.

[53] C. G. Rhodes, P. Wollmer, F. Fazio, and T. Jones, "Quantitative measurement of regional extravascular lung density using positron emission and transmission tomography.," *J. Comput. Assist. Tomogr.*, vol. 5, no. 6, pp. 783–91, Dec. 1981, doi: 10.1097/00004728-198112000-00001.

[54] A. J. Viera and J. M. Garrett, "Understanding interobserver agreement: the kappa statistic.," *Fam. Med.*, vol. 37, no. 5, pp. 360–3, May 2005, doi: 10.1001/jama.268.18.2513.

[55] A. J. A. T. Braat *et al.*, "Radioembolization with 90 Y Resin Microspheres of Neuroendocrine Liver Metastases: International Multicenter Study on Efficacy and Toxicity," *Cardiovasc. Intervent. Radiol.*, vol. 42, no. 3, pp. 413–425, 2019, doi: 10.1007/s00270-018-2148-0.

[56] R. Salem *et al.*, "Incidence of radiation pneumonitis after hepatic intra-arterial radiotherapy with yttrium-90 microspheres assuming uniform lung distribution," *Am. J. Clin. Oncol. Cancer Clin. Trials*, vol. 31, no. 5, pp. 431–438, 2008, doi: 10.1097/COC.0b013e318168ef65.

[57] J. Armstrong *et al.*, "Promising survival with three-dimensional conformal radiation therapy for non-small cell lung cancer," *Radiother. Oncol.*, vol. 44, no. 1, pp. 17–22, Jul. 1997, doi: 10.1016/S0167-8140(97)01907-5.

[58] C. Chiesa *et al.*, "EANM dosimetry committee series on standard operational procedures: a unified methodology for 99mTc-MAA pre- and 90Y peri-therapy dosimetry in liver radioembolization with 90Y microspheres," *EJNMMI Phys.*, vol. 8, no. 1, 2021, doi: 10.1186/s40658-021-00394-3.

9

[59] Y. K. Dewaraja *et al.*, "Intra- and Inter-operator variability in manual tumor segmentation: Impact on radionuclide therapy dosimetry," pp. 1–18, 2022, doi: 10.21203/rs.3.rs-1408164/v1.

[60] M. Stella, A. J. A. T. Braat, M. G. E. H. Lam, H. W. A. M. de Jong, and R. van Rooij, "166Holmium–99mTechnetium dual-isotope imaging: scatter compensation and automatic healthy liver segmentation for 166Holmium radioembolization dosimetry," *EJNMMI Phys.*, vol. 9, no. 1, p. 30, Dec. 2022, doi: 10.1186/s40658-022-00459-x.

[61] K. P. Willowson, G. P. Schembri, E. J. Bernard, D. L. Chan, and D. L. Bailey, "Quantifying the effects of absorbed dose from radioembolisation on healthy liver function with [99mTc]TcMebrofenin," *Eur. J. Nucl. Med. Mol. Imaging*, vol. 47, no. 4, pp. 838–848, 2020, doi: 10.1007/s00259-020-04686-1.

[62] M. N. G. J. A. Braat, K. J. Van Erpecum, B. A. Zonnenberg, M. A. J. Van Den Bosch, and M. G. E. H. Lam, "Radioembolization-induced liver disease: A systematic review," *Eur. J. Gastroenterol. Hepatol.*, vol. 29, no. 2, pp. 144–152, 2017, doi: 10.1097/MEG.0000000000000772.

[63] G. C. A. Costa *et al.*, " Radioembolization Dosimetry with Total-Body 90 Y PET ," *J. Nucl. Med.*, p. jnumed.121.263145, 2021, doi: 10.2967/jnumed.121.263145.

[64] Y. Tomozawa *et al.*, "Long-Term Toxicity after Transarterial Radioembolization with Yttrium-90 Using Resin Microspheres for Neuroendocrine Tumor Liver Metastases," *J. Vasc. Interv. Radiol.*, vol. 29, no. 6, pp. 858–865, 2018, doi: 10.1016/j.jvir.2018.02.002.

[65] S. C. Ebbers, C. van Roekel, M. N. G. J. A. Braat, M. W. Barentsz, M. G. E. H. Lam, and A. J. A. T. Braat, "Dose–response relationship after yttrium-90-radioembolization with glass microspheres in patients with neuroendocrine tumor liver metastases," *Eur. J. Nucl. Med. Mol. Imaging*, vol. 49, no. 5, pp. 1700–1710, 2022, doi: 10.1007/s00259-021-05642-3.

[66] C. Chiesa *et al.*, "Radioembolization of hepatocarcinoma with 90Y glass microspheres: treatment optimization using the dose-toxicity relationship," *Eur. J. Nucl. Med. Mol. Imaging*, vol. 47, no. 13, pp. 3018–3032, 2020, doi: 10.1007/s00259-020-04845-4.

[67] C. van Roekel *et al.*, "Dose-effect relationships of 166Ho radioembolization in colorectal cancer," *J. Nucl. Med.*, vol. 62, no. 2, pp. 272–279, 2021, doi: 10.2967/jnumed.120.243832.

[68] E. Jafargholi Rangraz *et al.*, "Quantitative comparison of pre-treatment predictive and post-treatment measured dosimetry for selective internal radiation therapy using cone-beam CT for tumor and liver perfusion territory definition," *EJNMMI Res.*, vol. 10, no. 1, 2020, doi: 10.1186/s13550-020-00675-5.

[69] A. J. A. T. Braat *et al.*, "90Y hepatic radioembolization: An update on current practice and recent developments," *J. Nucl. Med.*, vol. 56, no. 7, pp. 1079–1087, 2015, doi: 10.2967/jnumed.115.157446.

[70] R. Salem and K. G. Thurston, "Radioembolization with 90Yttrium Microspheres: A State-of-the-Art Brachytherapy Treatment for Primary and Secondary Liver Malignancies," *J. Vasc. Interv. Radiol.*, vol. 17, no. 8, pp. 1251–1278, Aug. 2006, doi: 10.1097/01.RVI.0000233785.75257.9A.

[71] J. L. Peterson *et al.*, "Complications after 90Y microsphere radioembolization for unresectable hepatic tumors: An evaluation of 112 patients," *Brachytherapy*, vol. 12, no. 6, pp. 573–579, 2013, doi: 10.1016/j.brachy.2013.05.008.

[72] T. W. T. Leung *et al.*, "Radiation pneumonitis after selective internal radiation treatment with intraarterial 90Yttrium-microspheres for inoperable hepatic tumors," *Int. J. Radiat. Oncol. Biol. Phys.*, vol. 33, no. 4, pp. 919–924, 1995, doi: 10.1016/0360-3016(95)00039-3.

[73] S. Ho, W. Y. Lau, T. W. T. Leung, M. Chan, P. J. Johnson, and A. K. C. Li, "Clinical evaluation of the partition model for estimating radiation doses from yttrium-90 microspheres in the treatment of hepatic cancer," *Eur. J. Nucl. Med.*, vol. 24, no. 3, pp. 293–298, 1997, doi: 10.1007/s002590050055.

[74] S. C. Kappadath, B. P. Lopez, R. Salem, and M. G. E. H. Lam, "Reassessment of the lung dose limits for radioembolization," *Nucl. Med. Commun.*, vol. 42, no. 10, pp. 1064–1075, Oct. 2021, doi: 10.1097/MNM.0000000000001439.

[75] B. Lopez, A. Mahvash, M. G. E. H. Lam, and S. C. Kappadath, "Calculation of lung mean dose and quantification of error for 90Y-microsphere radioembolization using 99mTc-MAA SPECT/CT and diagnostic chest CT," *Med. Phys.*, vol. 46, no. 9, pp. 3929–3940, 2019, doi: 10.1002/mp.13575.

[76] M. Elschot *et al.*, "99mTc-MAA overestimates the absorbed dose to the lungs in radioembolization: a quantitative evaluation in patients treated with 166Ho-microspheres," *Eur. J. Nucl. Med. Mol. Imaging*, vol. 41, no. 10, pp. 1965–1975, 2014, doi: 10.1007/s00259-014-2784-9.

[77] M. Wondergem *et al.*, "99m Tc-Macroaggregated Albumin Poorly Predicts the Intrahepatic Distribution of 90 Y Resin Microspheres in Hepatic Radioembolization," *J. Nucl. Med.*, vol. 54, no. 8, pp. 1294–1301, Aug. 2013, doi: 10.2967/jnumed.112.117614.

[78] A. A. Alsultan, M. L. J. Smits, M. W. Barentsz, A. J. A. T. Braat, and M. G. E. H. Lam, "The value of yttrium-90 PET/CT after hepatic radioembolization: a pictorial essay," *Clin. Transl. Imaging*, vol. 7, no. 4, pp. 303–312, Aug. 2019, doi: 10.1007/s40336-019-00335-2.

[79] M. D'Arienzo *et al.*, "Phantom validation of quantitative Y-90 PET/CT-based dosimetry in liver radioembolization," *EJNMMI Res.*, vol. 7, no. 1, p. 94, Dec. 2017, doi: 10.1186/s13550-017-0341-9.

[80] B. Kunnen, C. Beijst, M. G. E. H. Lam, M. A. Viergever, and H. W. A. M. de Jong, "Comparison of the Biograph Vision and Biograph mCT for quantitative 90Y PET/CT imaging for radioembolisation," *EJNMMI Phys.*, vol. 7, no. 1, p. 14, Dec. 2020, doi: 10.1186/s40658-020-0283-6.

[81] J. Hofmanninger, F. Prayer, J. Pan, S. Röhrich, H. Prosch, and G. Langs, "Automatic lung segmentation in routine imaging is primarily a data diversity problem, not a methodology problem," *Eur. Radiol. Exp.*, vol. 4, no. 1, p. 50, Dec. 2020, doi: 10.1186/s41747-020-00173-2.

[82] A. S. Pasciak, A. C. Bourgeois, and Y. C. Bradley, "A Comparison of Techniques for 90Y PET/CT Image-Based Dosimetry Following Radioembolization with Resin Microspheres," *Front. Oncol.*, vol. 4, no. May, pp. 1–11, May 2014, doi: 10.3389/fonc.2014.00121.

[83] H. Levillain *et al.*, "International recommendations for personalised selective internal radiation therapy of primary and metastatic liver diseases with yttrium-90 resin microspheres," *Eur. J. Nucl. Med. Mol. Imaging*, vol. 48, no. 5, pp. 1570–1584, May 2021, doi: 10.1007/s00259-020-05163-5.

[84] M. Cremonesi *et al.*, "Radioembolization of hepatic lesions from a radiobiology and dosimetric perspective.," *Front. Oncol.*, vol. 4, no. August, p. 210, Aug. 2014, doi: 10.3389/fonc.2014.00210.

[85] C. Chiesa *et al.*, "Need, feasibility and convenience of dosimetric treatment planning in liver selective internal radiation therapy with (90)Y microspheres: the experience of the National Tumor Institute of Milan.," *Q. J. Nucl. Med. Mol. imaging*, vol. 55, no. 2, pp. 168–97, Apr. 2011, [Online]. Available: http://www.ncbi.nlm.nih.gov/pubmed/21386789

[86] B. Kunnen, S. van der Velden, R. Bastiaannet, M. G. E. H. Lam, M. A. Viergever, and H. W. A. M. de Jong, "Radioembolization lung shunt estimation based on a 90 Y pretreatment procedure: A phantom study," *Med. Phys.*, vol. 45, no. 10, pp. 4744–4753, Oct. 2018, doi: 10.1002/mp.13168.

[87] J. R. Kallini, A. Gabr, R. Salem, and R. J. Lewandowski, "Transarterial Radioembolization with Yttrium-90 for the Treatment of Hepatocellular Carcinoma," *Adv. Ther.*, vol. 33, no. 5, pp. 699–714, 2016, doi: 10.1007/s12325-016-0324-7.

[88] T. J. Ward *et al.*, "Management of High Hepatopulmonary Shunting in Patients Undergoing Hepatic Radioembolization," *J. Vasc. Interv. Radiol.*, vol. 26, no. 12, pp. 1751–1760, Dec. 2015, doi: 10.1016/j.jvir.2015.08.027.

9

[89] D. K. Molina and V. J. M. DiMaio, "Normal organ weights in women: Part II - The Brain, Lungs, Liver, Spleen, and Kidneys," *Am. J. Forensic Med. Pathol.*, vol. 36, no. 3, pp. 182–187, 2015, doi: 10.1097/PAF.0000000000000175.

[90] D. K. Molina and V. J. M. Dimaio, "Normal organ weights in men: Part II-the brain, lungs, liver, spleen, and kidneys," *Am. J. Forensic Med. Pathol.*, vol. 33, no. 4, pp. 368–372, 2012, doi: 10.1097/PAF.0b013e31823d29ad.

[91] S. C. Kappadath, B. P. Lopez, R. Salem, and M. G. Lam, "Lung shunt and lung dose calculation methods for radioembolization treatment planning.," *Q. J. Nucl. Med. Mol. imaging*, vol. 65, no. 1, pp. 32–42, Mar. 2021, doi: 10.23736/S1824-4785.20.03287-2.

[92] F. Giammarile *et al.*, "EANM procedure guideline for the treatment of liver cancer and liver metastases with intra-arterial radioactive compounds," *Eur. J. Nucl. Med. Mol. Imaging*, vol. 38, no. 7, pp. 1393–1406, Jul. 2011, doi: 10.1007/s00259-011-1812-2.

[93] E. Garin *et al.*, "Personalised versus standard dosimetry approach of selective internal radiation therapy in patients with locally advanced hepatocellular carcinoma (DOSISPHERE-01): a randomised, multicentre, open-label phase 2 trial," *Lancet Gastroenterol. Hepatol.*, vol. 6, no. 1, pp. 17–29, 2021, doi: 10.1016/S2468-1253(20)30290-9.

[94] C. Chiesa, M. Bardiès, and H. Zaidi, "Voxel-based dosimetry is superior to mean absorbed dose approach for establishing dose-effect relationship in targeted radionuclide therapy," *Med. Phys.*, vol. 46, no. 12, pp. 5403–5406, Dec. 2019, doi: 10.1002/mp.13851.

[95] G. H. Van De Maat, P. R. Seevinck, C. Bos, and C. J. G. Bakker, "Quantification of holmium-166 loaded microspheres: Estimating high local concentrations using a conventional multiple gradient echo sequence with S 0-fitting," *J. Magn. Reson. Imaging*, vol. 35, no. 6, pp. 1453–1461, 2012, doi: 10.1002/jmri.23593.

[96] R. Bastiaannet, M. A. Viergever, and H. W. A. M. De Jong, "Impact of respiratory motion and acquisition settings on SPECT liver dosimetry for radioembolization," *Med. Phys.*, vol. 44, no. 10, pp. 5270–5279, 2017, doi: 10.1002/mp.12483.
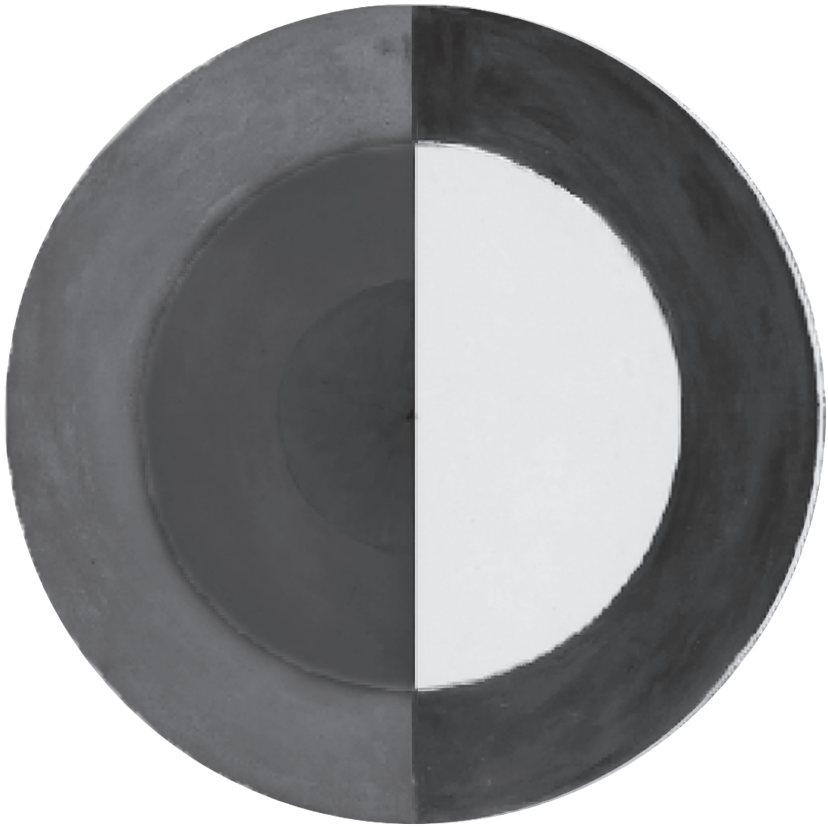
CHAPTER 10

Addenda

Nederlandse Samenvatting

De laatste jaren is het gebruik van holmium-166 (^{166}Ho) microspheren voor radioembolisatie toegenomen in Europa.

Hoofdstuk 1 beschrijft het gebruik van ^{166}Ho microspheren als een alternatief voor yttrium-90 (^{90}Y) tijdens radioembolisatie, zowel als partikel voor de simulatie als de behandeling, en beschrijft de benodigde stappen binnen de kliniek voor een dergelijke behandeling. De mogelijkheden om ^{166}Ho af te beelden, in het bijzonder SPECT, worden ook beschreven. Tegelijkertijd wordt het ^{166}Ho-^{99m}Tc dual-isotope protocol geïntroduceerd.

Deel I - ^{166}Ho SPECT beeldvorming

Radioembolisatie planning en uitkomsten zijn direct gerelateerd aan dosimetrie. Echter, dosimetrie is afhankelijk van betrouwbare beeldvorming, vooral wanneer klinische (niet-kwantitatieve) beeldreconstructies worden gebruikt. In het eerste deel van dit proefschrift worden de technische uitdagingen omtrent ^{166}Ho SPECT beeldvorming in de klinische setting beschreven.

Aangezien hoge mate van activiteit (enkele GBq) van ^{166}Ho–microspheren worden gebruikt voor een therapeutische behandeling, kan het scannen van patiënten kort na de behandeling de prestaties van een gammacamera beïnvloeden, wat een negatieve invloed kan hebben op de accuraatheid van de dosimetrie. **Hoofdstuk 2** beschrijft de invloed van hoge telsnelheden op ^{166}Ho SPECT door middel van een anthropomorfisch fantoom, gevuld met activiteit tot 2.7 GBq. De hoge telsnelheden hadden, kwalitatief beoordeeld, geen effect op de beeldkwaliteit of het uitvoeren van betrouwbare dosimetrie van gezond leverweefsel, echter dosimetrie van levertumoren was verslechterd door de dode-tijd van de gammacamera.

Naast absolute activiteit zijn er andere parameters die ^{166}Ho SPECT beeldvorming beïnvloeden. ^{166}Ho heeft een complex spectrum, waarbij het voornaamste photopeak window wordt vervuild door scatter van hoog-energetische gamma's van ^{166}Ho. In een separate studie wordt ^{99m}Tc colloid intraveneus toegediend, na ^{166}Ho toediening, met de gedachte het gezonde leverweefsel beter te kunnen afbeelden. Dit vereist een zogenaamd 'dual-isotope' beeldvormingsprotocol, met de mogelijkheid om de ^{166}Ho en ^{99m}Tc signalen te kunnen scheiden en voor beide isotopen een individuele SPECT te kunnen reconstrueren. Als het dual-isotope protocol wordt gebruikt heeft scatter van de additionele isotoop, ^{99m}Tc (met de gamma-emissielijn op 140 keV) ook invloed op de beeldvorming van de ^{166}Ho photopeak (81 keV). Om te corrigeren voor scatter van ^{99}Tc en hoog-energetische gamma's van ^{166}Ho

zijn verschillende scatter-correctie factoren onderzocht in **Hoofdstuk 3**, door het gebruik van fantoommetingen en patiëntdata.

Om de ^{166}Ho SPECT beeldvorming verder te optimaliseren is een aanvullend protocol onderzocht middels fantoommetingen. **Hoofdstuk 4** beschrijft de acquisitieprotocollen en de invloed van verschillende reconstructieparameters op beeldkwaliteit. De voorgestelde protocollen worden nader onderzocht in een multi-center studie in verschillende Nederlandse ziekenhuizen, met als doel om ^{166}Ho SPECT beeldkwaliteit te harmoniseren.

Deel II – dosimetrie

Het ^{166}Ho-^{99m}Tc dual-isotope protocol kan dosimetrie verbeteren door te voorzien in een automatische delineatie van gezond leverweefsel. Echter, omdat de ^{166}Ho SPECT beelden in dit protocol geacquireerd zijn in aanwezigheid van een additioneel isotoop, ^{99m}Tc, moet bewezen worden dat deze reconstructies van voldoende kwaliteit zijn voor betrouwbare voor betrouwbare ^{166}Ho dosimetrie. **Hoofdstuk 5** vergelijkt de resultaten van de ^{166}Ho dosimetrie in aan- en afwezigheid van ^{99m}Tc, doormiddel van metingen in drie relevante volumes: longen, gezond leverweefsel en tumoren.

Het automatisch intekenen (segmenteren) van gezond leverweefsel met behulp van het dual-isotope protocol wordt beschreven in **Hoofdstuk 3**, binnen een fantoom studie. Deze methode is vervolgens toegepast op patiëntdata, zoals beschreven in **Hoofdstuk 6**. De automatisch verkregen segmentaties van gezond leverweefsel zijn vergeleken met handmatige segmentaties, ingetekend door een ervaren nucleair geneeskundige. Hierbij is gekeken naar de uiteindelijke dosimetrie en de overlap tussen de segmentaties. De relatie tussen toxiciteit van een behandeling en geabsorbeerde dosis in het gezonde leverweefsel is ook onderzocht. Naast toxiciteit van gezond leverweefsel kan ook radiatie pneumonitis een bijwerking zijn van radioembolisatie. Incidentie van radiatie pneumonitis en gebsorbeerde dosis in de longen, gebaseerd op PET/CT na ^{90}Y radioembolisatie, wordt gerapporteerd in **Hoofdstuk 7**.

10

List of Publications

Journal Articles

- **M. Stella**, A. J. A. T. Braat, M. G. E. H. Lam, H. W. A. M. de Jong, and R. van Rooij, "Evaluation of acquisition and reconstruction parameters to optimize holmium-166 SPECT imaging". *In preparation*

- **M. Stella**, R. van Rooij, M. G. E. H. Lam, H. W. A. M. de Jong, and A. J. A. T. Braat, "Automatic healthy liver segmentation for holmium-166 radioembolization dosimetry". *Submitted*

- B. Kunnen, R. van Rooij, **M. Stella**, M. G. E. H. Lam, H. W. A. M. de Jong, A. J. A. T. Braat. "Comparison of three different therapeutic particles in radioembolization of locally advanced intrahepatic cholangiocarcinoma". *Submitted*

- **M. Stella**, A. J. A. T. Braat, M. G. E. H. Lam, H. W. A. M. de Jong, and R. van Rooij, "^{166}Holmium–^{99m}Technetium dual-isotope imaging: scatter compensation and automatic healthy liver segmentation for ^{166}Holmium radioembolization dosimetry", EJNMMI Phys 9, 30 (2022)

- **M. Stella**, R. van Rooij, M. G. E. H. Lam, H. W. A. M. de Jong, and A. J. A. T. Braat, "Lung Dose Measured on Postradioembolization ^{90}Y PET/CT and Incidence of Radiation Pneumonitis", Journal of Nuclear Medicine July 2022, 63 (7) 1075-1080.

- **M. Stella**, A. J. A. T. Braat, R. van Rooij, H. W. A. M. de Jong, and M. G. E. H. Lam, "Holmium-166 Radioembolization: Current Status and Future Prospective", Cardiovasc. Intervent. Radiol. 45, 1634–1645 (2022)

- **M. Stella**, A. J. A. T. Braat, and M. G. E. H. Lam, "Holmium-166 Radioembolization in NET Patients", In: Limouris, G.S. (eds) Liver Intra-arterial PRRT with 111In-Octreotide, pp. 241–250, 2021

- **M. Stella**, A. J. A. T. Braat, M. G. E. H. Lam, H. W. A. M. de Jong, and R. van Rooij, "Gamma camera characterization at high holmium-166 activity in liver radioembolization", EJNMMI Phys 8, 22 (2021)

- M. M. A. Dietze, B. Kunnen, **M. Stella**, H. W. A. M. de Jong, "Monte Carlo-based scatter correction for the SMARTZOOM collimator", EJNMMI Phys. 2020 Jul 22;7(1):49

- **M. Stella**, A. J. A. T. Braat, M. G. E. H. Lam, H. W. A. M. de Jong, and R. van Rooij, "Quantitative ^{166}Ho-microspheres SPECT derived from a dual-isotope acquisition with ^{99m}Tc-colloid is clinically feasible", EJNMMI Phys 7, 48 (2020)

Conference Abstracts

- M. Stella, R. van Rooij, **M. G. E. H. Lam**, H. W. A. M. de Jong, and A. J. A. T. Braat, "Dose-toxicity analysis for NET patients treated with [166]Ho-radioembolization following PRRT". EANM 2022, Barcelona

- **M. Stella**, R. van Rooij, M. G. E. H. Lam, H. W. A. M. de Jong, and A. J. A. T. Braat, "Automatic healthy liver segmentation for [166]Holmium radioembolization". SNMMI 2022, Vancouver

- **M. Stella**, A. J. A. T. Braat, M. G. E. H. Lam, H. W. A. M. de Jong, and R. van Rooij, "The impact of different ^{99m}Tc activities on dual Isotope imaging for [166]Holmium scout radioembolization procedure". EANM 2021, Virtual

- **M. Stella**, R. van Rooij, M. G. E. H. Lam, H. W. A. M. de Jong, and A. J. A. T. Braat, "Lung dose assessment on PET/CT scans acquired after yttrium-90 liver radioembolization and occurrence of radiation pneumonitis". EANM 2021, Virtual

- **M. Stella**, A. J. A. T. Braat, M. G. E. H. Lam, H. W. A. M. de Jong, and R. van Rooij, "Clinical feasibility of quantitative holmium-166 SPECT in presence of technetium-99m colloid". SNMMI 2020, Virtual

- **M. Stella**, A. J. A. T. Braat, M. G. E. H. Lam, H. W. A. M. de Jong, and R. van Rooij, "Characterization of gamma camera performance at high holmium-166activity for imaging protocol optimization". SNMMI 2020, Virtual

- **M. Stella**, A. J. A. T. Braat, M. G. E. H. Lam, H. W. A. M. de Jong, and R. van Rooij, "[166]Ho only versus [166]Ho DI: a qualitative and quantitative comparison". EANM 2019, Barcelona

10

Acknowledgments

The PhD is a journey on its own, but not on your own.

Prof. Lam, I own you my life-standing gratitude for having introduce me to the Nuclear Medicine world with this PhD's opportunity. This topic has now become my passion, probably thanks to your never-ending enthusiasm. Your support enabled me to freely pursue my research interests within clinically relevant investigations.

Prof. de Jong, thanks for having challenged me with unexpected questions rather than comforting answers. This pushed me to improve my understanding and ultimately become a better, more curious, researcher. I am deeply grateful that my scientific output could benefit your feedback and knowledge.

Arthur and **Rob**, it has been a SPECTacular journey; and this is mostly your merit. Our weekly meeting has always been my safe harbor, your advices and guidance allowed me to navigate even during the stormiest moments. I guess that now I am ready to lift the sail and continue on my own, confident that, whenever lost, you will always be my lighthouses.

Gerrit, thank you for having always been present, even since before I started the PhD. I will always be grateful to you for the trust you gave me all along this journey with your discreet, but steady, presence.

To the **UMCU colleagues**, especially my office and hallway mates, who turned a working place into an occasion to exchange ideas and feedback, thanks for having contributed to my development. This dissertation is pervaded by your daily input.

To the **Quirem colleagues** who have always welcomed me in Deventer, making me feel part of a bigger project, thanks for your kind attitude and for showing your interest in my work.

Thanks to all the people who accompanied my PhD journey in Utrecht: you were there in that ephemeral transition between youth and adulthood, the summer solstice of life. We simply enjoyed it together before it was too late. I will always keep it as one of the lightest and joyful chapter of my life.

A special thanks goes to my friends who supported me during, but especially beyond, the PhD. How much grateful I am toward you cannot be constrained to this acknowledgment, nor can be expressed by words. Your value lays in my heart, in my everyday life, and in the certainty that I can simply count on you. I hope we keep piling memories, adventures and laughs together.

Grazie di essere la mia bussola, tu, che sai dare significato al silenzio, che ammiri la mia forza, ma che tolleri le mie debolezze. Tu, che rimani quando il fuoco si è spento, ma le braci ancora ardono.

Mamma, **papà** e **zia**, a voi che avete riposto la vostra fiducia nella mia felicità: grazie per esserci, ancora una volta. Mentre tutto muta, voi siete la mia certezza: il mio rifugio di partenza e di ritorno per ogni viaggio della vita.

10

Curriculum Vitae

Martina Stella was born on 30th March in Magenta, Italy. Following her humanistic studies at "Liceo Classico S. Quasimodo", she obtained her Bachelor's degree in Biomedical Engineering from the Politecnico di Milano (Italy).

She continued her Master studies in Biomedical Engineering at Politenico di Milano, following the *technologies for electronics* track. During her Master she enrolled in an exchange program at Ghent Universiteit (Belgium). There she focused on medical imaging. She concluded her Master studies at PIE Medical Imaging (The Netherlands), where she performed her Master's thesis on automatic heart valves tracking using 4D flow MRI.

After a period as research scientist at Quirem Medical B.V. (The Netherlands), she started her PhD at University Medical Center Utrecht (The Netherlands). Her PhD was part of the Industrial Doctorates programme, under a collaborative grant of the Dutch Research Council (NWO) between UMC Utrecht and Quirem Medical B.V. During her PhD, she served as PhD representative for the Medical Imaging programme at the PhD council as well as at the Medical Imaging committee.

The findings of her PhD are described in this dissertation.